

UNIVERSITY of CALIFORNIA

Santa Barbara

Auger-Generated Hot Carrier Photocurrent in Forward Biased InGaN LEDs

A Dissertation submitted in partial satisfaction of the

requirements for the degree

Doctor of Philosophy

in

Materials

by

Andrew Colin Espenlaub

Committee in charge:

Professor James S. Speck, Co-Chair

Professor Shuji Nakamura, Co-Chair

Professor Claude Weisbuch

Professor Jacques Peretti, École Polytechnique

September 2018

The dissertation of Andrew Colin Espenlaub is approved.

Jacques Peretti

Claude Weisbuch

Shuji Nakamura, Co-Chair

James S. Speck, Co-Chair

August 2018

Auger-Generated Hot Carrier Photocurrent in Forward Biased InGaN LEDs

Copyright © 2018

by

Andrew Colin Espenlaub

Curriculum Vitae

Andrew Colin Espenlaub

EDUCATION

PhD in Materials Science and Engineering (2012-present) – (GPA 3.84/4.0)

University of California Santa Barbara, Santa Barbara CA

BS in Physics (honors program), *magna cum laude* (2008-2012) – (GPA 3.73/4.0)

University of Pittsburgh, Pittsburgh PA

TEACHING

Teaching Assistant (Spring Quarter 2017)

MATRL 206B, Materials Department UCSB

Grader (Winter Quarter 2017)

MATRL 206A, Materials Department UCSB

Teaching Assistant (Spring Quarter 2015)

MATRL 288V, Materials Department UCSB

Teaching Assistant (Winter Quarter 2015)

MATRL 101, Materials Department UCSB

RESEARCH EXPERIENCE

Graduate Research Assistant, Speck and Nakamura Groups (2012-present)

University of California Santa Barbara, Santa Barbara CA

Undergraduate Research Assistant, Choyke Group (2008-2012)

University of Pittsburgh, Pittsburgh PA

PUBLICATIONS

Auger-generated hot carrier current in photo-excited forward biased single quantum well blue light emitting diodes

Espenlaub, A.C., A.I. Alhassan, S. Nakamura, C. Weisbuch, J.S. Speck, *Applied Physics Letters*, 112, 141106 (2018).

High wall-plug efficiency blue III-nitride LEDs designed for low current density operation

Kuritzky, L.Y., A.C. Espenlaub, B.P. Yonkee, C.D. Pynn, S.P. DenBaars, S. Nakamura, C. Weisbuch, J.S. Speck, *Optics Express*, 25, 30696 (2017).

Stability of materials in supercritical ammonia solutions

Pimputkar, S., T.F. Malkowski, S. Griffiths, A. Espenlaub, S. Suihkonen, J.S. Speck, S. Nakamura, *Journal of Supercritical Fluids*, 110, 193 (2016).

Using Intrinsic Defect Spectra in 4H SiC as Imbedded Thermometers in the Temperature Range from 100 degrees C to 1500 degrees C

Yan, F., A. Espenlaub, R.P. Devaty, T. Ohshima, W.J. Choyke, *Materials Science Forum*, 679-680, 237 (2011).

HONORS AND AWARDS

Peter F. M Koehler Junior/Senior Academic Achievement Award (2012)

Department of Physics and Astronomy, University of Pittsburgh

Halliday Award for Excellence in Undergraduate Research (2012)

Department of Physics and Astronomy, University of Pittsburgh

Julia Thompson Award for Excellence in Undergraduate Writing (2011)

Department of Physics and Astronomy, University of Pittsburgh

Acknowledgements

I would like to acknowledge the many people without whom I would not have been able to complete this dissertation, and who generally put up with me for six years while I did.

First, of course, are the past and present members of my committee. In particular, I am grateful to Jim Speck for providing me a research project when I was suddenly sorely lacking in one, among many things. To Claude Weisbuch I am indebted for the many hours spent in his office discussing the physics and history of semiconductors – I think some of it might have sunk in. I have to thank Shuji Nakamura for what will almost certainly remain the easiest job interview I'll ever be lucky enough to get, when I first visited UCSB, and for second chances. I am also grateful to Jacques Peretti, who agreed to join my committee well into my time here despite spending most of his time in another country, and to Steven DenBaars and Michael Doherty for remaining on my committee as long as they did after my research drifted from their own areas of interest.

That research would not have been possible without the epi growers at UCSB, namely Abdullah Alhassan and Erin Young. They were always very accommodating of my special, and unusual requests. Additionally, the many technical staff who maintain the fabulous facilities here at UCSB – too many to name – have been crucially important.

I am indebted to all the members of the Nakamura, DenBaars, Speck, and Gordon groups, my fellow graduate students and friends, from whom I have learned so much about cleanroom processing, device physics, epi growth over the years. More importantly, we shared innumerable fun and memorable times which I shall never forget.

My early time in graduate school were spent disproportionately in the Physics machine shop and, rather paradoxically, those many hours machining odds and ends for custom lab

equipment taught me some of the most useful skills, for work and life in general, that I have learned since coming to UCSB. This is thanks to everyone in the shop, but especially to the enormous patience of Guy Patterson, Master Machinist and dispenser of the secrets of “how the big boys do it.” Because of Guy, I can honestly claim, for the first time in my life, to be ‘handy,’ around the lab and otherwise. But what do I know?

Lastly, I could not have made it this far without the unwavering support of my family.

*To Peggy Ann Espenlaub,
Grandmother*

Abstract

Auger-Generated Hot Carrier Photocurrent in Forward Biased InGaN LEDs

By

Andrew Colin Espenlaub

This dissertation presents measurements of the photocurrent in forward biased III-Nitride light emitting diodes (LEDs). This photocurrent is observed to be in the forward direction, and is therefore attributed to the hot carriers being generated by Auger recombination in the active region of the device. There is strong evidence that Auger recombination is the cause of the well-known phenomenon of efficiency droop in III-Nitride LEDs, which significantly limits the efficiency of high brightness LED lighting. Therefore, the photocurrent measurements presented in this dissertation are a step towards a benchtop technique to more easily study the physical origins of efficiency droop in commercial LEDs.

First, single quantum well (SQW) devices are studied, as these are the simplest platform to interpret the results of the measurements. Next, devices with multiple quantum wells (MQW) are studied, as all commercial LEDs are MQW devices. Additionally, measurements of LEDs grown by ammonia molecular beam epitaxy (NH_3 MBE) are presented. These LEDs show no droop, even out to high drive current densities. Finally, measurements of the photocurrent in LEDs processed from commercial epi are presented.

Table of Contents

1	Introduction.....	1
1.1	Group III-Nitrides and Light Emitting Diodes	1
1.2	Motivation	2
1.3	Overview of Subsequent Chapters	3
2	Background	5
2.1	The pn-Junction	5
2.2	GaN, InN, AlN, and Their Alloys	10
2.3	The Quantum Well Light Emitting Diode.....	14
2.4	III-Nitride Quantum Wells	16
2.5	Efficiency in Light-Emitting Diodes	18
2.6	Models of Efficiency Droop in III-Nitride LEDs.....	26
2.7	Photo-Induced Currents in Semiconductor Devices.....	32
3	Methods and Apparatus.....	41
3.1	Overview of the Measurement Problem.....	41
3.2	Device Structure	44
3.3	Optical and Electrical Apparatus	48
4	Photocurrent in SQW Blue LEDs	54
4.1	Introduction	54
4.2	Epi Design	57
4.3	Results	59
4.4	Discussion.....	68

5	Photocurrent in MQW Blue LEDs.....	78
5.1	Introduction	78
5.2	Epi Design	78
5.3	Results	80
5.4	Discussion.....	90
6	Ongoing and Future Work.....	98
6.1	Introduction	98
6.2	Commercial Epi and Devices	98
6.3	Green LEDs	99
6.4	ABC Modeling and Photocurrent	100
6.5	Defect-Assisted Auger.....	103
	References.....	108
A.	Photolithography Process Follower.....	113
A.1	Main Process.....	113
A.2	Photolithography Processes	116
B.	Control Program Code.....	117
B.1	Python 3 Code	117
C.	Auger-Generated Hot Carrier Currents	137
C.1	Conventional Auger Recombination.....	140
C.2	Defect-Assisted Auger Recombination.....	142

1 Introduction

1.1 Group III-Nitrides and Light Emitting Diodes

The human history of lighting is very long, but it is only relatively recently that it involved anything other than something on fire, e.g. – wood fires, oil lamps, wax candles, and kerosene and natural gas lamps. In a flame, the vapors emits light, including visible light, due to the high temperature of the particulates in the flame and the partial ionization of the gases. Arguably, even the light from carbon-arc lamps and gas-discharge lamps, which use electric current to ionize and superheat a gas, have more in common with candlelight than with more modern solid-state lighting.¹ It wasn't until the incandescent lightbulb was invented that humanity finally had a practical lighting solution which didn't involve a glowing, ionized gas.

The incandescent lightbulb still relies on getting something (the filament) really hot to generate light however. Using a hot object — a solid or a gas — to generate visible light is extremely inefficient as most of the thermal energy is radiated at infrared wavelengths. Even the sun (a large ball of glowing, ionized gas) radiates over half of its light in the infrared [2].

The first lighting technology which did not involve an ionized gas or a deliberately hot object was the light emitting diode (LED), first invented in 1928 by Oleg Vladimirovich Lossev [3]. LED technology utilizes the electroluminescence from a semiconductor diode to provide light, and Lossev's LED was a particular type of diode called a point-contact diode. It was made using a material then known as "carborundum", what is now called silicon carbide. Lossev's work has only recently been rediscovered [4], so he is still not always properly credited for the invention of the LED.

¹ For more on the history of lighting, the reader is referred to reference [1], and to the references therein.

LEDs can be very efficient at converting electrical energy into visible light (though Lossev's certainly wasn't as it was made from an indirect bandgap material like silicon carbide). With the invention of the first practical, high brightness blue LEDs by Shuji Nakamura in the early 1990s [5], [6], the solid-state lighting revolution could truly begin. Other bright LEDs existed before then, at longer wavelengths [1], but it wasn't until high brightness blue LEDs were available that white LED lighting was possible. Modern LED bulbs use blue LEDs to excite yellow (or a mixture of yellow and red) phosphors so that the combination of the emission from the LED and the phosphor appears white to human eyes. Without blue LEDs, white LED lighting wouldn't be possible. LED lighting is even more energy efficient than fluorescent lighting and is rapidly replacing more traditional lighting solutions worldwide [1].

Blue LEDs today are made from a class of direct bandgap semiconductors known as the group III-nitrides — gallium nitride (GaN), indium nitride (InN), aluminum nitride (AlN), and their alloys. The unique material properties and the challenges they represent for LED design will be discussed in more depth in the next chapter.

1.2 Motivation

III-nitride LEDs are very energy efficient, but there are still limitations. One of these is the phenomenon known as efficiency droop wherein an LED becomes less efficient when it is driven above a certain current density. Every blue LED exhibits some degree of efficiency droop, eventually, and it is a significant factor affect the design of high power, high efficiency LED lighting. The work presented in this dissertation is aimed squarely at the problem of efficiency droop, and of understanding its physical origins.

There are multiple proposed explanations for efficiency droop in III-nitride LEDs, which will be discussed in detail in the next chapter, and the issue is hotly debated in the scientific community. Recent work by UCSB researchers [7] on ultra-high vacuum electroemission spectroscopy on operating LEDs has provided convincing evidence that a phenomenon known as Auger recombination is intimately connected to efficiency droop, and perhaps is even its dominant cause. Auger recombination is a process that generates high energy electrons and holes within the semiconductor, and these "hot" carriers can produce current within the device. Due to their large kinetic energy, Auger-generated hot carriers can easily surmount barriers within the device which other carriers cannot, allowing them to potentially be distinguished. This dissertation presents measurements of photo-induced forward current in resonantly excited blue LEDs, forward biased into the droop regime. An argument will be made that the photo-induced current can only be due to Auger-generated hot carriers and thus is a signature of Auger recombination within the active region of the device. Hopefully this will provide a fruitful avenue for studying the causes of efficiency droop in III-nitride LEDs for other researchers in the future.

1.3 Overview of Subsequent Chapters

The rest of this dissertation is organized as follows. Chapter 2 will cover the basic operating principles of III-nitride LEDs and review the literature on the causes of efficiency droop in LEDs, as well as prior observations of forward biased photocurrent in pn-junction devices. Chapter 3 will present the measurement apparatus used in this work to measure the forward biased photocurrent. In Chapters 4 and 5, the results of measurements on single quantum well (SQW) and multiple quantum well (MQW) blue III-nitride LEDs will be

presented. Chapter 6 will present ongoing and proposed future work to further understand the photocurrent measurements and efficiency droop in general.

The nanofabrication process used to manufacture the LEDs used in this work, and the computer code used to control the measurement apparatus can be found in the appendices, as well as a detailed discussion of the different types of Auger processes which may occur in III-nitride LEDs.

2 Background

This chapter will introduce the basic architecture of III-nitride light emitting diodes (LEDs), some of the relevant material properties of the III-nitrides, and the formalism for talking about LED efficiency and efficiency droop. Then, the published models of efficiency droop which appear in the literature will be briefly reviewed, to place the work in this dissertation in some context. Finally, several types of photo-induced currents which may occur in semiconductor devices will be discussed, and the few published results on photocurrent in forward-biased pn-junction devices will be discussed.

2.1 The pn-Junction

Nearly every commercial LED today is built from a junction of p-type and n-type semiconductors called a pn-junction. As will be seen in later sections, a good understanding of pn-junction operation is important for assessing the published theories of efficiency droop. Therefore, it will be useful to briefly present the DC electrical characteristics of these junctions before moving on to discuss LED operation in more detail.

A band diagram of a symmetric pn-junction at zero bias is shown in Figure 2.1.1. The region around the junction is depleted of free carriers, and the resulting space charge from the ionized dopants generates a built-in field in the junction. In equilibrium, diffusion of electrons from the n-side to the p-side, and of holes in the opposite direction, is balanced by drift of electrons and holes in the built-in field and no net current flows. If the n-side is kept at a positive potential relative to the p-side, the field in the junction increases and a small net drift current flows, in what is defined as the reverse direction. If instead the p-side is kept at a

positive potential relative to the n-side, then the applied field cancels out some of the built-in field and reduces the barrier to diffusion so that a net current flows in the forward direction.

This is shown in Figure 2.1.2.

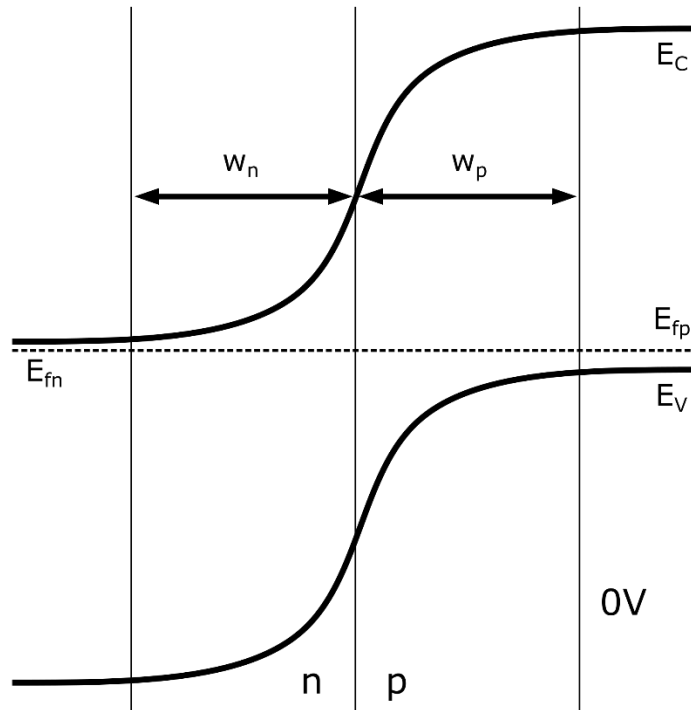


Figure 2.1.1: A diagram of the conduction (E_C) and valence (E_V) bands for a symmetric pn-junction at zero bias. The quasi-Fermi levels (E_{fn} and E_{fp}) for the electrons and holes are identical and the system is in equilibrium. The widths of the depletion regions are labelled as w_n and w_p , and are equal due to the symmetry of the doping in the junction.

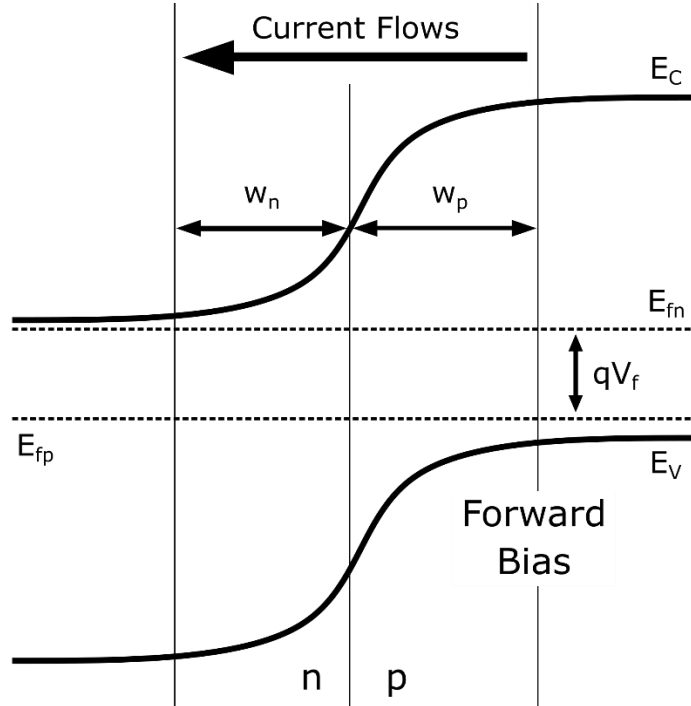


Figure 2.1.2: A diagram of the conduction (E_C) and valence (E_V) bands for a symmetric pn-junction under forward bias. The quasi-Fermi levels (E_{fn} and E_{fp}) for the electrons and holes are no longer equal, and their separation is equal to the forward applied voltage, V_f . The widths of the depletion regions are labelled as w_n and w_p , are equal due to the symmetry of the doping in the junction, and are smaller than at zero bias. The built-in field across the junction is reduced by the applied field, and a net current flows in the forward direction – from right to left in this diagram (electrons flow from left to right).

If both sides of the junction are significantly thicker than the respective minority carrier diffusion lengths, then the diode is considered a "long diode". In the absence of recombination in the depletion region of the junction, the current density in the device is given by the classic Shockley equation [8].

$$J = J_s(e^{qV/kT} - 1) \quad (2.1.1)$$

where

$$J_s = \frac{qn_p D_n}{L_n} + \frac{qp_n D_p}{L_p} \quad (2.1.2)$$

with q as the fundamental electron charge, D_n and D_p as the minority carrier diffusivities for electrons and holes respectively, and with n_p and p_n as the minority carrier concentrations at the p-side and n-side edges of the junction respectively. This equation is derived using the full depletion approximation, and assumes that the total thickness of the material on both sides of the junction is much greater than the minority carrier diffusion lengths on those sides (the electron diffusion length on the p-side, and the hole diffusion length on the n-side). The gradients in the minority carrier concentrations at the edge of the junction are approximated by assuming that the concentrations decrease linearly and vanish at precisely one diffusion length [8].

When the diode is forward biased, the exponential is much larger than the second term and the current is almost entirely minority carrier diffusion current away from the junction. In this limit the electron minority carrier diffusion current density, on the p-side, is given by

$$J_n = \frac{qn_p D_n}{L_n} e^{qV/kT} \quad (2.1.3)$$

while the hole minority carrier diffusion current density, on the n-side, is given by

$$J_p = \frac{qp_n D_p}{L_p} e^{qV/kT} \quad (2.1.4)$$

If one or both sides of the junction are similar or small in thickness compared to the relevant minority carrier diffusion length, then the diode is considered a "short diode". If the contact to the short side of the junction is Ohmic, the minority carrier density still vanishes, but it does so over the distance from the edge of the depletion region to the contact. Therefore, the diffusion lengths in the Shockley equation get replaced by the width of the quasi-neutral region on the short side of the junction.

This is approximately the width of the short side, unless the depletion region width on that side extends an appreciable distance towards the contact, in which case the effective width will change with bias. In the case the former case, assuming the p-side is short, the electron minority carrier diffusion current density becomes

$$J_n = \frac{qn_p D_n}{W_p} e^{qV/kT} \quad (2.1.5)$$

where W_p is the total width of the material on the short p-side of the junction. For $W_p < L_n$, the current in the short diode is larger than that in a long diode by a factor of $L_n/W_p > 1$.

Short diodes appear to "turn on" at lower voltages than long diodes, because the current is larger for the same bias – that is, the short diode will reach a given current density, say 1 A/cm², at a lower voltage than a long diode. Most III-nitride LEDs are short on the p-side since the p-type layer is typically only a few hundred nanometers thick and the minority carrier diffusion length in p-GaN is, depending on doping and dislocation density, anywhere from ~50-100 nm up to 1 μm in the more extreme cases [9]–[12]. This has implications when discussing the so-called "injection efficiency" under forward bias.

If there is recombination inside the depletion region of a pn-junction, then the Shockley equation changes form to include something called the ideality factor of the diode. In symmetric junctions, this factor varies from 2 to 1 depending on how much Shockley-Read-Hall (SRH) recombination there is in the junction. In asymmetric junctions, the simple mono-exponential form of the Shockley equation ceases to adequately describe the behavior of the junction. If measured current-voltage (IV) characteristics are force-fit to the Shockley equation, ideality factors well outside this theoretical range are extracted. This is also the case for some III-Nitride LEDs, where ideality factors can even be as high as 7 [13], though they

can also be less than 2. It varies with device design and active region quality and should only be used with caution when analyzing the electrical behavior of LEDs.

2.2 GaN, InN, AlN, and Their Alloys

The vast majority (if not totality) of commercial, short wavelength visible (violet, blue, green) LEDs are based on gallium nitride (GaN) pn-junctions. This includes all LED lighting, which is generated white light using a blue LED to pump one or more phosphors.

With a bandgap of 3.39 eV at room temperature [14], GaN is considered a wide bandgap semiconductor. The group III-nitrides indium nitride (InN) and aluminum nitride (AlN), along with GaN, form a material system – the AlInGaN system. AlInGaN alloys can, in principle, have direct bandgaps ranging from ~0.7 eV to 6.2 eV [15]–[17]. This range spans from the near-infrared (~1.78 μm) to the mid-UV (200 nm). The binary compounds that make up the endpoints of the AlInGaN system (AlN, GaN, and InN) have a number of advantages which make it technologically useful. Among them are that:

- they all share the same crystal structure;
- they are all direct bandgap semiconductors;
- they have Type I band alignments with each other.

Sharing the same, wurtzite, crystal structure (shown in Figure 2.2.1) allows single crystal films with a wide range of alloy compositions to be grown. The direct bandgaps allow for efficient light emission at room temperature, which is important for making light emitting devices.

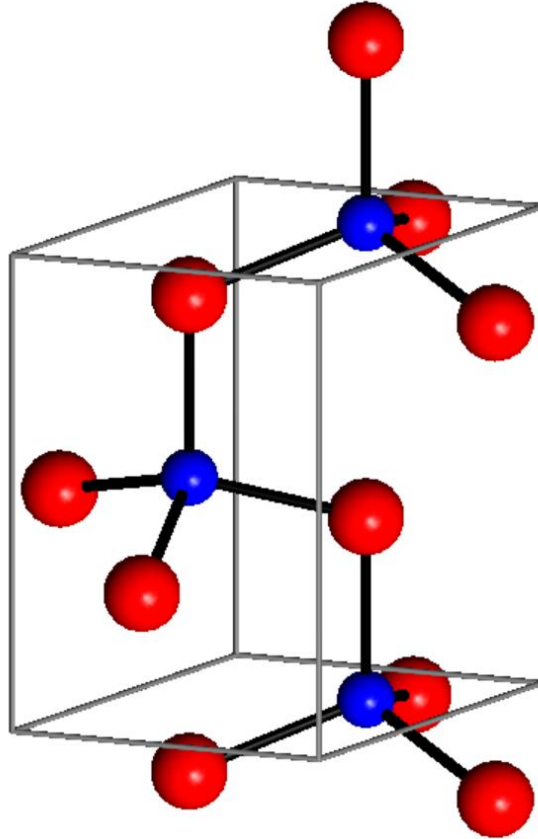


Figure 2.2.1: The unit cell of the wurtzite unit cell is shown, with the [0001] axis oriented up. The anions are shown in red and the cations in blue.

Because the materials in the AlInGaN system have Type I band alignments (see Figure 2.2.2), a specific type of heterostructure called a quantum well (QW) can be grown using two different alloys of different bandgaps. These heterostructures are discussed in the next section, and are central to efficient LED technology.

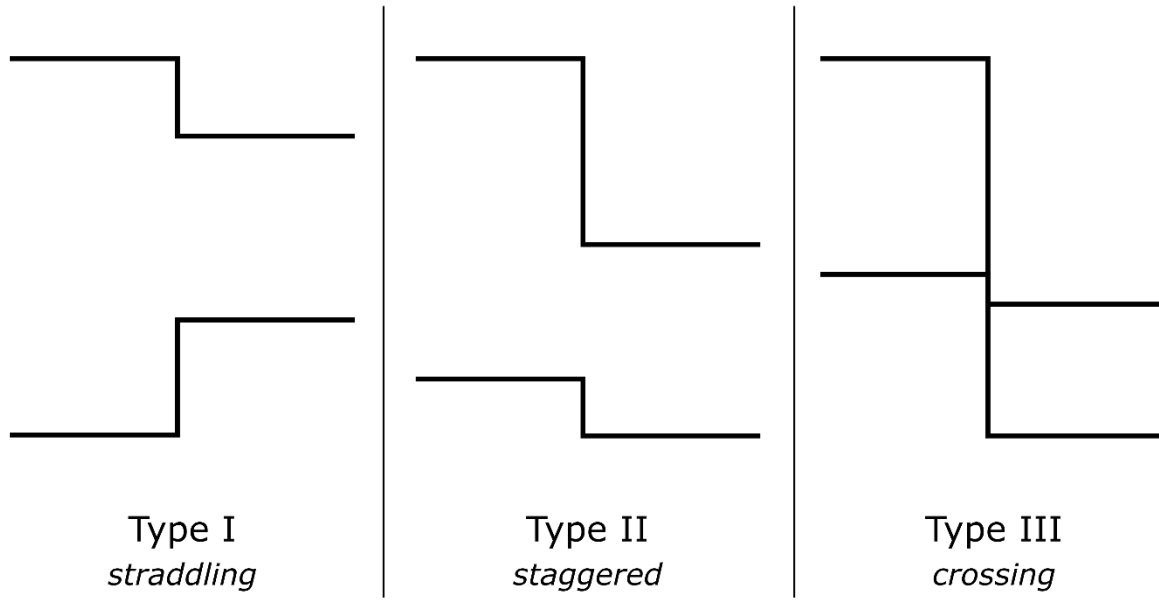


Figure 2.2.2: The three possible types of band alignments for semiconductor heterostructures are shown. In each case, the conduction band minimum and valence band maximum are shown. The type I alignment is known as *straddling* alignment, while the type II alignment is known as *staggered*, and the type III alignment is known as *crossing*.

The AlInGaN system also has some disadvantages. Some of the more important for LEDs are:

- AlInGaN alloys have spontaneous polarization fields;
- AlInGaN alloys are strongly piezoelectric;
- there is a large lattice mismatch between the binary compounds;
- there is no cheap native substrate.

The wurtzite crystal structure has space group $P6_3mc$ and point group $6mm$. This axial point group is non-centrosymmetric and thus polar. The spontaneous polarization \mathbf{P}_s is along the $[000\bar{1}]$ direction. Additionally, they are all strongly piezoelectric. This, coupled with the large lattice mismatch between InN and GaN (and to a lesser extent, the mismatch between AlN and GaN), means that there is usually a large polarization charge at the interfaces between

different alloys in the AlInGaN system. The lattice mismatch also limits the practical thickness of high quality strained epitaxial layers.

The absence of inexpensive native GaN substrates means the epitaxial material for GaN-based devices is usually grown on foreign substrates, which unfortunately have a large lattice mismatch with GaN. The most common substrate for LEDs is sapphire, due to its transparency in the visible wavelengths. Another common substrate, especially for electronic devices, is silicon due to its low cost.

Both n-type and p-type doping of AlInGaN alloys are possible. Doping to make GaN and smaller bandgap alloys n-type is very efficient. The most common intentional n-type dopant is silicon, though other efficient donors exist (such as oxygen and germanium). Magnesium is the only practical acceptor, though it has a large ionization energy, [18], leading to only ~1% ionization at room temperature in GaN. In addition, the acceptors must be activated by thermally annealing the p-type material at high temperatures to drive out hydrogen, which passivates the Mg atoms [19].

The large ionization energy of Mg in GaN leads to asymmetrically doped pn-junctions in LEDs, where high conductivity n- and p-type regions are desirable. There can be an order of magnitude as much Mg on the p-side as there is Si on the n-side of the junction. Even so, the n-side typically still has a higher majority carrier concentration due to the low ionization efficiency of Mg. Counterintuitively, the higher overall dopant atom concentration on the p-side leads to most of the built-in voltage of the junction to be dropped across the n-side depletion region, despite there being more free carriers on the n-side. As far as the depletion region is concerned, GaN LEDs behave like p⁺/i/n junctions, not p-/i/n junctions.

2.3 The Quantum Well Light Emitting Diode

As mentioned in the previous section, the binary group-III nitrides have Type I band alignments with each other. This type of alignment means that when a thin layer of a smaller bandgap material is sandwiched between two layers of a larger bandgap material a potential well forms in both the conduction band and the valence band, shown below, in Figure 2.3.1.

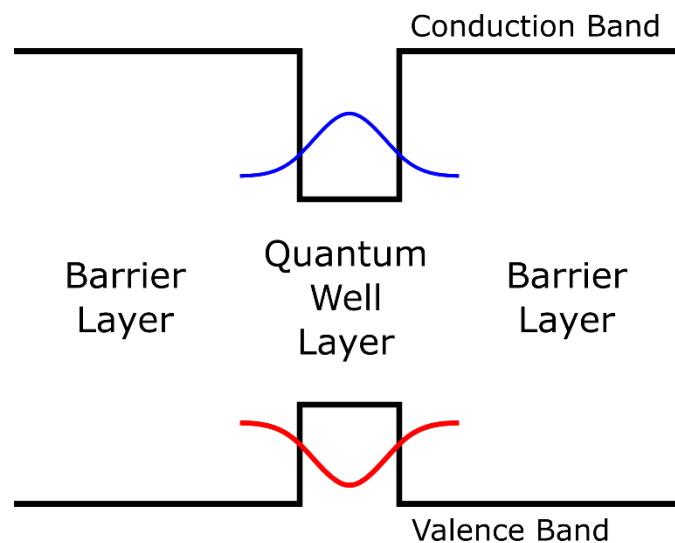


Figure 2.3.1: A schematic quantum well with type I band alignments between the quantum well material and the barrier material. Both the electron (blue) and hole (red) wavefunctions will be confined in the potential well, which would not occur if the material had type II or type III band alignments.

A potential well will tend to concentrate free carriers from the surrounding material, and a potential well formed between materials with Type I band alignments will concentrate both electrons and holes. This leads to an increase in the recombination rate of electrons and holes relative to the recombination rate in the bulk. Furthermore, the higher concentrations of electrons and holes affect the relative magnitude of the various recombination mechanisms, such as radiative recombination. This was first suggested by H. Kroemer [20] as a way to

increase the efficiency of semiconductor lasers. Potential wells have also proven useful for making high efficiency LEDs.

If the smaller bandgap layer is thin enough, the potential well is called a quantum well (QW), since the solutions to the Schrödinger equation in the well begin to behave like the solutions to the classic elementary quantum mechanics problem of the same name.

When a QW is placed in the depletion region of a pn-junction, it will accumulate electrons from the n-type material and holes from the p-type material. Under forward bias, more carriers will be injected from the contacts into the QW layer (as majority carrier diffusion current), where a large fraction will get trapped in the well and recombine. In a well-designed LED, this recombination will be mostly radiative, and will utilize a large fraction of the total current injected from the contacts. The exact proportions depend on the magnitude of the junction's minority carrier diffusion current, the relative carrier density dependence of the radiative and non-radiative rates in the QW, and the depth and thickness of the QW.

In the infrared, the AlInGaAs system can be used to make QW LEDs, and in the near-infrared and long wavelength visible (red/orange/yellow), the AlInGaP system is commonly used. The AlInGaN system, however, dominates the market for short wavelength visible (green/blue/violet) and near-ultraviolet LEDs, as the efficiency of AlInGaP LEDs decreases as the emission wavelength is pushed shorter, into the yellow and green. Similarly, AlInGaN LEDs become increasingly inefficient at longer wavelengths. There is a wavelength range, from the green into the yellow, where no material system is very efficient, which is called the "Green Gap". Closing this gap is a focus of considerable research efforts in the LED community, and the work in presented in this dissertation may contribute to understanding the origins of this gap, as will be discussed in later chapters.

2.4 III-Nitride Quantum Wells

Because the III-nitrides are polar and strongly piezoelectric, and because epitaxial layers such as QWs are typically highly strained, the shape of the potential well is different in the nitrides from other material systems. Shown in Figure 2.4.1 is a schematic showing the effect of polarization fields in a c-plane InGaN QW on the band structure of an LED.

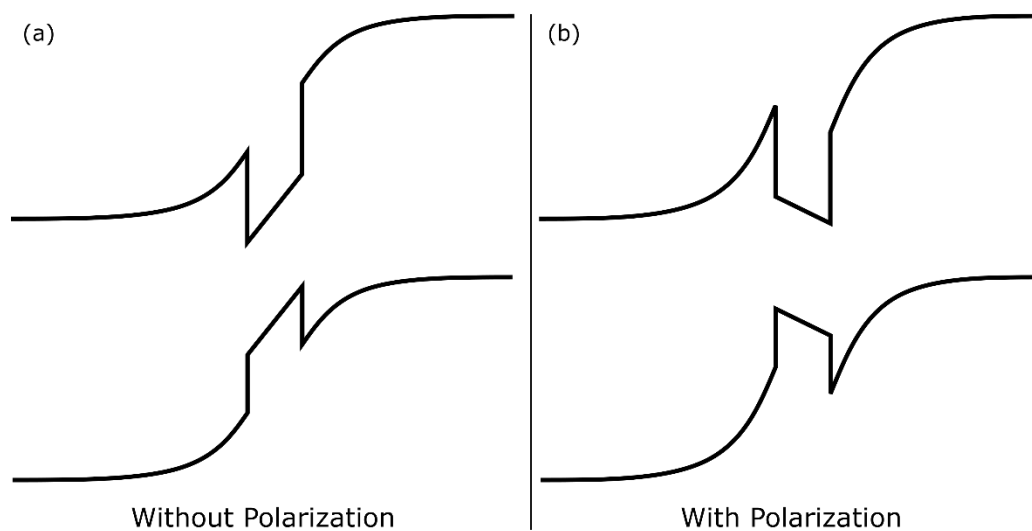


Figure 2.4.1: Band diagrams for forward biased quantum well LEDs (a) without, and (b) with polarization fields as in InGaN c-plane LEDs. As the forward bias increases, the magnitude of the net field in the QW layer decreases towards zero in the LED shown in (a), but increases in the LED shown in (b).

The addition of the polarization fields to the built-in field of the pn-junction creates a much more triangular well shape that separates the bound electrons and holes to opposite sides of the QW layer. This separation reduces the electron-hole wavefunction overlap and consequently decreases the radiative recombination rate in the QWs of c-plane nitride LEDs. The separation increases with QW thickness and practical LEDs often have very thin QW layers (~3 nm) as a result. The polarization fields can be screened by free carriers at high carrier densities, though full screening never occurs, even at very high current densities.

Another peculiarity of InGaN QWs is that random local fluctuations in the alloy composition result in regions of relatively high In content [21]. These composition fluctuations lead to fluctuations in the position of the conduction band minimum and valence band maximum in the QW layer. At low carrier densities, the high In regions are thought to be sufficiently deep to confine electrons and holes locally, simultaneously increasing their wavefunction overlap and helping reduce the negative impact of high threading dislocation density. Threading dislocations are non-radiative recombination centers, and typically occur at a high density in InGaN QWs because GaN-based LEDs are grown heteroepitaxially, on substrates with large lattice mismatch.

High efficiency, commercial nitride LEDs use a multiple QW (MQW) design to enhance light output power. It is still an open question why multiple QWs help the efficiency and output power of an LED, since there is evidence that only the QW nearest the p-side of the LED emits a significant amount of light in typical MQW LEDs [22]. Commercial LEDs all have MQWs though (apparently there is some small improvement), and this must be kept in mind when conducting LED research. It may be simpler to study SQW LEDs from an analytical point of view, but to have an impact on the state-of-the-art the conclusions drawn from experiments on SQW devices must be extended to MQW designs.

Commercial nitride LEDs also typically have what is called an electron-blocking layer (EBL) on the p-side of the MQW active region. This layer has a wider bandgap than the p-type GaN it is embedded in, through alloying with AlN, and is usually thought to help reduce the number of electrons injected from the n-side that overshoot the active region entirely, and thus never recombine radiatively in the QWs. However, it is unclear whether or not EBLs actually block overshoot of electrons effectively. Alloy fluctuations in the AlGaIn may allow

percolative transport of electrons through the barrier [23]. Despite this uncertainty over how they improve performance, they do, and so EBLs are typically included in commercial LEDs.

2.5 Efficiency in Light-Emitting Diodes

At the core of the motivation for the work presented in this dissertation is the so-called 'efficiency droop' problem in nitride QW LEDs, so it will be useful to quickly discuss LED efficiency — and what it means for it to droop. The following section provides a review of the various published models on the origin of efficiency droop in III-nitride LEDs. The work in this dissertation implicitly takes a particular view of the origins of efficiency droop, so this discussion is important to provide some context.

An ideal LED would produce one photon for every electron travelling between its terminals, and all of those photons would make it out of the device. This would represent 100% external quantum efficiency (EQE). The formal definition of EQE is the photon flux exiting the device divided by the electron flux flowing through the device.

$$EQE = \frac{(\textit{photon flux})}{(\textit{electron flux})} \quad (2.5.1)$$

The ideal LED would also produce nearly monochromatic photons (with energy $h\nu$) at biases at or below the voltage $h\nu/q$ so that the power conversion efficiency – sometimes called the wall plug efficiency (WPE) – is greater than or equal to 100%. Since the optical output power is $L = h\nu \cdot (\textit{photon flux})$, and the current through the LED is $I = q \cdot (\textit{electron flux})$, the relationship between EQE and WPE is

$$WPE = \frac{L}{IV} \quad (2.5.2)$$

$$\begin{aligned}
&= \frac{h\nu \cdot (\textit{photon flux})}{q \cdot (\textit{electron flux}) \cdot V} \\
&= \frac{h\nu/q}{V} \cdot EQE
\end{aligned}$$

Greater than 100% WPE is not a violation of the Laws of Thermodynamics as it simply means that the LED is cooling its surroundings and using some thermal energy in the conversion of electrical power into optical output power. In real LEDs there are several sources of loss which cause both the EQE and the WPE to be less than 100%.

First, LEDs must typically be operated at voltages above the photon voltage, $h\nu/q$, to produce a sufficient intensity of light. This reduces the WPE by a factor of $h\nu/qV$. No LED with greater than 100% WPE has been demonstrated to date at practical output powers (the record WPE is >80% at 20 mA [24]), though >100% WPE has been demonstrated at very low output powers in a cryogenically cooled infrared LED [25]. Very efficient III-Nitride LEDs have been shown to emit a reasonable amount of light slightly below the photon voltage so that $WPE > EQE$, but not yet at a $WPE > 100\%$ [26].

Second, not every photon that is produced within the device escapes the semiconductor chip or its packaging, instead getting absorbed at metal surfaces such as the contacts to the device, or in other parts of the device. The fraction of the generated photon flux which escapes the device is called the light extraction efficiency (LEE). The EQE divided by the LEE is referred to as the internal quantum efficiency (IQE) of the device.

$$IQE = \frac{EQE}{LEE} \tag{2.5.3}$$

Third, there may be leakage paths shunting the junction (though these are negligible in good LEDs), or carriers may overshoot the QWs and avoid recombination in the active region. Overshooting carriers simply participate in the usual minority carrier diffusion current of the

diode. The fraction of the current injected at the terminals of the device which ends up as recombination current in the QWs in the active region of the device is called the injection efficiency (IE). It is frequently assumed that the IE in LEDs is approximately 100%, though this may not be entirely accurate due to how short the p-side of most III-nitride LEDs is. Ideally the IE would be calculated by a computer simulation of the IV characteristics of the LED, but current simulation software for QW LEDs is insufficient to accurately model the IE in a predictive manner. This is largely due to the immense difficulty of correctly modelling carrier transport perpendicular to quantum structures, especially in strongly piezoelectric materials with large compositional alloy fluctuations.

Finally, not all of the recombination processes in the QWs of the LED are radiative. Indeed, the advantage of using QWs is that they reduce the importance of the non-radiative SRH process relative to radiative recombination, by concentrating electrons and holes in the same space. This works because the radiative rate is a 2nd order reaction (to borrow terminology from chemistry), while the SRH rate is only 1st order since the defect-mediated recombination takes places via two single carrier processes (electron capture and hole capture) which occur in series.

The fraction of the recombination current which is radiative will be referred to as the “radiative efficiency” in this dissertation, and may be defined for the device as a whole, or for each individual QW. The radiative efficiency, η_{rad} , of the whole device is the IQE divided by the IE, and is the average of the radiative efficiencies of the QWs, weighted by the fraction of the recombination current which occurs in each QW.

$$\eta_{rad} = \frac{IQE}{IE} = \frac{1}{N_{QW}} \sum_i^{all\ QWs} \frac{(radiative\ rate)_i}{(total\ rate)_i} \quad (2.5.4)$$

It is frequently assumed that all of the recombination current occurs in the QW closest to the p-side of the junction, since most of the light is emitted from this QW. This is likely because of the short mean free path of the holes injected from the p-side of the device, which results in most of the holes becoming trapped in the QW nearest the p-side. As III-nitride LEDs are always grown n-side first, this QW is always the last to be grown and so is also referred to as the "top QW" in this work, while the other QWs are called the "lower QWs".

There are three important recombination processes which are thought to occur in nitride QWs: SRH, radiative, and Auger recombination. Each has a different dependence on the carrier densities in the QW. The SRH rate for a trap with a mid-gap state an energy E_t is given by the following equation [27],

$$\mathcal{R}_{SRH} = \frac{c_n c_p (np - n_i^2)}{c_n n (1 + e^{(E_t - E_{Fn})/kT}) + c_p p (1 + e^{(E_{Fp} - E_t)/kT})} \quad (2.5.5)$$

where n and p are the electron and hole concentrations, E_{Fn} and E_{Fp} are the quasi-Fermi levels (QFLs) for electrons and holes, and c_n and c_p are the electron and hole capture rates by the trap level.

If the QFLs are far from the trap level, compared to kT ($E_{Fn} - E_t \gg kT$ and $E_t - E_{Fp} \gg kT$) and the electrons and holes are far out of equilibrium ($np \gg n_i^2$) then Eq. (2.5.5) simplifies to

$$\mathcal{R}_{SRH} \cong \frac{c_n c_p np}{c_n n + c_p p} \quad (2.5.6)$$

and if one of the terms in the denominator is much larger than the other, then it becomes even simpler. If electron capture is much faster than hole capture, then the product $c_n n$ dominates the denominator and Eq. (2.5.6) is approximately

$$\mathcal{R}_{SRH} \cong \frac{c_n c_p n p}{c_n n} = c_p p \quad (2.5.7)$$

and similarly for the converse when hole capture is much faster than electron capture, where the SRH rate is instead $\mathcal{R}_{SRH} \cong c_n n$. In both cases, the SRH rate becomes linear in either the electron or the hole concentration.

For non-degenerate carrier densities, the band-to-band radiative recombination rate (in a direct bandgap semiconductor like the III-nitrides) is proportional to the product of the densities of electrons and holes since it occurs in a single step [28].

$$\mathcal{R}_{rad} = B(np - n_i^2) \cong Bnp \quad (2.5.8)$$

Often the electron and hole concentrations are assumed to be approximately equal ($n \sim p$) when there is sufficient current being injected into the active region. In this case then the sum of the SRH and radiative rates can be written as

$$\mathcal{R}_{TOT} \cong An + Bn^2 \quad (2.5.9)$$

where A is equal to either C_n or C_p , depending on the relevant traps.

At low carrier densities the SRH recombination rate will dominate the radiative rate, but as carrier density increases the radiative recombination will quickly outstrip the SRH rate. In the absence of any other recombination processes, this means the radiative efficiency of a QW will be given by the following equation,

$$\eta_{rad} = \frac{\mathcal{R}_{rad}}{\mathcal{R}_{TOT}} \cong \frac{Bn^2}{An + Bn^2} \quad (2.5.10)$$

This efficiency is plotted versus current density in Figure 2.5.1, for several values of the SRH coefficient, A , (representing different defect concentrations). The efficiency tends to 100% at high carrier densities as the SRH rate becomes insignificant. The current densities

were calculated using the following expression, which assumes that the injection efficiency is 100%:

$$J = qd_{QW} \cdot \mathcal{R}_{TOT} = qd_{QW} \cdot (An + Bn^2) \quad (2.5.11)$$

The QW thickness, d_{QW} , was taken to be a typical value of 3 nm.

Unfortunately, there is a third recombination process which can occur, namely Auger recombination [29]–[31]. Instead of producing phonons in a defect-mediated recombination process, like SRH, or producing a photon as in radiative recombination, an electron-hole pair which recombines by an Auger process – in analogy with the eponymous Auger process which occurs in atoms – gives its energy to another carrier. That high energy 'hot' carrier may be either an electron or a hole, leading to two types of direct, band-to-band Auger processes in semiconductors. If a hot electron is produced, the recombination process is called *eeh* Auger (since it involves two electrons and one hole). Similarly, if a hot hole is produced it is called an *ehh* Auger process. The *eeh* Auger rate can be written

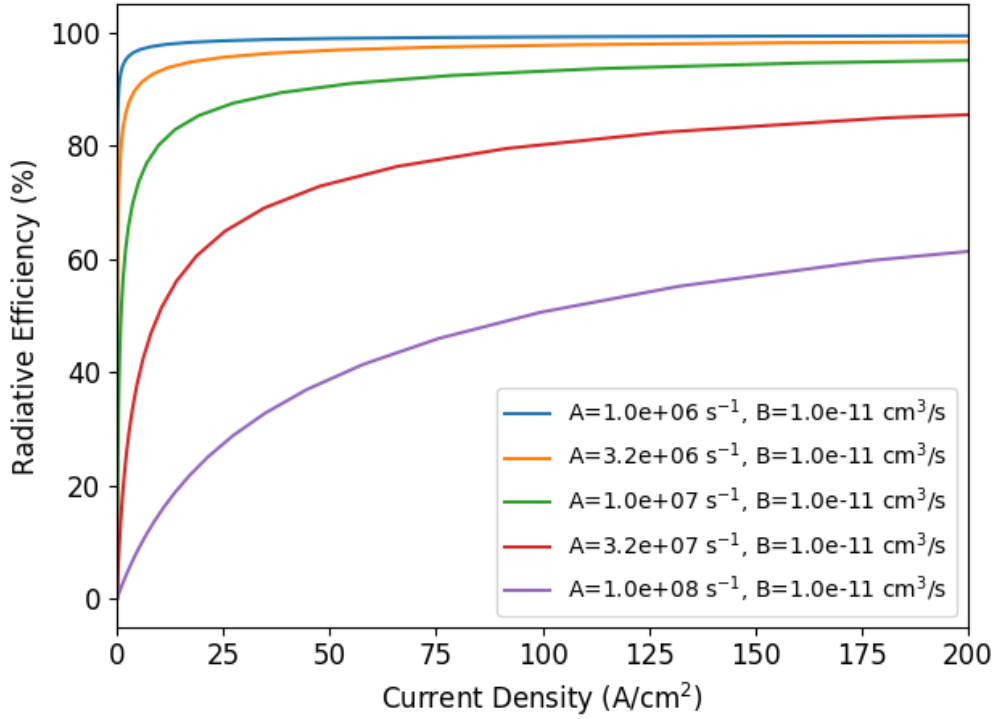


Figure 2.5.1: The radiative efficiency of a 3 nm single quantum well in the ‘AB model’ for various values of the Shockley-Read-Hall rate coefficient. The efficiency tends to 100% at high current density as the radiative rate eventually dominates the recombination current.

$$\mathcal{R}_{eeh} = C_n n(np - n_i^2) \cong C_n nnp \quad (2.5.12)$$

where C_n is the eeh Auger rate coefficient. The approximation is valid when $n_i^2 \ll np$. The extra factor of n occurs because there has to be another electron around to accept the energy from the recombining electron-hole pair. The situation is analogous for ehh Auger, except the rate is proportional to an extra factor of p instead. In the high injection limit ($n \sim p$) they both become approximately equal to

$$\mathcal{R}_{Auger} = C_n nnp + C_p npp \cong Cn^3 \quad (2.5.13)$$

where C is the effective Auger recombination rate coefficient for the combination of both processes.

Adding Auger recombination into the mix, the radiative efficiency of a QW is now given by

$$\eta_{rad} \cong \frac{Bn^2}{An + Bn^2 + Cn^3} \quad (2.5.14)$$

which, due to the conventional choice of symbols for the rate coefficients, gives the name "ABC Model" for the efficiency in III-nitride LEDs. The radiative efficiency, including the Auger term, is plotted in Figure 2.5.2 for various values of the rate coefficients, against current density given by Eq. (2.5.15) below:

$$J = qd_{QW} \cdot \mathcal{R}_{TOT} = qd_{QW} \cdot (An + Bn^2 + Cn^3) \quad (2.5.15)$$

It is clear that Auger recombination causes the radiative efficiency in the QW to decrease after a certain point. This phenomenon is observed in the EQE of real LEDs and is referred to as "efficiency droop". There is, however, considerable debate in the literature about whether or not Auger recombination is the dominant mechanism behind droop. The arguments for and against are briefly reviewed in the next section.

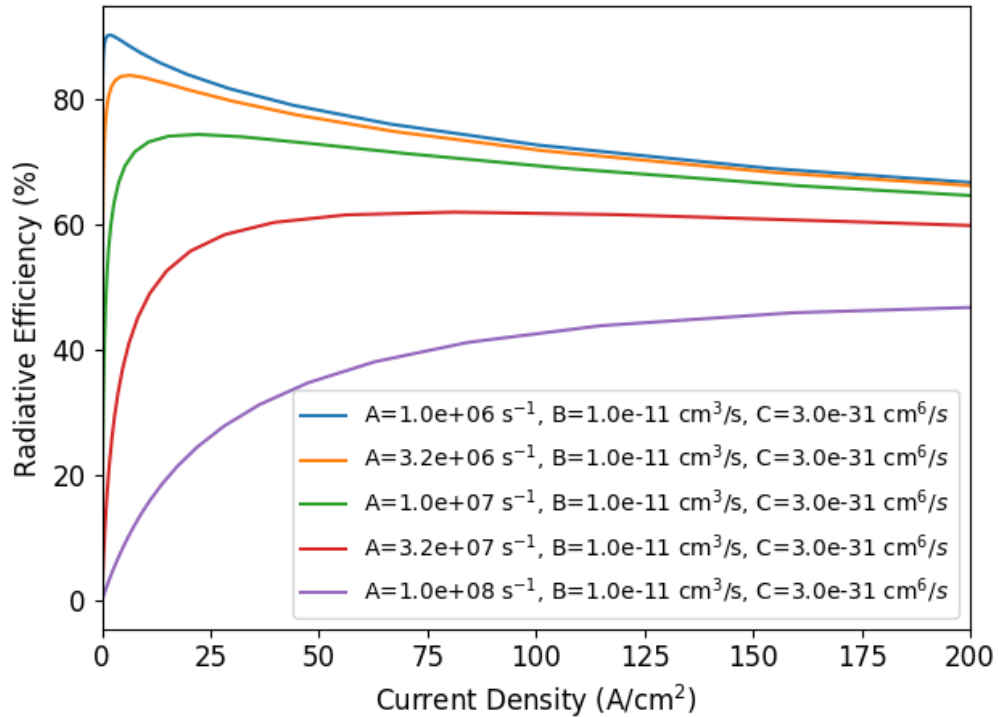


Figure 2.5.2: The radiative efficiency of a 3 nm single quantum well in the ‘ABC model’ for various values of the Shockley-Read-Hall rate coefficient. Unlike in the ‘AB model,’ the efficiency now peaks, and then begins to droop. The current density at which the peak occurs depends on the SRH rate coefficient. For a high enough value of the SRH coefficient, the peak moves out to current densities beyond the typical operating regime of LEDs, and the efficiency curve again looks like the ‘AB model’ curves, except the apparent asymptote is <100%.

2.6 Models of Efficiency Droop in III-Nitride LEDs

There is a heated debate in the literature over the origin of efficiency droop in III-nitride LEDs. What follows in this section is a brief review of the controversy. The aim is not to be comprehensive, but instead to sketch for the reader an outline of the published models of efficiency droop and provide some context for the work presented in the remainder of this dissertation.

Broadly, there are two categories of droop theories: 1) those that attribute it to decreasing injection efficiency with increasing diode bias, and 2) those that attribute it to decreasing radiative efficiency in the QW(s).

The injection efficiency of III-nitride LEDs is often assumed (by virtue of much hand-waving) to be 100%. Plausible arguments for this are that good LEDs usually exhibit significant recombination current at voltages below the built-in voltage of the GaN pn-junction (~3.3 V) so that there can be little minority carrier diffusion current in parallel with it, and that the QW(s) are deep enough in the nitrides that thermionic emission current of carriers out the potential well is negligible.

Questioning this assumption, there are a considerable number of articles devoted to the idea that droop is caused by poor injection efficiency, i.e. – high minority carrier diffusion current. This is thought to occur in GaAs double heterostructure (DH) lasers, largely by thermionic emission of carriers out of the potential well [32], where the depth of the potential well(s) in the active region of GaAs devices is typically lower than in nitride devices due to the smaller bandgap of the arsenides. The authors of Ref. [32] also consider minority carrier diffusion current across the junction, but conclude that even in GaAs where the bandgap is less than half that in GaN, it is a small component of the leakage current.

One published analytical model of what is called "carrier leakage" past the active region in nitride LEDs published in the literature is a modified version of the ABC model where the denominator has higher order terms in the carrier density in the quantum wells [33]. The authors claim that the minority carrier diffusion current in the junction flowing in parallel with the recombination current in the device, is given by a polynomial function of the bound carrier density in the quantum wells, conveniently similar to the ABC model which fits EQE curves

reasonably well. The argument they use to derive their mathematical model is circular however. They repeatedly substitute an expression into itself to obtain the higher order terms in their current expression, up to the sixth degree (the procedure beginning with Eq. 7 of [33]). The higher order polynomial model does appear to fit efficiency droop data better, as to be expected with the additional degrees of freedom, but has no solid relationship to the physical phenomenon of carrier leakage.

Other authors argue for reduced injection efficiency as the cause of droop based on observations of decreased droop in the relative EQE of LEDs that have modified epi structures with respect to a reference LED structure [34]–[36]. However, unless the epi structures being compared are nearly identical in material quality (in terms of defect density and impurity concentration), then variations in the amount of defect-related non-radiative recombination can lead to variation in the onset of efficiency droop. This would manifest in a lower absolute EQE, which was not reported, as well as less apparent droop. This is because a shorter SRH recombination lifetime, all other things equal, will increase the current density at which EQE peaks. In the extreme case, this can cause an LED to appear to have reduced or non-existent droop, though in actuality the droop has simply been pushed out to higher current densities beyond the measured range. This is illustrated in Figure 2.5.2, where the curve with the highest SRH rate coefficient appears not to droop in the range of current densities plotted.

Considering that state-of-the-art commercial LEDs still droop today and that an industry understandably hungry to eliminate droop would have surely tried these authors' recommendations, the simplest explanation for their results is that the authors simply had material with significantly different SRH lifetimes and their recommendations do not work in

commercial material, which is always of higher and more consistent quality than university-grown material.

In the second category of droop theories – centered on the idea that droop is a decrease in the radiative efficiency of the active region, and not in the injection efficiency – there are two main proposals. The first is that carriers bound in the quantum wells gradually become more delocalized as the localized states created by random alloy fluctuations in the InGaN fill up at higher injection levels [37]–[42]. As they do, the effective SRH rate increases since the delocalized carriers interact more strongly with threading dislocations (of which there are typically many). The second proposal is that Auger recombination begins to dominate the recombination current at higher injection levels, leading to a decrease in the radiative efficiency in the quantum wells [7], [43], [44]. These two proposals will now be discussed briefly.

III-nitride LEDs have large numbers of threading dislocations, when grown on foreign substrates. These act as non-radiative recombination centers when they thread the QW layers. In fact, they occur in such high densities ($\sim 10^8 \text{ cm}^{-2}$) that the non-radiative lifetime in the quantum wells could be expected to be so short that very little light would ever be emitted. To explain this conundrum (light is definitely emitted), it has been proposed [37]–[42] that the localization of carriers in high indium regions of the QWs helps the carriers to avoid most of the dislocations, and further concentrates them so that the effective carrier concentration is also higher.

These authors argue that as more carriers are injected into the active region, the localized states fill up so that additional carriers will – at some point – begin to occupy delocalized states. These delocalized states extend over larger volumes of the QW, and end up interacting more

strongly with dislocations as a result. This is supposed to increase the net non-radiative SRH recombination rate and hence has been proposed to be the cause of efficiency droop by the authors, though they offer no estimate of the magnitude of the droop that could be expected from this mechanism.

The second proposal to explain efficiency droop by a decrease in the radiative efficiency of the QWs is that Auger recombination begins to dominate the lifetime at high carrier densities. It is the third, highest order term in the ABC model of efficiency, and, as can easily be seen by taking the limit of the ABC efficiency equation at high carrier density, it would cause the radiative efficiency to decrease as $1/n$, or $1/L^{1/2}$ (since light output is proportional to n^2). This model often provides a very good approximation to what is observed, even in MQW LEDs, and unlike the 6th order polynomial model of [33], is grounded fairly well in semiconductor physics.

Thus, Auger recombination would seem to be a plausible explanation for efficiency droop. However, direct band-to-band Auger rates decrease with increasing bandgap so that the rate coefficient in InGaN quantum wells would have to be several orders of magnitude higher than theoretical calculated values to explain the amount of droop observed in real LEDs [44], [45]. This is often pointed out in the literature by the proponents of carrier leakage-mediated droop (for example, in Section 2.2 of [46]), since if Auger recombination can be eliminated as a likely cause, the most probable candidate remaining is carrier leakage.

The Auger theory is not dead yet though as the calculated rates for indirect, or phonon-assisted, Auger processes in InGaN are high enough to explain the droop behavior of III-nitride LEDs [44]. Indeed, the some of the authors of [37]–[42], proponents of the delocalization theory of droop, have also commented that indirect-Auger recombination could be the cause

of efficiency droop [47]. Additionally, the broken symmetry perpendicular to the plane of the QW(s) has been shown to enhance the Auger rate [48], offering another explanation for why Auger processes in LED QWs appear to be more dominant than the bulk Auger rate would suggest.

More recently Shahmohammadi, et al. [49] have shown that localization of carriers, even at high carrier densities, also enhances Auger recombination in InGaN quantum wells, and Vaxenburg, et al. [50] showed that the polarization fields in polar, c-plane InGaN QWs theoretically enhances the Auger recombination rate even further, at the expense of the radiative recombination rate.

Work by Iveland, et al. [7] has shown that some fraction of the electrons emitted from the cesiated surface of an operating LED into vacuum have high enough energies above the bulk conduction band minimum that they could only have originated from Auger recombination process somewhere within the LED (the active region being the most likely place, by far). This is a *direct observation* of the result of a hot electron-producing Auger process within the LED, and so confirms the existence of Auger recombination within the device.

This technique, called electro-emission spectroscopy (EES), has limitations however. The main one being that it can only detect the signature of *eeh* Auger, because hot holes from *ehh* processes cannot be emitted into vacuum. Additionally, only a small and uncertain fraction of the hot electrons escape the device into vacuum, so it is difficult to say on the basis of these experiments alone whether Auger recombination is the dominant cause of efficiency droop, though it certainly appears to be well correlated with the non-radiative current at high current densities [7]. The work presented in the subsequent chapters of this dissertation represents the first stages of development of a complementary (and indirect) technique to detect Auger

recombination within a III-nitride LEDs which may someday allow us to say definitively that Auger recombination is the dominant cause of droop.

2.7 Photo-Induced Currents in Semiconductor Devices

This dissertation is about photocurrent in LEDs under high forward bias. Therefore it will be useful to briefly discuss the electrical behavior of semiconductor devices, and especially QW pn-junction devices, under optical illumination.

The simplest case is that of a slab of semiconductor with two identical Ohmic contacts on it, separated by some distance. The semiconductor will have some conductivity in the dark, depending on the temperature, its bandgap, and how it is doped, if at all. This conductivity, σ_{dark} , can be given by the expression,

$$\sigma_{dark} = qn\mu_n + qp\mu_p \quad (2.7.1)$$

where μ_n and μ_p are the electron and hole mobilities.

If the semiconductor is then illuminated between the contacts with photons with energy greater than the bandgap of the device, some of those photons will be absorbed. Consequently, the carrier densities will increase as electron-hole pairs are generated by the absorbed photons. The above expression shows that if the carrier densities increase, the conductivity must also increase. This phenomenon is called photoconductivity.

After the light is turned on, the conductivity will be

$$\sigma_{light} = q(n + \Delta n)\mu_n + q(p + \Delta p)\mu_p > \sigma_{dark} \quad (2.7.2)$$

Thus, for the same applied bias across the device, the current will increase under illumination. It will be seen in subsequent chapters that this is also what appears to happen in forward biased QW LEDs where carriers are directly excited into the QW(s) by light that has an energy above

the QW bandgap, but below the bandgap everywhere else in the device (so-called "resonant excitation"). The behavior of the LEDs only bears a superficial resemblance to this kind of photoconductivity, however, as the photo-generated electron-hole pairs in the LED are generated into bound states in the QWs and cannot increase the overall conductivity of the device without first escaping the QWs. Understanding the ways this escape may happen is at the core of this work.

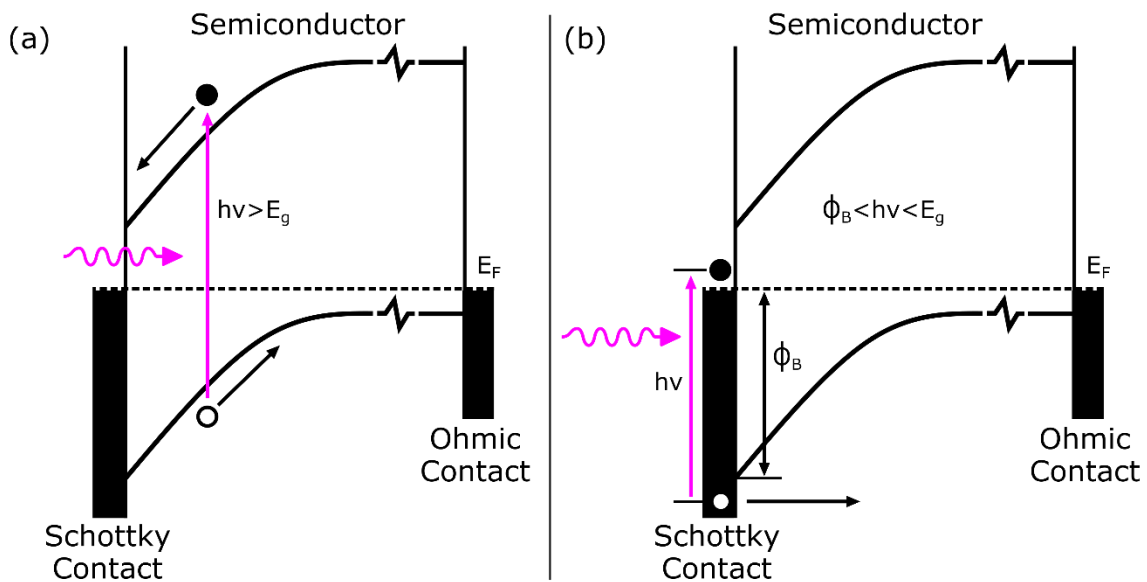


Figure 2.7.1: Illuminated Schottky barrier photodiodes at 0V, excited with (a) above bandgap, and (b) below bandgap photons. In (a), the above bandgap light excites electron-hole pairs into the band-bending region where the electric field separates them and causes current flow. In (b), the below bandgap excitation is absorbed in the metal Schottky contact and the hot hole is emitted into the semiconductor where it is accelerated by the electric field towards the Ohmic contact. The process depicted in (b) is referred to as internal photoemission (IPE).

Schottky barrier diodes also have a photoresponse, though it is more complicated than simple photoconductivity. A schematic band diagram of such a device is shown in Figure 2.7.1 for a p-type semiconductor. If the illumination is of an energy greater than the bandgap of the semiconductor, then any light absorbed in the band-bending region (BBR) of the diode generates electron-hole pairs which are separated by the electric field in the BBR. This causes

current to flow in the device in the reverse direction (shown in Figure 2.7.1(a)). If the contacts are left open so no net current can flow, a forward voltage will develop instead to counteract the reverse photocurrent (i.e. – the Schottky contact will develop a negative voltage relative to the bulk semiconductor). This voltage is called the open-circuit voltage.

If the light is instead of an energy less than the bandgap in the semiconductor, photocurrent may still result but it is a bit more subtle to understand. The sub-bandgap light cannot generate electron-hole pairs within the semiconductor, so the light must be absorbed in the contact metal, near the interface with the semiconductor. There, the light will generate hot carriers within the metal. If those carriers are generated close enough to the interface, they may enter the BBR in the semiconductor. In the case of a p-type diode, if the carrier is a hot electron it will be swept back into the metal, and if it is a hot hole it will be swept into the semiconductor. This hot hole produces photocurrent on its own by a process called internal photoemission (IPE), shown in Figure 2.7.1(b). More on IPE in Schottky diodes can be found in Ref.'s [51], [52].

If the hot hole has enough energy (as determined by the photon energy, the bandgap, the barrier height, and the bias on the diode), it may also generate photocurrent by generating of an electron-hole pair in the BBR by impact ionization. This is shown in Figure 2.7.2. The field in the BBR will separate the generated carriers and cause additional current to flow, just as in the case of above bandgap light. This will be more likely to occur as the BBR becomes thinner than the impact ionization distance in the semiconductor, as the hot carrier may simply lose energy to phonons before it can cause impact ionization if the BBR is too thick.²

² The mean free path for hot holes in p-GaN does not appear to be well known. However, the LO phonon relaxation time of hot holes in p-GaN is known to be approximately 0.6 ps (see Ref. [53]), which implies a mean free path on the order of 60 nm (assuming a velocity of $\sim 10^7$ cm/s). If the BBR is much wider than this, impact ionization will not occur because the hot holes will lose energy to LO phonon scattering.

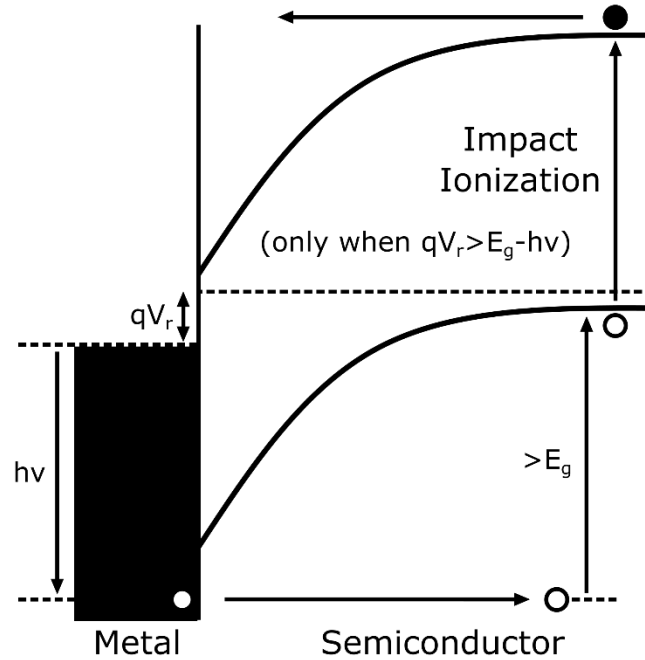


Figure 2.7.2: Hot hole generation and subgap photocurrent in a reverse biased p-type Schottky junction. When the energy of the incoming photon is less than the bandgap of the semiconductor the junction must be reverse biased or the hot holes will not have enough energy to cause impact ionization. Additionally, the band-bending must happen over a distance shorter than the mean free path of the hot hole in the semiconductor, or an even greater reverse bias is necessary to overcome the energy lost by the hot hole as it scatters.

Generally, this kind of impact ionization-induced photocurrent in Schottky diodes, with below bandgap excitation, requires the diode to be reverse biased. This is precisely the condition that rectifying Schottky contacts to LEDs are in when the pn-junction of the LED is forward biased. Generally p-type contacts to GaN are of the Schottky type, but in good contacts the surface layer is doped very heavily to allow holes to tunnel into the semiconductor through the ultra-thin ($<3\text{nm}$) BBR. If tunneling occurs, the voltage drop across the BBR is never great enough at the current densities the LEDs are operated at, for photocurrent to flow. However, if the BBR is too thick to allow tunneling current to flow, but still thin enough to allow impact ionization to occur (as may occur in only slightly rectifying contacts), then those contacts may generate some photocurrent in addition to whatever is going on in the active

region of the device. This will become important in Chapter 4, as the photocurrent due to slightly rectifying contacts may represent a small portion of the measured value in the SQW LEDs discussed in that chapter.

LEDs are fundamentally pn-junction devices, and the junction field in pn-diodes can separate photo-generated carriers just like the field in the BBR of a Schottky barrier diode can under above bandgap illumination. Thus, pn-junctions can also generate photocurrent in reverse bias. Below is a schematic of the typical change in the current-voltage (IV) characteristic of pn-junction devices under reverse bias. This behavior is observed in junctions with and without QWs, as long as there is light absorbed in the junction of the device. In a pure pn-junction device, this means light with energy above the bandgap of the material forming the junction. Adding one or more QWs to the junction region of a pn-junction device extends the absorption of the device below the bandgap of the junction material. The device is still transparent to light below the absorption edge of the QW layers however.

Reverse biases applied to the junction increase the junction field, and thus the rate at which photo-excited carriers are swept towards the contacts, up to a point. In a QW junction device, the rate of escape of the carriers out of the well(s) typically limits the current. After the current is limited by the escape rate, the photocurrent is simply proportional to the intensity of the incident light. This proportionality makes reverse biased pn-junction devices useful as photodetectors. Any pn-junction device can be operated in this regime – even LEDs. However, commercial photodetectors are typically designed specifically to operate in this regime, while LED structures operated as photodetectors typically have much lower efficiencies as such. Additionally, commercial photodetectors, which are sometimes made

from indirect bandgap semiconductors like silicon or germanium, which would make poor LEDs due to their comparatively lower radiative recombination rates.³

There are typically two mechanisms by which carriers that are resonantly photo-excited into the QW(s) may escape in a reverse biased QW junction device. The first is thermionic emission, where carriers overcome the potential barrier by absorbing thermal energy. After they acquire enough energy to escape the potential well, the junction field sweeps the majority of them in the reverse direction. A fraction do diffuse in the forward direction, as minority carriers, but since the overall barrier is much higher in that direction it is a vanishingly small amount.

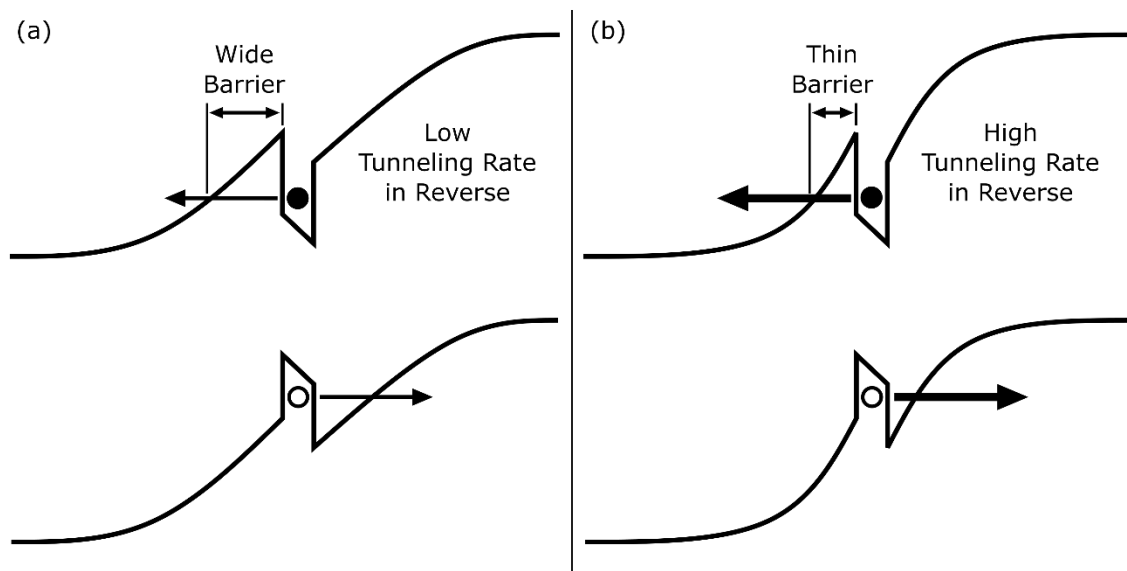


Figure 2.7.3: Schematics of showing tunneling escape from the QW of a SQW LED, through (a) wide barriers and (b) thin barriers ($\sim < 3$ nm). The higher junction field in (b) compared to that in (a) is necessary to decrease the barrier width and facilitate tunneling.

³ Astonishingly, silicon devices designed specifically as LEDs can have respectable radiative efficiencies of almost 1% however (see Ref. [54]).

The second escape mechanism is quantum mechanical tunneling. For carriers to tunnel out of a potential well, the barrier must be thin enough (typically on the order of ~ 3 nm or less). This requires high junction fields, and carriers may only tunnel out of the well in the reverse direction.

If a pn-junction device is biased in the forward direction in the dark, then a small forward current flows, before the device is considered turned on, as soon as the bias is larger than kT/q . As long as the magnitude of this dark current is smaller than the magnitude photocurrent there will be a net reverse current once the junction is illuminated. This is shown in Figure 2.7.4. The possible mechanisms for the photocurrent are unchanged.

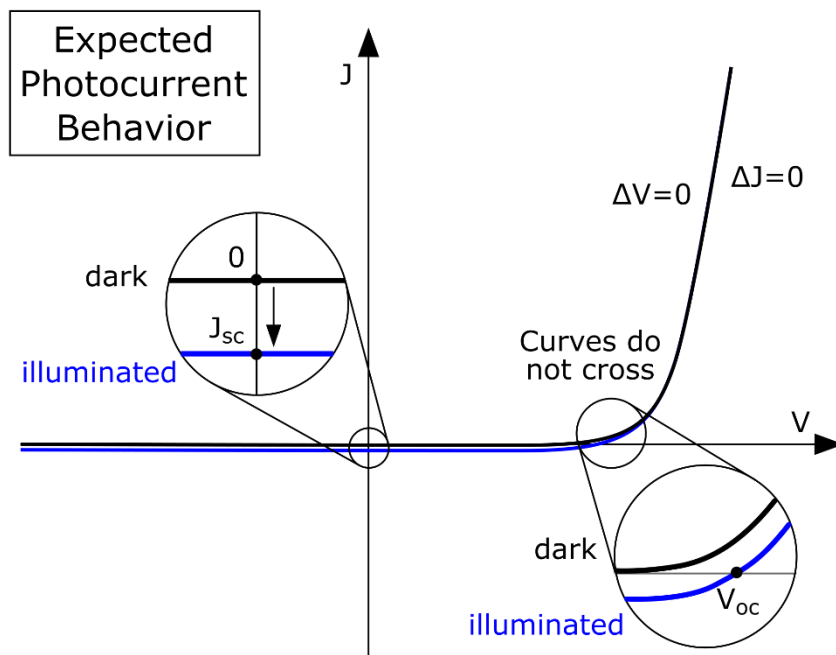


Figure 2.7.4: Schematic of the dark (black) and illuminated (blue) current density vs voltage curve of a typical QW junction device, showing the photocurrent in reverse (left) and forward (right) bias. The point where the current goes to zero on the illuminated curve is the open circuit voltage, V_{oc} . The current where the voltage is zero on the illuminated curve is the short circuit current, J_{sc} . The photocurrent (and voltage change) approaches zero as the forward bias increases.

Increasing the forward bias, eventually, the net current in the illuminated device goes to zero, at a bias called the 'open-circuit voltage'. Above this bias, the typical picture of photocurrent in QW junction devices predicts that the photocurrent should rapidly approach zero. This is depicted in Figure 2.7.4, where the blue curve represents the illuminated IV characteristic of the device, and the black curve is the IV characteristic in the dark.

This dissertation is about what happens in III-nitride QW LEDs – which do not follow the expected photocurrent behavior for QW junction devices – at biases above the open-circuit voltage, when the dark current in the diode is no longer small. At high forward biases the photocurrent is observed to be a *forward current*, adding to the dark current to produce a net increase in the total current in the device. At some point slightly beyond the open-circuit voltage, the net photocurrent goes to zero, and subsequently switches sign to become positive (N.B. – this also necessarily means that the voltage change upon illumination becomes negative at the same time). This is shown in Figure 2.7.5. This phenomenon has been reported before, in blue LEDs [55], and green LEDs [56], though the published explanations have so far been inadequate, as will be discussed in later chapters.

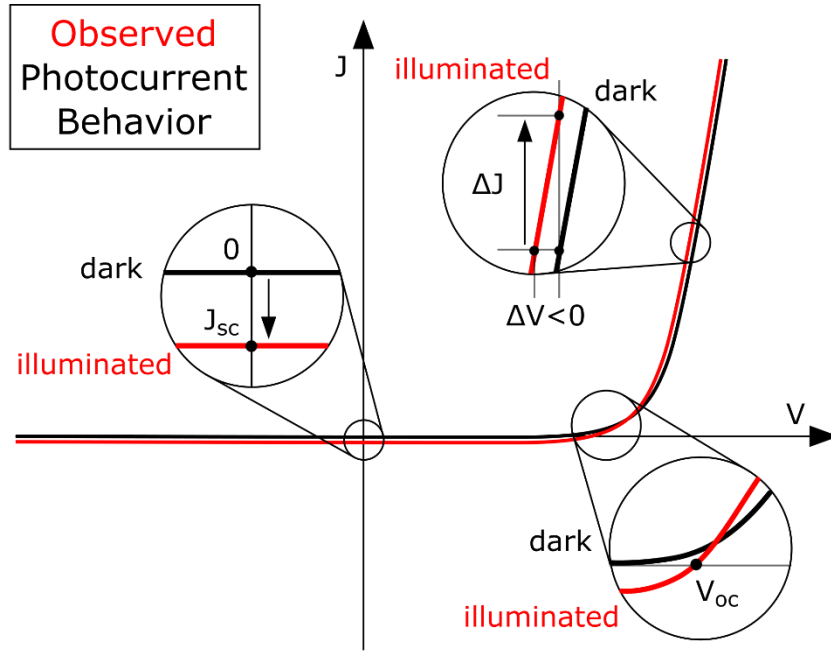


Figure 2.7.5: Schematic of the dark (black) and illuminated (red) current density vs voltage curve of a typical QW III-Nitride LED, showing the photocurrent in reverse (left) and forward (right) bias. The point where the current goes to zero on the illuminated curve is the open circuit voltage, V_{oc} . The current where the voltage is zero on the illuminated curve is the short circuit current, J_{sc} . The photocurrent becomes zero and then reverses sign to become positive, above V_{oc} . The photo-induced voltage change also changes sign and becomes negative.

3 Methods and Apparatus

3.1 Overview of the Measurement Problem

In the simplest measurement of the photocurrent in a diode, all that is needed are a light source, a voltage source, and a current meter. The diode must have two electrical contacts (one to the anode and one to the cathode) and an optical window to allow the light to impinge on the junction. The current is measured with the junction illuminated and in the dark, and the photocurrent is found by simply taking the difference between the two values. If the diode emits light and the photo-induced change in light output of the diode is of interest, then a photodetector is also needed. Collection optics to improve the signal are optional. That's it.

As this apparently simple technique relies on taking the difference between two measurements, there are, however, some limitations. If the photocurrent is small compared to the dark current through the diode, then this approach can lead to a large error in the extracted photocurrent.

This is, unfortunately, precisely the situation to be found in forward biased light emitting diodes (LEDs), where the current in the dark can be as large as 100 A/cm^2 , while the photocurrent may be only a few mA/cm^2 , even at several W/cm^2 incident power. So, to make an accurate measurement of the photocurrent in forward bias, more sophisticated measures will be needed. These will be described in the following.

The relatively small photocurrent necessitates the use of lock-in detection to separate the photoresponse from the much larger dark current. Lock-in amplifiers are very useful laboratory tools, for a variety of purposes. When they are used to detect very low DC signals against a large DC background they function as a high Q bandpass filter. In this mode, a very

low frequency carrier signal is added to the optical excitation by chopping it with a perforated wheel. This shifts the excitation in frequency space away from 0 Hz where the lock-in amplifier can select out the now AC (~80 Hz) photoresponse from the DC background. The lock-in amplifier outputs a voltage, typically from 0-10 V, which corresponds to the root-mean-square (rms) amplitude of the input signal. In addition, if the input signal was a square wave instead of sinusoidal, the lock-in amplifier output only reflects the rms amplitude of the first harmonic component of the square wave. This is an artifact of the way the lock-in filters out the input signal from the background by using the orthogonality of sines. Therefore, if the peak-to-peak amplitude of the square wave input is desired (i.e. – the difference between the current in the illuminated and dark states) then the lock-in output must be multiplied by the following correction factor,

$$V_{pp} = 2 \times \sqrt{2} \times \frac{\pi}{4} \times V_{out} = \frac{\pi}{\sqrt{2}} \times V_{out} \quad (3.1.1)$$

where V_{out} is the output voltage of the lock-in. The factor of $2 \times \sqrt{2}$ goes from rms amplitude to peak-to-peak amplitude, and the $\pi/4$ accounts for the lock-in measuring only the first harmonic of a square wave (the first Fourier coefficient in the expansion of a square wave is $4/\pi$).⁴

Another subtlety of practical measurements on forward-biased LEDs is that they typically dissipate quite a bit of heat when driven into the droop regime. As this dissertation is aimed at studying the origin of efficiency droop, the self-heating of the diode in this regime cannot be neglected. A quick calculation shows that a blue LED operating at ~4 V at ~100 A/cm² will consume 400 W/cm² of electrical power and if its wall plug efficiency (WPE) at 100 A/cm² is

⁴ For more information on lock-in amplifiers, see Ref. [57].

50%, then 200 W/cm^2 will be converted to optical output power, leaving 200 W/cm^2 to heat the device. For the device area used in this work, 0.1 mm^2 , this is 200 mW of heat. Self-heating is a significant enough problem that commercial packaged LEDs with modest heat sinking can still reach temperatures $>100 \text{ }^\circ\text{C}$ [58] under typical operating conditions.

Several things in an LED change with temperature, including the recombination rates in the active region and the minority carrier diffusion current across the junction. All of these changes conspire to cause the current to increase, for a constant applied bias, with increasing temperature. The effect is exacerbated at high drive currents and will interfere with attempts to measure the photocurrent, which will be shown in subsequent chapters to also be an increase in current. Performing the measurement on devices which are left on-wafer instead of singulated, with good heat sinking, will help to mitigate some of these effects. When left on-wafer, the large wafer area helps to spread the heat away from the device mesa more effectively than a much smaller 1 mm^2 die would.

In addition to measuring on-wafer devices with proper heat sinking, performing the measurement of the photocurrent as a function of bias in a randomized order – instead of sweeping, from low to high or high to low bias as is common practice in academic groups – converts any residual systematic errors due to self-heating into random scatter in the measured photocurrent data. This is important because in a sweep the measurement is typically performed quite quickly compared to the thermal time constant of the system and the effects of the heating during measurement of high current density data points can add on top of each other. However, in a randomized measurement, low current density data points are likely to follow the high current density ones, allow the LED time to cool.

More constraints arise when we consider the effects of contact geometry and current crowding on the measured values of the photocurrent, especially if we wish to be quantitative in our analysis of the photoresponse. These issues and the steps taken to mitigate them will be discussed in the next section.

3.2 Device Structure

The central problem of designing a suitable device structure for measuring the photocurrent in forward-biased LEDs is to create the greatest overlap between the electrically and optically injected areas of the device. LEDs manufactured from GaN grown on sapphire substrates cannot utilize a back-side contact to for the n-type contact, since the sapphire is insulating, and instead must use the conventional geometry shown in Figure 3.2.1(a).

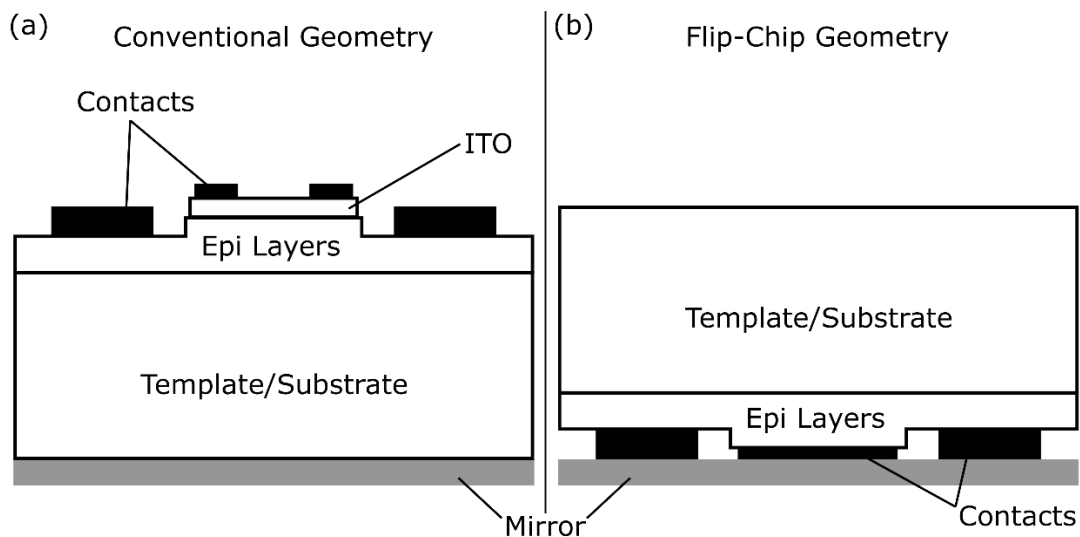


Figure 3.2.1 Comparison of the conventional, p-side up geometry (a) and the flip-chip geometry (b) of LEDs. The contact on top of the etched mesa structure is the p-contact, while the n-contact is in the field surrounding the mesa. In (a), the layer labelled “ITO” is the transparent indium tin oxide (ITO) current spreading layer used to allow light to escape out of the top of the mesa. In either geometry, the device is mounted to a reflective surface, labelled “Mirror” in the above.

Current is injected under the p-type contact and proceeds vertically to the bottom of the mesa where it then spreads out laterally to reach the n-type contact. It is possible to cover the entire top of the mesa with the p-contact and flip the structure upside down, using the back of the substrate as a window to the junction of the diode as shown in Figure 3.2.1(b), but this so-called “flip-chip” process is difficult to execute.

In the simpler-to-process conventional geometry the p-type contact can be made to cover only part of the mesa, thereby allowing light to escape out through the top. However, now current is injected only under the p-contact metal, and must spread into the optically injected area of the junction, as shown in Figure 3.2.2. Unless a transparent, conducting window layer such as indium tin oxide (ITO) is used under the contact to help laterally spread the current, there will be highly non-uniform electrical injection in the uniformly optically injected area of the device. And, even if the window layer provided enough current spreading, the contact would always block some of the electrically injected area from the light. This now makes the measurement essentially like having two diodes in parallel with only one being optically pumped, except that there are also numerous leakage paths between them due to the possibility of lateral diffusion of carriers from the optically injected areas to the shadowed ones.

To simplify the analysis of the photocurrent measurements, as well as the device processing, it is simplest to use a semi-transparent metal contact which also acts as a window and current spreading layer, providing high spatial overlap between the electrically and optically injected areas of the mesa when the optical excitation overfills the mesa. This is depicted in Figure 3.2.3. In the practical implementation of this scheme, only a small portion of the mesa near the edge will end up being shadowed by thick metal (required to contact the top of the mesa electrically) and the current spreading is much more uniform.

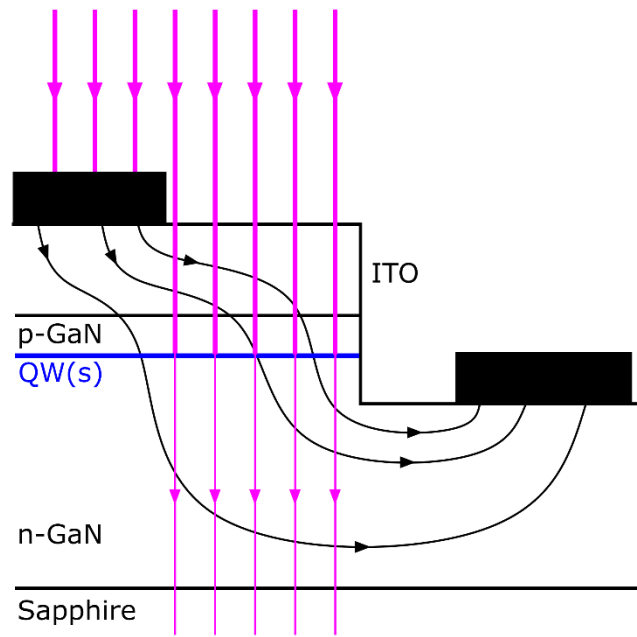


Figure 3.2.2 Schematic showing current crowding and laterally uneven current injection in an LED with an ITO p-contact, as in Figure 3.2.1(a). The thick p-metal also shadows part of the QW(s) from the optical excitation (in violet), but those same regions are still electrically injected.

To make electrical contact to the device from the external circuit, probes or wire-bonds are necessary, both of which require thick (i.e. – opaque) metal pads. Probes are the simplest option from a processing perspective (wire-bonding by hand can be difficult and typically has a low yield). The p-pad, as well as the probe making contact to it, would shadow the optical excitation if it were located on top of the mesa so a dielectric layer (PECVD-deposited SiO_2) is placed over the sidewalls of the mesa to bring the pad and a wire off the mesa without shorting the p-contact to the n-type material underneath the pad. A top down schematic of the device geometry, including the semi-transparent p-contact and the off-mesa pads is shown in Figure 3.2.4. The pads are rather large in diameter (~ 1 mm) to enable probing the devices without the use of a microscope. This limits the density of devices which may be placed on a wafer but not overly so, with the final process allowing 10 devices per cm^2 .

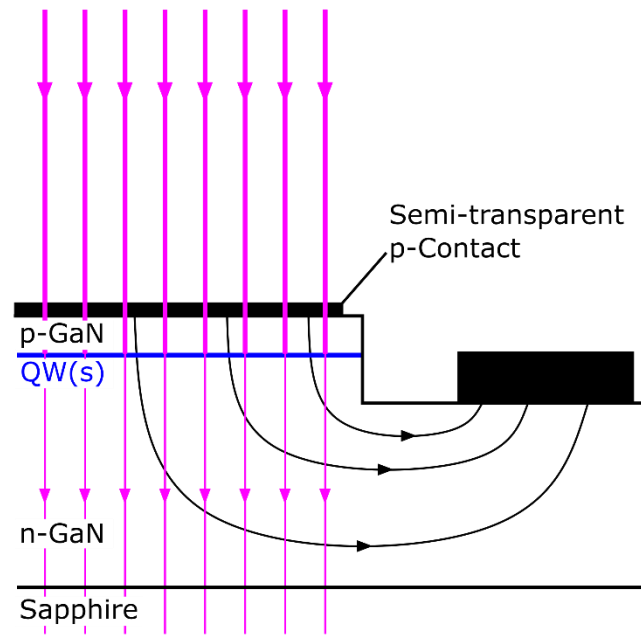


Figure 3.2.3 Schematic showing a conventional LED geometry with a thin, semi-transparent metal p-contact covering almost the entire mesa. This allows for much more uniform injection of current into the QW(s), much more closely matching the uniform optical excitation.

For more details of the nanofabrication process used to make the devices discussed in this dissertation, see Appendix A.

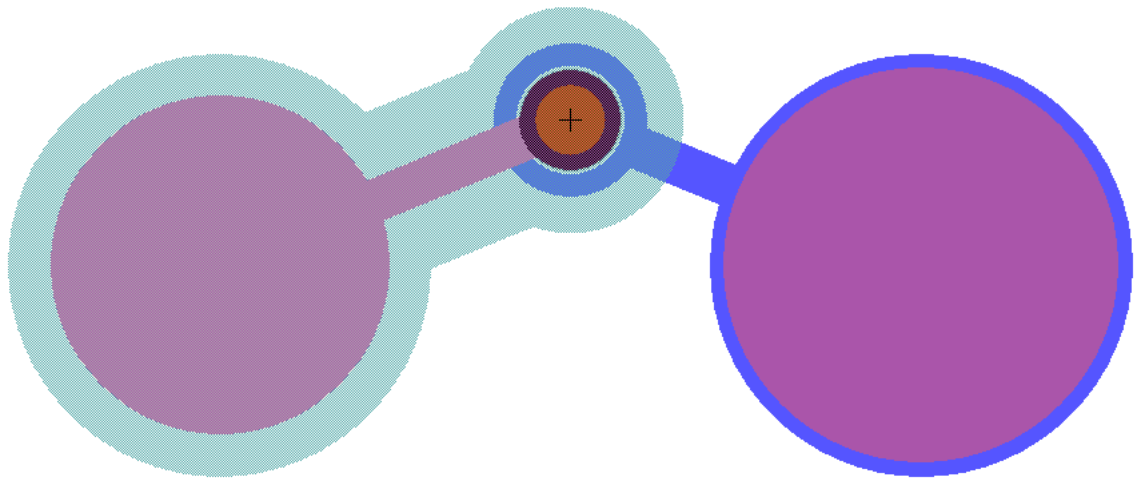


Figure 3.2.4 Top down schematic of the LED geometry used in this dissertation. The schematic was generated from the photomask file and each of the different colors represents a different lithography step. The circular mesa is in the center (orange) and is completely covered by the semi-transparent p-contact metal. The ring around the base of the mesa (blue) is the n-contact. The SiO₂ used to bring the p-pad off of the mesa (teal) completely surrounds the mesa. The n- and p-pad metals are the large circles (purple) on either side of the mesa. There are 10 of these devices per cm² in the processed wafer pieces.

3.3 Optical and Electrical Apparatus

A block diagram of the optical apparatus used for the work presented in this dissertation is shown below in Figure 3.3.1. A 100 mW, output power stabilized, continuous wave (CW) diode laser emitting at 403 nm (Coherent Cube) was used to provide optical excitation of the LED. The laser wavelength was chosen because it is not absorbed in the GaN layers of the LEDs, but only in the InGaN quantum well (QW) layer(s) of the device. The resonant excitation ensures that electron-hole pairs are excited optically only into the junction of the device, into bound states in the QW(s). Knowing this considerably aids in the interpretation of the photocurrent.

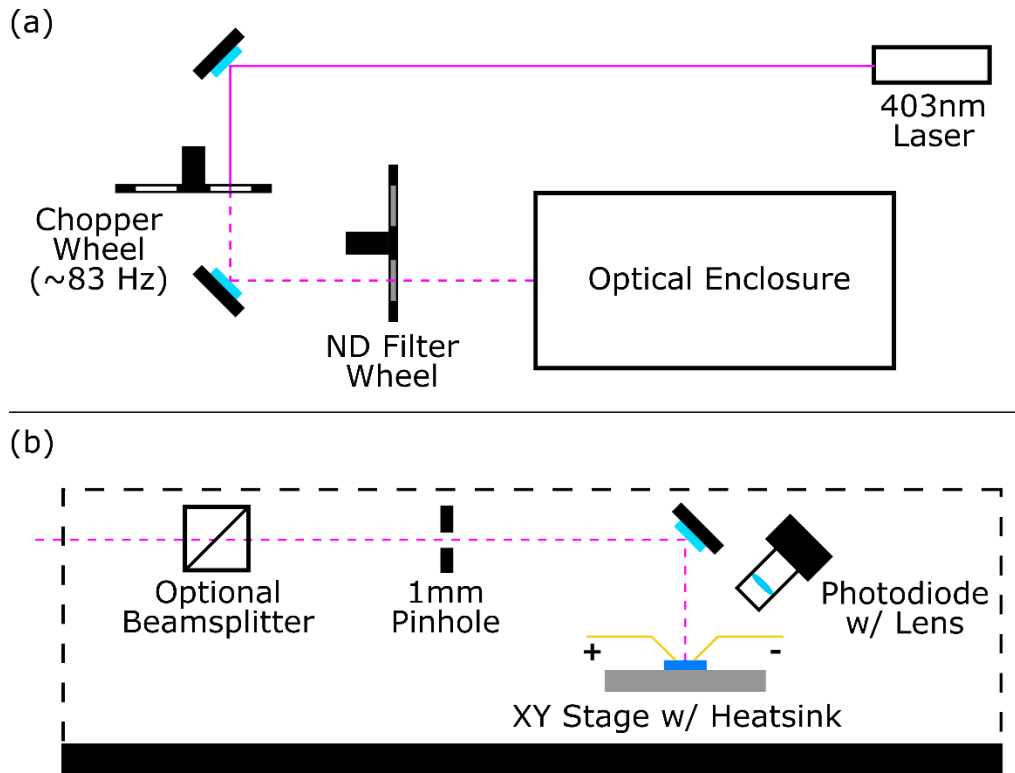


Figure 3.3.1: Schematic of the optical layout of the photocurrent measurement apparatus, showing a top-down view (a) of the whole setup, and a side view (b) of the inside of the optical enclosure.

The laser light is well collimated, by the manufacturer, so no external source collimating optics are necessary. The laser light is steered by a metal mirror through a chopper wheel that has an opening width much larger than the diameter of the laser beam. After the chopper wheel, the laser light is again reflected off of a mirror. It passes through an ND filter wheel which can be used to adjust the incident power density. After the filter wheel, the laser light passes into a black cardboard optical enclosure which helps reduce the effects of stray light, for example, from the computer monitor. Any change in current caused by light into the QW(s) of the LEDs which doesn't pass through the chopper wheel should be ignored by the lock-in amplifier, but any light which does pass through the chopper wheel will be included in the photocurrent signal. The enclosure helps to minimize this but the distance from the chopper

wheel to the LED also helps because of the reduced range of incident angles into the chopper wheel which will end up impinging on the LED. The room lights were also kept off during all measurements to further reduce stray light.

Inside the enclosure, there is an optional beamsplitter which may be inserted into the beam path to allow monitoring the laser power. The Coherent laser output power is very well controlled, and so this is generally unnecessary.

After the beamsplitter, the laser light passes through a 1 mm diameter pinhole that serves two purposes. First, it creates a beam of a known cross-sectional area so that an optical power density can be easily calculated by measuring the power of the laser beam after the pinhole and dividing by the area of the pinhole. A freshly purchased, calibrated photodiode power meter was used for this purpose. The power meter could be taped in the path of the beam after the pinhole to measure the power density, or removed from the beam path to perform the photocurrent measurement, thus capturing the true power density incident on the LED. Without any ND filters in the beam path, the average power density of the collimated 100 mW laser beam after the pinhole was $\sim 5.7 \text{ W/cm}^2$.

Second, the pinhole helps avoid optical pumping of multiple devices at once by an unnecessarily large beam, which would complicate the measurements of photo-induced changes in EL intensity. The device area is, after all, only 0.1 mm^2 . Using a “pinhole” with a 1 mm diameter is only advantageous because it keeps the intensity of the signal measured by the power meter high and because it makes alignment of the laser beam with a device easier. A smaller pinhole could certainly be substituted out if there were ever a need.

After the pinhole, the laser beam reflects off one more metal mirror, down onto the LED, which is mounted horizontally on an aluminum heat sink with thermal paste. The back of the

LED wafer (actually a 11 mm x 11 mm piece) was coated in a black, colloidal graphite paint to prevent the laser light from causing the thermal paste to luminesce, which would interfere with the EL measurements. It also helped to reduce reflections of the laser light off the back surface of the wafer. All of the epi material used in this work were grown on flat (not patterned) sapphire substrates so as to minimize scattering from the GaN/sapphire interface as well.

A thermistor is mounted on the aluminum heat sink, close to the LED wafer piece. The thermistor is the feedback sensor for a thermoelectric cooler, underneath the aluminum heat sink. The thermoelectric cooler controls the temperature of the top of the aluminum heat sink to be 25 °C – slightly above room temperature – using an ILX Lightwave LDT-5500B Temperature Controller. This controller allows some adjustment of the control parameters to tune the response time of the controller to be reasonably close to the response time of the thermal circuit. Parameter values were chosen to minimize overshoot oscillations which could adversely affect the measurement.

Between the heat sink and the thermoelectric cooler was a thin sheet of mu-metal, which was surprisingly found to be necessary to reduce an effect on the LED photocurrent in reverse bias whenever there was a large change in current through the thermoelectric cooler. The photocurrent in reverse bias was observed to change whenever the current through the thermoelectric cooler changed, before the temperature had time to change and independent of the direction of the change in current. Inserting the sheet of mu-metal eliminated the behavior, though the original cause of the behavior remains a mystery. The independence from the sign of the current change and the fact that the photocurrent (essentially the absorption of the QWs) change before the temperature had time to respond implies that it has something to do with the

magnetic field created by the large currents ($\sim 1-3$ A) in the thermoelectric cooler. Regardless, the behavior was eliminated.

A Keithley 2400 sourcemeter was used to drive the LED, in “4W” or 4 wire mode. This removes the voltage drop across the BNC cables supplying current to the device from the voltage measuring circuit. A resistor network, composed of 5 nominally $1\ \Omega$ resistors in parallel, was placed in series with the LED. The overall resistance of the network was measured to be $0.26\ \Omega$. This resistor network was used to measure the current through the LED, by measuring the voltage drop across the network during LED operation. The resistor network acts as a current amplifier with $0.26\ \text{V/A}$ gain, and all reported photocurrent values take this gain into account, along with the lock-in factor discussed previously.

A Thorlabs DET10A, UV-enhanced, battery powered, biased silicon photodiode was used to collect the EL emitted by the LED. A single 1” diameter plano-convex lens mounted in a lens tube was used to increase the solid angle of light captured by the detector. The signal was still quite low, so a FEMTO DLPCA-200 high-gain, low-noise current amplifier was used to amplify it, at $10^7\ \text{V/A}$ gain.

The lock-in amplifier used was a Stanford Research Systems SR830. It was used to measure the photocurrent through the LEDs via the voltage drop across the series resistor network, or the voltage across the LED directly if the LEDs were instead driven in current control. The lock-in was also used to measure the photo-induced change in EL, though this could not be done simultaneously with the photocurrent or photovoltage. When the lock-in amplifier was set to measure the change in EL, the output of the FEMTO amplifier was used as input. The reference signal from the optical chopper wheel was used as the reference input to the lock-in in all cases.

Finally, a Keithley 2000 digital multimeter (DMM) equipped with a multiplexer card, was used to measure the dark voltage across the LED and the output of the FEMTO amplifier in the dark. The multiplexer card allowed both signals to be measured with the same instrument.

The SR830, Keithley 2000, and 2400 were all controlled remotely over a GPIB interface by a custom computer program, written in Python 3. It utilizes the convenient PyVISA package [59] which facilitates GPIB control of instrumentation via a normal, line-by-line computer program, without the need to resort to LabVIEW and the inevitable ‘spaghetti code’ of a typical LabVIEW VI. This author, who has some prior experience with computer programming, found this the easier solution to implement and maintain. Some researchers will of course disagree. Mileage may vary.

The text of the computer control program can be found in Appendix B.

4 Photocurrent in SQW Blue LEDs

This chapter describes the final result of several years of effort to develop the forward biased photocurrent measurement apparatus and determine whether or not it could be used as a technique for studying Auger recombination in III-Nitride LEDs. Several major challenges had to be overcome beyond the design and construction of the measurement apparatus, which was discussed in the previous chapter. Some of these challenges were personal, not technical, as there was a steep learning curve associated with processing semiconductor devices by hand in a cleanroom environment, which I had to climb at an accelerated pace.

In addition to the work in the cleanroom, considerable effort went into understanding the origins of the photocurrent and arriving at a robust argument that the photocurrent in forward bias could only be due to Auger recombination in the quantum well (QW) layer(s) of the LEDs.

First the design of the proof-of-concept experiments presented in this chapter are introduced. Then, the epi structure will be discussed before the results of the photocurrent measurements are presented. Finally, the argument that the photocurrent is due to Auger-generated hot carriers is presented in detail.

4.1 Introduction

The epi structure for the LEDs measured for this work was custom, grown at UCSB by Abdullah Alhassan. It is possible to measure photocurrent in forward biased commercial LEDs, but the sophisticated epi structure and device geometry complicate the analysis unnecessarily for a proof of concept experiment such as presented in this chapter.

The principle simplification in the custom design over the typical commercial epi structure was to use only a single quantum well (SQW) in the active region instead of the ubiquitous multiple quantum well (MQW) active region. It is well known that MQW LEDs suffer from uneven injection of electrons and holes into the QWs of the active region [22]. The conventional explanation for this is that the effective mass of holes is $\sim 5x$ higher than that of electrons in GaN, and that consequently the injected electrons are distributed fairly evenly between the QWs (with slightly higher concentrations in the QWs nearest the n-side of the device), while the injected holes are concentrated mostly in the QW nearest the p-side. Therefore, most of the radiative, and by extension Auger, recombination occurs in the top QW.

When carriers are resonantly photo-excited into the InGaN QWs by above band-gap light at a low intensity, the top QW will experience a slight increase in the generation rate of carriers into the top QW, relative to the rate of electrical injection. However, since holes are not being injected into the other QWs at a high rate, the same intensity of light will produce a larger relative change in the hole concentration in the lower QWs in the MQW active region, due to the longer recombination lifetime.

The difference in photo-response between the top QW and the lower QWs makes it difficult to separate the response of the top QW (where there is potentially significant amounts of Auger recombination occurring) from that of the lower QWs the measurement of photocurrent. This challenge is eliminated in SQW LEDs.

Another complication posed by commercial devices is the lateral non-uniformity in injection caused by less than ideal current spreading under the p-contact to the device. If a thick metal contact which covered the entire top of the mesa were used to achieve uniform current spreading, it would shadow nearly all of the light emission from the top of the device.

Therefore, a contact which covers only part of the mesa is used in commercial devices, and a transparent conducting oxide film like indium tin oxide (ITO) is inserted between the p-GaN and the contact metal to spread the current laterally over the entire mesa before it is injected into the active region. However, ITO is still absorbing enough that there is a practical tradeoff between the sheet resistance of the current spreading layer and the light extraction efficiency of the device. For practical thickness of ITO there can be still quite a bit of non-uniformity in the current spreading.

Typical commercial devices do not, therefore, have uniform current spreading, and the resulting non-uniformity complicates the interpretation of forward biased photocurrent measurements. The regions with higher current density would produce a different photo-response than the regions with lower current density and the measured photocurrent becomes the weighted average over the whole mesa. Additionally, the opaque metal contact shadows some of the optical excitation, so the optically injected area of the mesa does not overlap with the electrically injected area.

The solution to this is to use a semi-transparent metal p-contact which covers as much of the mesa area as possible, as discussed in the previous chapter. The optically and electrically injected areas of the device overlap highly in this design, and nearly all of the current spreading occurs within the metal contact. Only ~20 nm of Au is necessary to spread the current to a high degree of uniformity across a 0.1 mm^2 circular mesa from the perimeter. Counting the very thin contact metal (5 nm of Pt for the LEDs in this dissertation) this produces a semi-transparent contact with approximately 70% absorption. Clearly, this is not a good choice for commercial applications where light extraction efficiency is important, but it allows a far simpler interpretation of forward biased photocurrent measurements on the LEDs.

Finally, the choice to compare the photocurrent in devices with and without electron blocking layers (EBLs) was made as a simple way to potentially rule out current due to hot carriers generated by Auger recombination as a source of the measured photocurrent. AlGaN EBLs may or may not be effective at blocking low energy electrons from leaving the active region of the device towards the p-side of the device [23]. However, if they are and a significant reduction in the photocurrent were observed in LEDs with an EBL over those without, then current due to the Auger-generated hot carriers, which should have ample energy to surmount the EBL could not be the origin of the observed photocurrent. Absence of a significant reduction in photocurrent does not prove that Auger recombination was the mechanism behind the photocurrent however, due to the uncertainty over the blocking efficiency of the AlGaN layer.

4.2 Epi Design

A schematic of the epi structure of the SQW LEDs in this chapter is shown in Figure 4.2.1. Flat sapphire substrates were used instead of the more typical patterned sapphire substrates (PSS) to avoid unnecessary scattering of the pump light at the sapphire/GaN interface. Choosing flat sapphire comes with reduced light extraction efficiency, but this is less important for a proof of concept test of the measurement technique than reducing reflections of the pump light. And, the semi-transparent p-contact is already absorbing a significant fraction of the emission anyway, so light extraction was always going to be low in these LEDs.

Mg:p++-GaN contact layer
200 nm Mg:p-GaN
7 nm UID GaN
3 nm UID In _{0.15} Ga _{0.85} N
7 nm UID GaN
43 nm Si:n-GaN
6x Si:n-In _{0.04} Ga _{0.96} N (3 nm)/Si:n-GaN (8 nm)
1.1 μm Si:n-GaN
Buffer
Flat Sapphire Substrate

Figure 4.2.1: The epi structure of the SQW LEDs discussed in this chapter. The red layers are doped p-type, the blue layers are doped n-type, and the turquoise layer is the quantum well. In the LED with the EBL, the first 8 nm of the Mg:p-GaN layer was replaced with a Mg:AlGa_{0.15}N EBL layer.

The first layer grown was the GaN buffer layer, followed by a 1.1 μm thick Si-doped n-GaN layer. In the processed devices, this n-GaN layer is the one to which the n-contact is made. After the n-GaN layer, a Si-doped InGa_{0.04}N/GaN superlattice (SL) was grown, as is typical. The SL had 6 periods, the InGa_{0.04}N wells had a nominal 4% In content and were 3 nm thick, while the GaN barriers were 8 nm thick. The entire SL was doped to the same nominal Si concentration as the underlying n-GaN layer. After the SL, another 43 nm of Si-doped n-GaN was grown, at the same Si concentration.

Following the n-GaN layers, a 7 nm barrier of unintentionally doped (UID) GaN was grown, followed by the UID InGa_{0.15}N quantum well (QW) and another 7 nm UID GaN barrier. The QW had nominally 15% In content, and — more importantly — produced devices which emitted in EL at 450 nm +/- 5 nm over the entire range of current densities up to 100 A/cm².

After the UID active region layers, 200 nm of Mg-doped p-GaN was grown, followed by a relatively heavily Mg-doped p+ GaN contact layer. Two wafers were grown, on the same

day. In one of the wafers, an AlGaIn EBL was substituted for the first 8 nm of the 200 nm p-GaN layer.

An 11 mm x 11 mm piece was processed from each epi wafer, with the process described in Appendix A.

4.3 Results

4.3.1 DC Characteristics

Figure 4.3.1 shows the dark current-voltage (IV) for two representative SQW LEDs, one with and one without an EBL. Additionally, the light emission-current (LI) curves and a plot of the normalized, relative external quantum efficiency (EQE) versus current density for the same LEDs is shown in Figure 4.3.2.

It is clear from Figure 4.3.2(b) that both devices exhibit a similar degree of efficiency droop, and that the onset of droop in each device occurs at a nearly identical current density. This is an indication that they both have QWs of similar material quality. Poor quality material typically causes the current density at which the EQE peaks to increase, due to elevated Shockley-Read-Hall (SRH) recombination at low current densities. Higher quality material would similarly exhibit an EQE peaking at lower current densities, as the lower SRH recombination is more easily overcome by radiative recombination. This can be seen easily from the ABC model of droop. The carrier density at which the efficiency in the ABC model peaks, n^* , can be found by setting the derivative of the radiative efficiency equal to zero and solving for n^* ,

$$\left. \frac{\partial \eta_{rad}}{\partial n} \right|_{n=n^*} = \frac{2Bn \cdot (An + Bn^2 + Cn^3) - Bn^2 \cdot (A + 2Bn + 3Cn^2)}{(An + Bn^2 + Cn^3)^2} \Big|_{n=n^*} = 0$$

$$\Rightarrow 2Bn^* \cdot (An^* + Bn^{*2} + Cn^{*3}) - Bn^{*2} \cdot (A + 2Bn^* + 3Cn^{*2}) = 0$$

$$2An^* + 2Bn^{*2} + 2Cn^{*3} = An^* + 2Bn^{*2} + 3Cn^{*3}$$

$$An^* = Cn^{*3}$$

$$n^* = \sqrt{\frac{A}{C}} \quad (4.3.1)$$

It increases with increasing A coefficient (representing SRH) and decrease with increasing C coefficient (representing Auger recombination). The recombination current density is monotonic and increasing with the carrier density, and is given by

$$J = qd_{QW}(An + Bn^2 + Cn^3) \quad (4.3.2)$$

in the ABC model, so the current density at peak efficiency follows the carrier density at peak efficiency,

$$J^* = qd_{QW} An^* \left(2 + \frac{B}{\sqrt{AC}} \right) \quad (4.3.3)$$

From the semi-logarithmic IV curves Figure 4.3.1(b) it can be seen that neither device exhibits substantial leakage current in forward bias. Leakage current – current which bypasses the active region of the device via some parallel conduction path – can be caused by growth defects in the epi material, or by processing defects. Evidently neither are significantly present in this case and it is reasonable to assume that all of the current supplied to the device terminals travels through the active region of the device.

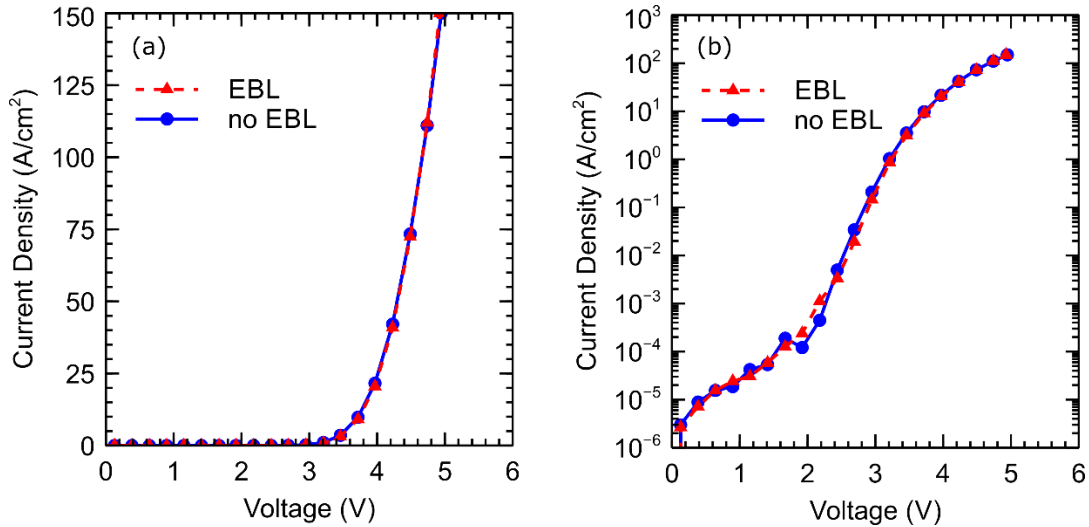


Figure 4.3.1: Unilluminated current density vs voltage data for representative SQW LEDs, both without an EBL (blue circles, solid lines) and with an EBL (red triangles, dashed lines). The only difference between (a) and (b) is the linear (a) or logarithmic (b) ordinate axis. Both plots show negligible leakage current below turn-on, though there is a high turn-on voltage of ~ 4 V at 20 A/cm², due to the unintentionally rectifying contacts.

Both devices exhibit a high forward voltage of nearly 4 V (at 20 A/cm²), which is due in large part to partially rectifying contacts. This rectification is unintentional, and a rectifying n-contact will have no effect on the photocurrent measurement since the contact is opaque and no hot carriers are generated in the metal within a mean free path of the metal-semiconductor interface (the importance of this is discussed in Chapter 2). Absorption in a rectifying p-contact metal on the other hand should be expected to have a small effect on the measurement if it is rectifying, as it is semi-transparent, thin, and it covers the entire mesa. The effect of the rectifying p-contacts to these SQW LEDs is discussed at the end of this chapter and is expected to be a small contribution to the overall photocurrent based on the observed photo-responses in other devices, including ones with improved p⁺ GaN contact layer doping.

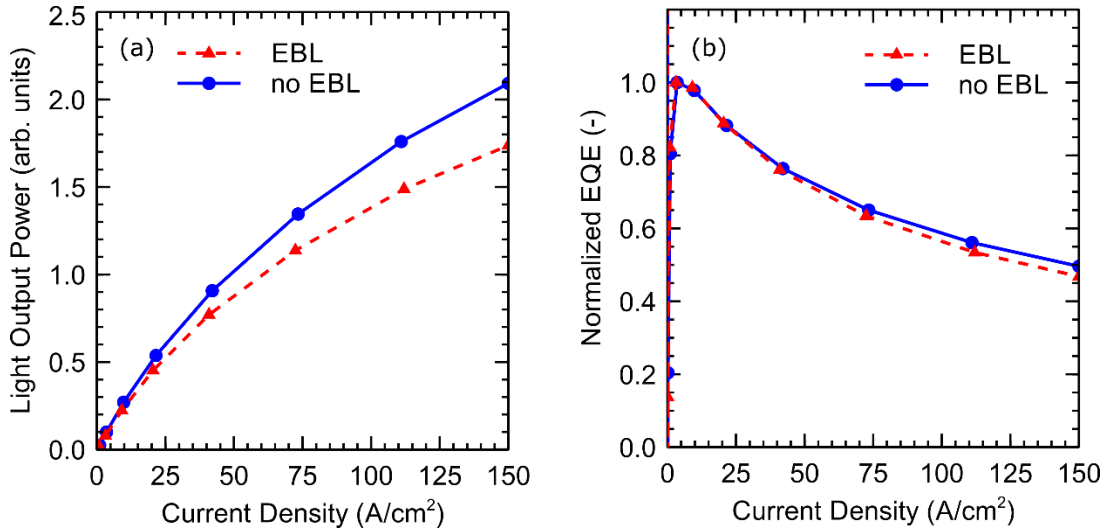


Figure 4.3.2: Unilluminated light output power (a) and normalized external quantum efficiency vs current density (b) for the same LEDs as in Figure 4.3.1.

4.3.2 Photo-Induced Modulation of the IV Characteristic

Measurements of the photoresponse of the LEDs were performed under two control schemes – 1) constant voltage, and 2) constant current. Under constant voltage conditions, the photo-modulation of the IV characteristic is observable as a change in the current, ΔJ , flowing through the device (Figure 4.3.3(a)). Under constant current conditions, the photoresponse is a change in voltage, ΔV , across the device (Figure 4.3.3(b)). If $\Delta J > 0$, this necessarily implies $\Delta V < 0$, as can be seen from the schematic IV curves in Figure 2.7.4. Therefore, making measurements under both control schemes provides a consistency check for the experiments – if ΔJ and ΔV had the same sign it would mean something is wrong with the measurement. This is not the case and the two control schemes are consistent.

Another important practical difference between the two schemes comes down to the effect of the Ohmic voltage drop across the series resistance of the device, which can be considerable under the high current density conditions in the droop regime. As an example, if the series

resistance is 5Ω , then 100 A/cm^2 in a 0.1 mm^2 device (100 mA) corresponds to a 0.5 V drop. When the terminal voltage is held constant and the current is allowed to change, the Ohmic voltage drop ($I \cdot R$) changes with the current, and so the "junction voltage" of the diode changes as well. The junction voltage is the voltage across the contacts that isn't dropped across the series resistance of the device and is the voltage which determines the current through the diode. The series resistance of the device is mostly due to the p-contact and current spreading (either in the p-side current spreading layer, or in the n-GaN as current spreads laterally under the mesa). Therefore, the junction voltage represents, to a good approximation, the voltage dropped across the depletion region of the pn-junction. Ideally, this is the voltage we would like to hold constant, as it is what controls the conductance of the LED. However, this is impossible and we only have control over the voltage difference between the contacts of the device. Measuring the photoresponse of the LED at constant current avoids this issue as the Ohmic voltage drop does not change when the current is held constant. Therefore, the change in voltage measured under optical excitation is a change in the junction voltage alone.

Measurements of the photocurrent at constant voltage are still useful when the overall modulation of the IV characteristic is small however, as the change in the junction voltage is consequently also small. Additionally, checking the consistency of the constant current and constant voltage measurements by multiplying ΔV at constant current by the slope of the IV characteristic measured in the dark to calculate the expected photocurrent, and comparing that to the measured ΔJ at constant voltage. The result of this calculation is shown in Figure 4.3.4. While low, the noise in the dark IV characteristic is similar in magnitude to the photomodulation, so using the slope of the IV characteristic to convert constant current measurements of the photovoltage to photocurrents is not ideal and produces a very noisy

comparison. Nonetheless, to the extent that a comparison can be made, the two control schemes appear to be consistent.

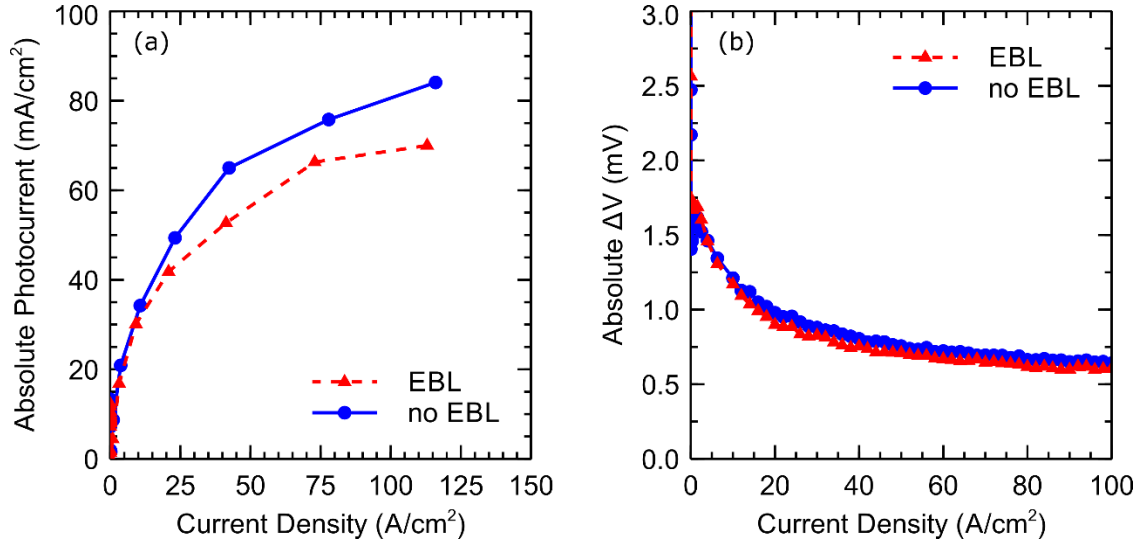


Figure 4.3.3: Data from the forward-biased photomodulation measurements, at a pump power density of ~ 5.7 W/cm², on the SQW LEDs. The photocurrent measured at constant voltage is shown in (a), plotted vs the forward current density through the LED. The photovoltage measured at constant current is shown in (b), plotted vs the forward current density through the LED.

The reverse bias photocurrent was measured at -1 V, originally with the intention of using it as a measure of the optical generation rate of carriers into the QW. However, it was only ~ 17 mA/cm², which is ~ 3 x less than the photocurrent in forward bias. If there were 100% sweep out efficiency of optically excited electron-hole pairs from the QW in reverse bias, this would imply that the source of the photocurrent was somehow producing current at ~ 3 x times the rate that carriers were being photo-generated into the QW. Fortunately, the assumption that there is 100% sweep out efficiency in reverse bias is a poor one for these LEDs. For tunneling escape to be efficient in InGaN QWs where the carriers face barriers to thermionic emission of several hundred millivolts, the depletion regions *and* the UID barriers on either side of the QW must have sufficiently high electric fields so that the tunneling barrier is ~ 3 nm

wide. Since the UID barriers are 7 nm wide, this requires high reverse biases – above where these narrow junction devices begin to experience breakdown. If instead the sweep out efficiency were closer to 33% (very reasonable), the forward photocurrent would be consistent with the reverse bias photocurrent.

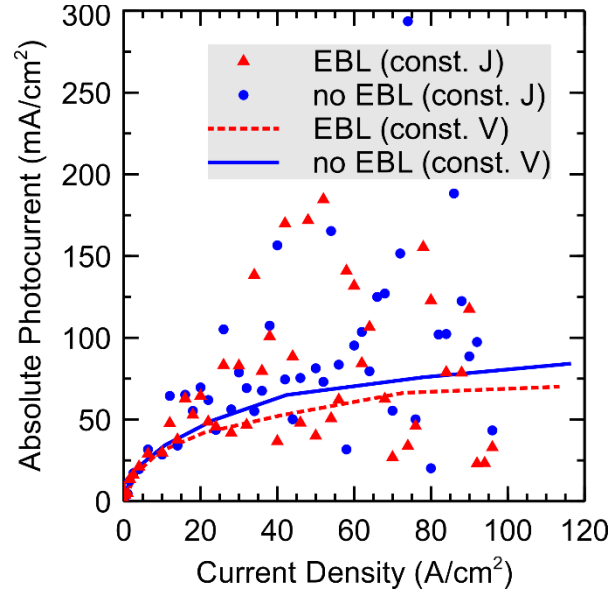


Figure 4.3.4: Comparison of the photocurrent measured at constant voltage (lines) and the photocurrent calculated from the photovoltage measured at constant current and the slope of the dark IV characteristic (symbols). The data calculated from the measured photovoltage are considerably more noisy than the data measured at constant voltage (same as shown in Figure 4.3.3(a)).

Finally, as discussed in Chapter 3, the lock-in amplifier output signal represents the absolute value root-mean-square (rms) amplitude of the first harmonic of the square wave photomodulation of the LED’s IV characteristic. This signal must be multiplied by a factor of $\pi/\sqrt{2}$ to convert it to the full peak-to-peak amplitude of the square wave photoresponse of the LED. Absent from the lock-in output signal (in amplitude-phase mode) is any information on the sign of the photoresponse. Normally, this information could be retrieved from the phase angle of the input signal to the reference signal (it should shift by 180 degrees when the sign

flips, in amplitude-phase mode), or from the sign of the in-phase component (X, in X-Y mode). However, there is considerable noise in the phase signal at the low LED biases where the sign flips and the shift is mysteriously ~ 160 degrees instead of 180 degrees (in X-Y mode, this means that when the sign of X flips, the out-of-phase component, Y, becomes non-zero). This puzzling behavior persists when different lock-in amplifiers are used, so it is almost certainly a real effect and not a problem with the instrumentation. Therefore, instead of relying on the lock-in alone, the change in sign of the LED photoresponse was confirmed by hand by comparing the change in current at reverse and forward biases. The photoresponse, though small, can still be detected at high enough forward biases and pump intensities using a high precision digital multimeter. The photoresponse shown in Figure 4.3.3 was checked in this way and was found to be of the opposite sign to the photoresponse in reverse bias. This is crucial, as it confirms that the photocurrent in the forward biased LEDs is in the forward direction. Additionally, the magnitude of the lock-in amplitude signal was checked against measurements done by hand to confirm that it measured the same values, which it did.

4.3.3 Photo-Induced Modulation of the EL Intensity

In addition to the photoresponse of the IV characteristics of the LEDs, the change in the EL intensity was measured. This is shown in Figure 4.3.5(a), and is shown normalized to the EL intensity measured in the dark in Figure 4.3.5(b), plotted against the current density through the device. The sign of the change in EL can be seen not to vary with current density (there is no cusp in the lock-in output signal). DC measurements using a high precision digital multimeter showed that the EL intensity increased with photo-excitation.

Increasing EL intensity corresponds, necessarily, to an increased radiative recombination rate within the QW of the LEDs. This, in turn, implies that the carrier densities within the QW are increasing with photo-excitation. It is not easy to see that this necessarily had to be the case, but it will prove useful to know that it is.

For instance, since the carrier density in the QW increases under resonant optical excitation, that implies that all of the non-radiative recombination rates which depend on the carrier density also increase. This includes the Auger recombination rates (both *eeh* and *ehh*), and therefore the hot carrier generation rates.

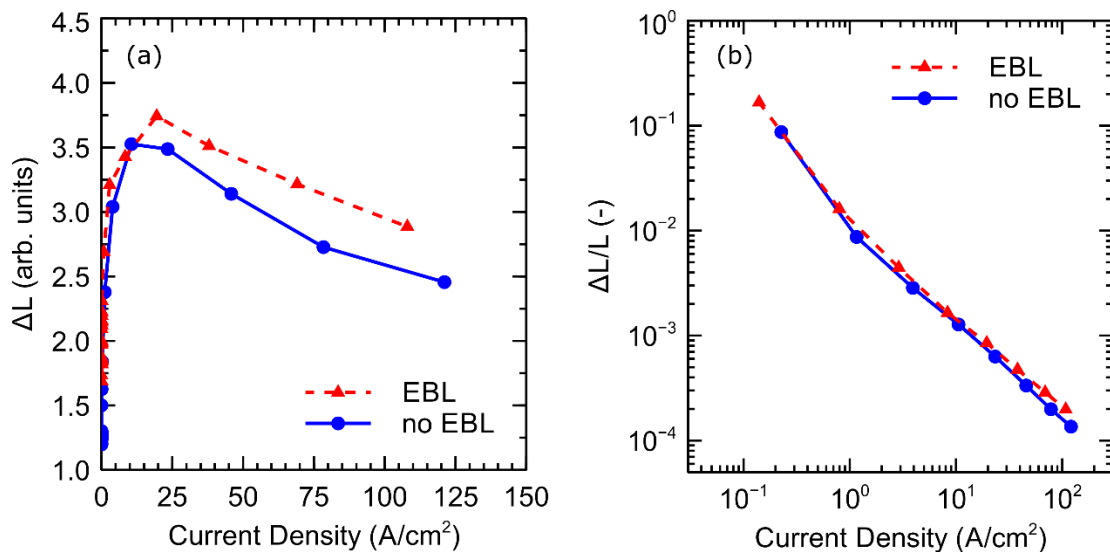


Figure 4.3.5: Photomodulated change in EL intensity, ΔL , measured at constant voltage, at a pump power density of $\sim 5.7 W/cm^2$, (a) and the normalized change in EL intensity (b), plotted vs current density. The EL intensity increased under illumination.

The normalized increase in the EL intensity diminishes with increasing current density, consistent with the picture of a decreasing carrier lifetime within the QW. As discussed in the introduction to this chapter, at a constant generation rate (optical excitation power), shorter total carrier lifetime corresponds to fewer added carrier density.

It is also interesting to note that the increase in EL intensity shown in Figure 4.3.5(a) appears to have a shape similar to that of an EQE plot with droop.

4.4 Discussion

4.4.1 Potential Sources of Forward Photocurrent

For resonant optical photo-excitation of the QW(s) in a QW pn-junction device (like an LED) to generate photocurrent, the carriers generated by the excitation must somehow escape the QW and make it to the contacts.

SRH or radiative recombination of photo-excited carriers cannot generate any photocurrent in a resonantly photo-excited QW LED because the recombining carriers never leave the QW. The same is not true of Auger recombination, which will be discussed below.

In reverse biased QW pn-junction devices, carriers may escape the QW by either tunneling out of the QW or by thermionic emission. Tunneling escape is always in the reverse direction, because there are no states to tunnel into in the forward direction in a pn-junction. Thermionic emission is favored producing a net reverse current due to the larger potential barrier in the forward direction. These two processes are shown schematically in Figure 4.4.1.

In forward biased QW pn-junction devices, these escape mechanisms also function when the forward bias is below the flat band voltage, which is usually equal to the built-in voltage of the junction. As the forward bias approaches the flat band voltage, the efficiency of tunneling out of the QW decreases as the electric field in the junction decreases and the potential barrier widens. Additionally, as the electric field in the junction vanishes so does the potential difference between the two sides of the junction. This means that thermionic

emission of carriers out of the QW(s) tends towards producing zero net current as the barriers to escape on either side of the junction become identical, at the flat band voltage.

When the forward bias on the diode, V_{applied} , is below the open circuit voltage, V_{OC} , of the device ($V_{\text{applied}} < V_{\text{OC}}$, and as a reminder, V_{OC} corresponds to the diode bias where zero net current flows under a given optical power density), the photocurrent is still in reverse (due to tunneling and thermionic emission), even though there is a small dark current (only a few mA/cm^2) in the forward direction. This dark current corresponds to a mix of SRH, radiative, and Auger recombination of carriers. At such low carrier densities as occur in the QW(s) below V_{OC} , SRH should be the dominant recombination mechanism.

When the forward biased dark current through a QW pn-junction device is large enough (several A/cm^2 , orders of magnitude larger than in unconcentrated solar cells) that appreciable Auger recombination occurs in the QW layer(s), an additional escape mechanism must be considered – escape of the hot carriers generated by Auger recombination. These hot carriers have energies of several eV (in III-Nitride devices) once they leave the QW layers for the GaN barriers. This is quite a lot of energy and is easily enough for carriers to overcome the junction field in forward bias. The final states for hot carriers generated by Auger processes in a QW are thought to be high- \vec{k} states, with directionally uniform distribution of momenta [50]. This, together with the symmetric diffusional forces due to the absence of a thermal population of hot carriers, approximately 50% of the carriers can be expected to go in each direction.

Before continuing, there are two important points with respect to the net current due to Auger-generated hot carriers. First, this uncertainty in the hot carrier escape direction affects the electrically injected current in the dark differently than it does the photocurrent. This is discussed further in the next section. Secondly, neither tunneling escape nor thermionic

emission will ever produce net forward photocurrent, at any bias sufficiently below the built-in voltage of the diode. So, despite the difficulty in determining the direction of the theoretical hot carrier current, photocurrent due to Auger-generated hot carriers is the only escape mechanism which can produce photocurrent in the forward direction when the junction is biased below its flatband voltage.

4.4.2 Mass Balance Analysis for the Various Escape Mechanisms

To expand on the difference between the dark current produced by the various escape mechanisms and the photocurrent produced by those mechanisms, consider Figure 4.4.1, which depicts carrier escape from a SQW LED, with no EBL for simplicity.

The difference is in whether the carriers involved in the escape process have been injected from the electrical contacts in order to be in the QW (so they can then escape it), or if they have been generated directly into the QW by absorption of a photon. In the dark, all the carriers participating in every escape process have been injected from the electrical contacts, so the injection current must be added to the net current of the escaping carriers to arrive at the total current.

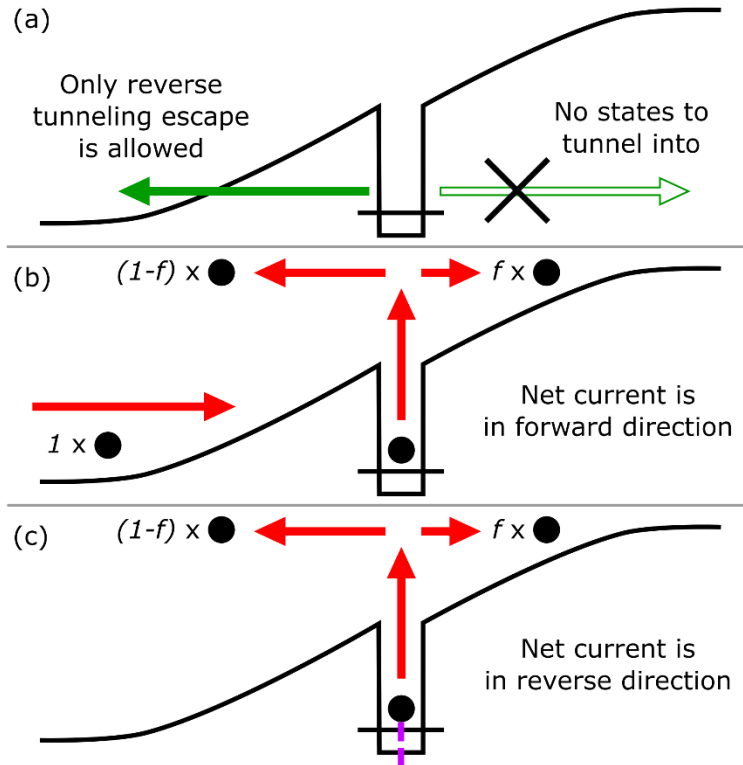


Figure 4.4.1: Carrier escape of electrically injected carriers by quantum mechanical tunneling (a) and thermionic emission (b). The fraction of carriers which goes in the forward direction is zero for tunneling and some value, f , greater than zero for thermionic emission. Depicted in (c) is the case of escape of photoexcited carriers by thermionic emission.

In the case of tunneling escape in the dark (Figure 4.4.1(a)), the net escape current is zero as tunneling is always in reverse and every escaping carrier has to travel to the QW from the contacts via forward current.

For thermionic emission in the dark (Figure 4.4.1(b)), some of the carriers may travel forward, though the majority will always escape in the reverse direction due to the lower potential barrier. As the forward bias increases, the fraction travelling forward approaches 50%. The net escape current then is proportional to the product of the total escape rate and the fraction of carriers escaping in the forward direction, tending towards half the total thermionic

emission rate at high forward biases. Carriers travelling in the reverse direction contribute no net current in the dark for the same reason there is no net dark current from tunneling escape.

The carriers travelling in the forward direction are injected from one contact as majority carriers, progress through the junction to the active region where they are subsequently trapped in the QW for a time. They then acquire enough thermal energy to be emitted and continue on their way through the circuit in the forward direction to the other contact as minority carriers. By the time they reach the opposite contact, the escaped carriers are indistinguishable from minority carriers which were never bound in the QW. As a result, the net forward thermionic emission current can never be greater than the total minority carrier diffusion current across the pn-junction. Even for GaN LEDs, which are short on the p-side, this can be expected to be small at reasonable output powers as the LEDs typically turn on at junction voltages several hundred mV below the built-in voltage of the junction. However, even if thermionic escape and the resulting minority carrier diffusion current were significant in GaN LEDs in the dark, it will be seen in a moment that there can be no forward photocurrent resulting from this escape mechanism.

The situation for Auger-generated hot carrier current is a bit more complicated than for either of the two cases discussed so far because Auger recombination is a three-body process. In the dark, all three carriers involved in the Auger event must be injected into the active region. Take the case of *eeh* Auger recombination as an example (*ehh* Auger is analogous and is discussed more thoroughly in Appendix C). In this case, two electrons and one hole must be injected into the active region. One electron recombines with the hole, producing one carrier worth of forward current per every Auger event. The other electron becomes hot and escapes the active region in one of two directions. If it travels in reverse, it produces no net escape

current on its own, just as for escape by tunneling or thermionic emission. The total current for the event is one carrier worth of forward current due to the recombination. If the hot carrier escapes in the forward direction, then it produces one additional carrier worth of current for that recombination event. The total current is now two carriers worth of forward current for the event. If the fraction of hot carriers which travel forward is called f , then it is straightforward to see that the total dark current due to Auger recombination events must be proportional to $1 + f$ times the Auger recombination rate. The case that f is exactly 50% is shown in Figure 4.4.2.

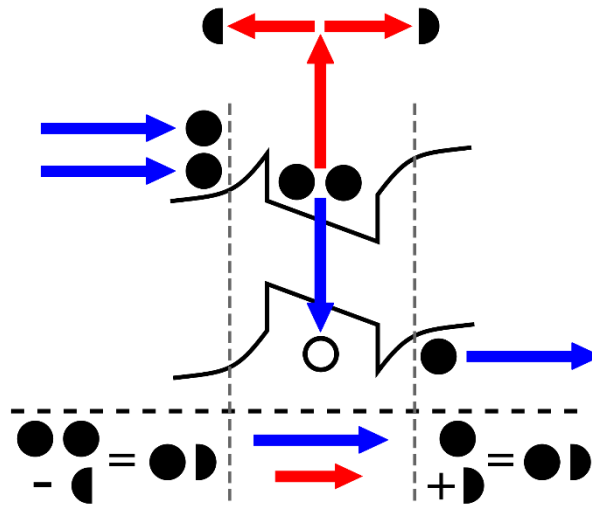


Figure 4.4.2: Schematic showing the situation for *eeh* Auger, where all the carriers are electrically injected into a SQW active region, and assuming exactly half of the hot carriers go in each direction after escaping the QW. Hemi-circles represent the fraction of carriers that are travelling in a given direction. Below the band diagram is shown the average carrier current for a single Auger event..

The above argument is due Witzigmann, et al. [60], [61], who considered the effect of the hot carrier current would have on measured values of the Auger rate coefficient, in the absence

of illumination. It should be noted that, while Witzigmann, et al. were the first to discuss the fate of the hot carriers escaping via the Auger process, the idea that the hot carriers contribute to leakage current in heterostructure junction devices originated in the InP-based laser literature [62]–[66].

Now, turning to the photocurrent resulting from each of these mechanisms, it is necessary to consider what happens when the escaping carriers have been excited directly into the QW. For tunneling escape, this means that a net reverse photocurrent now results as all the escaping carriers leave the QW in reverse – this is exactly the situation for photodetectors and solar cells. For thermionic emission, the photocurrent is proportional to the net escape current only, and so is $2f - 1$ times the photo-induced increase in the thermionic escape rate. If exactly 50% travel forward and 50% travel in reverse, there is no net photocurrent. For thermionic emission, $f < 50\%$ because of the larger potential barrier in the forward direction, so $2f - 1 < 0$ and the photocurrent is always in reverse. This is depicted in (Figure 4.4.1(c)). Neither escape by tunneling or by thermionic emission can therefore produce a forward photocurrent (when the voltage is below the flatband voltage for the junction) even if thermionic emission constitutes a large portion of the dark current flowing through the device in the droop regime as the proponents of the “carrier leakage” theory of droop contend.

Considering the photocurrent due to Auger-generated hot carriers is again complicated by the three-body nature of the Auger process. Optically modulating the Auger recombination rate (by increasing the bound carrier concentrations in the QW) causes an increase in the hot carrier generation rate. The expression for the Auger recombination rate under optical excitation can be expanded in a Taylor series. For perturbatively small excitations, only the term that is first order in the change in carrier density needs to be kept,

$$\mathcal{R}_{Auger} = C(n_{dark} + \Delta n)^3 \cong Cn_{dark}^3 + 3Cn_{dark}^2\Delta n, \quad \Delta n \ll n_{dark} \quad (4.4.1)$$

where n_{dark} is the carrier density in the dark, and Δn is the net increase in the carrier density upon illumination. If the carrier density increases, the net Auger recombination rate (i.e. – hot carrier production rate) also increases.

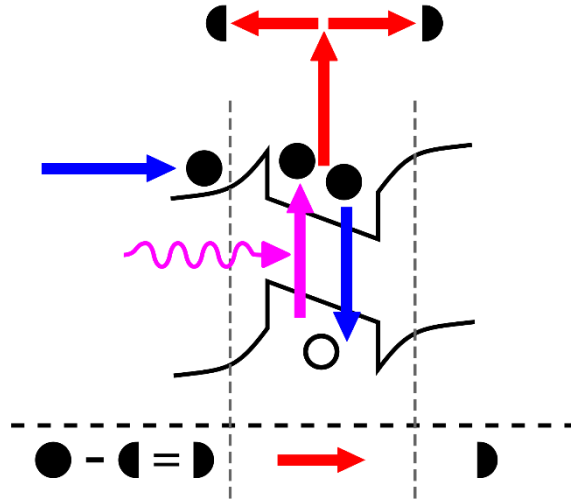


Figure 4.4.3: Schematic showing the situation for *eeh* Auger, where some but not all of the carriers are optically injected into a SQW active region. It is assuming that exactly half of the hot carriers go in each direction after escaping the QW. Hemi-circles represent the fraction of carriers which are travelling in a given direction. Below the band diagram is shown the average carrier current for a single Auger event. The current is still in the forward direction, unlike for thermionic emission.

There is no injection current associated with optically exciting carriers into the QWs so the photocurrent from the increased Auger recombination rate is entirely due to electrically injected hot carriers that are subsequently emitted from the QWs. Any hot carriers escaping in reverse produce a reverse current which cancels out the forward current that was required to inject them, and any hot carriers escaping in the forward direction produce an extra carrier worth of forward current. To a first approximation one might expect that exactly 50% of the

hot carriers escape in each direction, ignoring the junction field completely as a result of their high kinetic energy (the final states for Auger transitions out of semiconductor QWs are thought to be high energy with a high- \vec{k} , as discussed in Ref. [50]). This would result in 0.5 carriers worth of photocurrent, on average, per photo-excited Auger recombination event. This case is illustrated in Figure 4.4.3. Of course, higher order effects may make the actual fraction which escape in the forward direction different than 50%.

Escape of Auger-generated hot carriers is the only escape mechanism for photo-excited carriers that is capable of producing a net forward photocurrent. Since we know from EES measurements [7] that there is definitely Auger recombination occurring in the droop regime of forward biased QW LEDs, Auger-generated hot carriers must be contributing to the observed forward photocurrent. The extent to which they account for the entire photocurrent measured in the particular SQW LEDs discussed in this chapter is uncertain though, due to the unintentionally rectifying p-contacts which these devices had. This is discussed in the next section.

4.4.3 Possible Contact Effects

As mentioned above, the SQW LEDs discussed in this chapter had a slightly high turn-on voltage, likely due to rectifying contacts to p-GaN. If the contacts to the n-GaN were rectifying as well, they would have no effect on the photocurrent since they are opaque and completely off the mesa. As discussed in Chapter 2, p-contacts may generate a small forward photocurrent due to internal photoemission from the Schottky barrier at the contact, or from impact ionization if the p⁺⁺ contact layer is not heavily doped enough to form an Ohmic contact.

Based on past experience with the forward photocurrent in other devices, with commercial quality Ohmic contact layers and/or ITO contacts (where the absorption in the ITO near the semiconductor interface is much lower), the photocurrent in these SQW LEDs cannot be entirely due to contact effects. Additionally, the LEDs discussed in the next chapter all have Ohmic p-contacts, confirmed with circular transmission line measurements (CTLMs), and they exhibit forward photocurrent that scales with the number of QWs in the LEDs. The scaling with QW number could not occur if the photocurrent were entirely due to contact effects.

5 Photocurrent in MQW Blue LEDs

5.1 Introduction

The aim of the work presented in this chapter was to determine if it is possible to extend the analysis of the forward biased photocurrent measurements from single quantum well (SQW) light emitting diodes (LEDs) to multi-quantum well (MQW) structures, similar to those used in commercial devices. As discussed previously, the main question in extending the technique to MQW LEDs is how the non-uniform electrical injection of carriers into the multiple quantum wells (QWs) affects the measured photocurrent.

To study the effect of multiple QWs systematically a series of four custom LED structures were analyzed. All four were identical, except for the number of QWs in the structure – 1, 3, 5, and 7. Besides the number of QWs, the only significant difference between the LEDs discussed in this chapter and the ones from the last chapter is that the MQW LEDs also have improved contact layer doping so that the p-contact is Ohmic.

The chapter is organized as follows: first, the details of the epi structures will be discussed, and then the DC and photo-modulated data will be presented. Lastly, the dependence of the photocurrent and electroluminescence (EL) increase with QW number will be discussed.

5.2 Epi Design

The epi structure for the LEDs discussed in this chapter is shown in Figure 5.2.1. All of the epi was grown by Abdullah Alhassan. As with the SQW LEDs, all of the LEDs for the QW number series were grown on flat sapphire substrates to minimize scattering of the pump

light by the GaN/sapphire interface. The first layer grown was a 3 μm thick UID GaN buffer. After the buffer, 2 μm of Si-doped n-GaN was grown, where the Si concentration was nominally $5 \times 10^{18} \text{ cm}^{-3}$. Next, an n-type, 7-period superlattice was grown. The InGaN layers in the superlattice were 3 nm thick, while the GaN layers were 6.5 nm thick. The Si doping remained unchanged. Difference in the superlattice design between these LEDs and the superlattice in the SQW epi from the last chapter are not expected to impact the results in any way as the pump light is not absorbed in the superlattice.

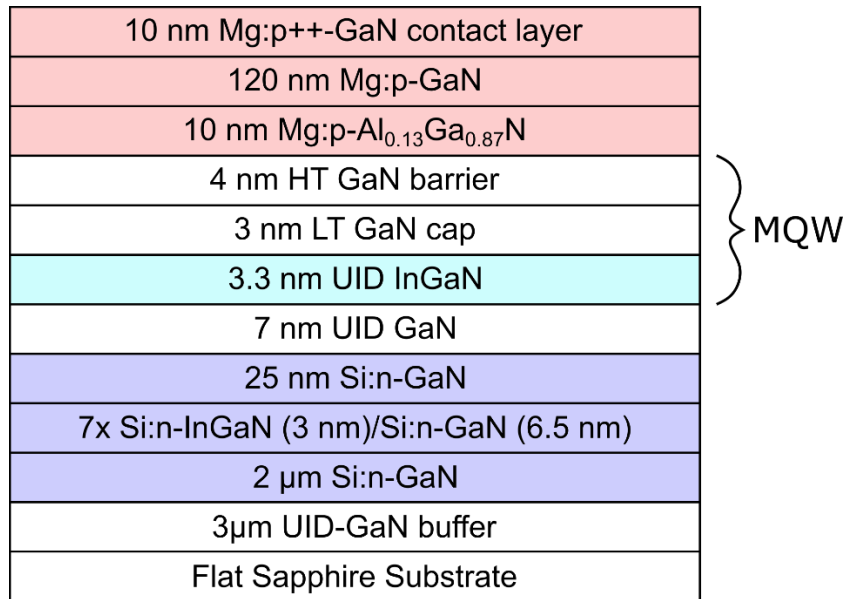


Figure 5.2.1: The epi structure of the MQW LEDs discussed in this chapter. The red layers are doped p-type, the blue layers are doped n-type, and the turquoise layer is the quantum well. Growth of the 3.3 nm QW layer, the 3 nm LT GaN cap, and the 4 nm HT GaN barrier (labelled 'MQW') was repeated a number of times equal to the number of QWs in each LED.

After the superlattice, a 25 nm thick n-GaN layer was grown, with nominally the same Si concentration as the previous n-type layers. The active region was grown next, beginning with a 7 nm thick UID GaN barrier. The following layers were repeated once for every QW in the device: a 3.3 nm thick InGaN QW, a 3 nm low temperature GaN barrier and a 4 nm high

temperature GaN barrier. The QW compositions were such that their emission wavelength under electrical excitation was again very nearly 450 nm for all the wafers grown.

After the final high temperature GaN barrier, a 10 nm thick, Mg-doped, p-type AlGaIn electron blocking layer (EBL) was grown, with nominally 13% Al content. Then, 120 nm of p-GaN was grown, with a nominal Mg concentration of $4.5 \times 10^{19} \text{ cm}^{-3}$. Finally, a 10 nm p++ GaN layer was grown to help provide Ohmic contacts. This layer was heavily doped with Mg, nominally $>1 \times 10^{20} \text{ cm}^{-3}$ in concentration to provide an improved contact layer for p-contact.

An 11 mm x 11 mm piece was processed from each epi wafer, with the process described in Appendix A.

5.3 Results

5.3.1 DC Characteristics

Shown below Figure 5.3.1 are the dark current-voltage (IV) characteristics of representative devices from each of the epi wafers. Current density is shown on a linear and a log scale. All of the devices measured were all chosen because of their low leakage current below turn-on. Additionally, the turn-on can be seen to be reasonably sharp for each of the LEDs tested. The forward voltage at 25 A/cm^2 is lower than for the SQW LEDs tested in the previous chapter – especially for the 1QW LED ($\sim 3.2 \text{ V}$ instead of $\sim 4.0 \text{ V}$ at 25 A/cm^2) – a sign that the contacts are improved. It is still a little high for all the LEDs, which is likely due to the un-annealed Ti/Au n-contacts, but rectifying n-contacts have no effect on the photocurrent of these devices due to the thickness of the metal, as discussed elsewhere.

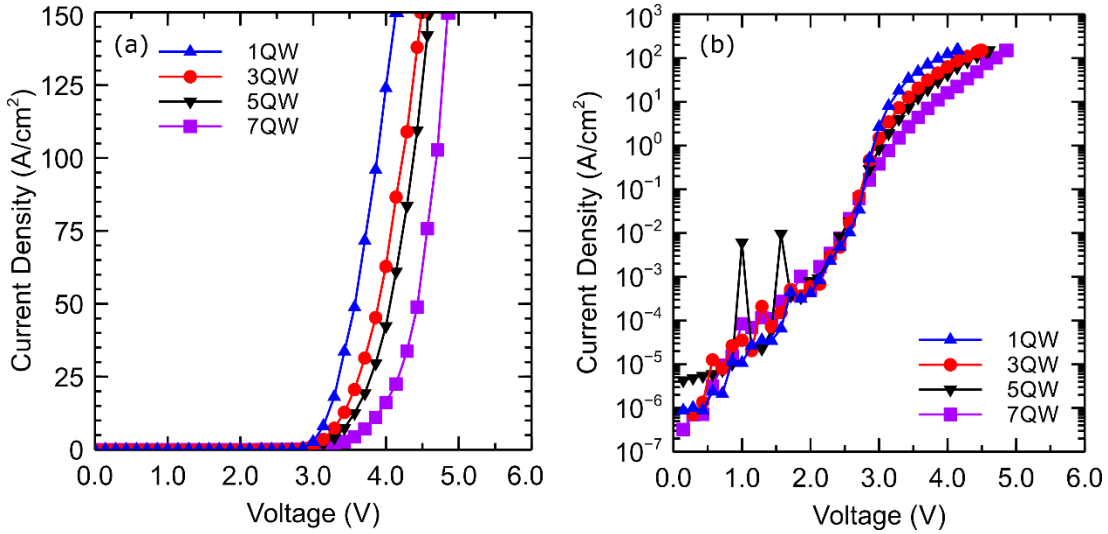


Figure 5.3.1: Unilluminated current density vs voltage characteristics plotted with a linear (a) and semi-logarithmic (b) ordinate axis scale, for the MQW devices discussed in this chapter.

To confirm that the semi-transparent Pt/Au p-contacts were rectifying, CTLM measurements were carried out on each epi piece that was processed. The IV curves are shown in Figure 5.3.2. The “correction factor method” was used to extract the contact resistance from the CTLM measurements, the details of which can be found in [67].

The contact resistances were all found to be on the order of $10^{-3} \Omega \cdot \text{cm}^2$, meaning that at 100 A/cm^2 the reverse biased Schottky junction at the contact is only dropping a few 100 mV. Since 403 nm pump light from the Coherent Cube laser has an energy of $\sim 3.06 \text{ eV/photon}$, the low contact resistance means that any hot holes generated in the metal which make it into the band-bending region will have a maximum energy of $\sim 3.16 \text{ eV}$ below the valence band maximum. The bandgap of GaN is 3.4 eV at room temperature (and $> 3.2 \text{ eV}$ for all temperatures $< 300 \text{ }^\circ\text{C}$ [68]) so the p-contacts to these devices will not contribute to the photocurrent as the hot holes will not have an energy in excess of the bandgap at the current densities used for the photocurrent measurements.

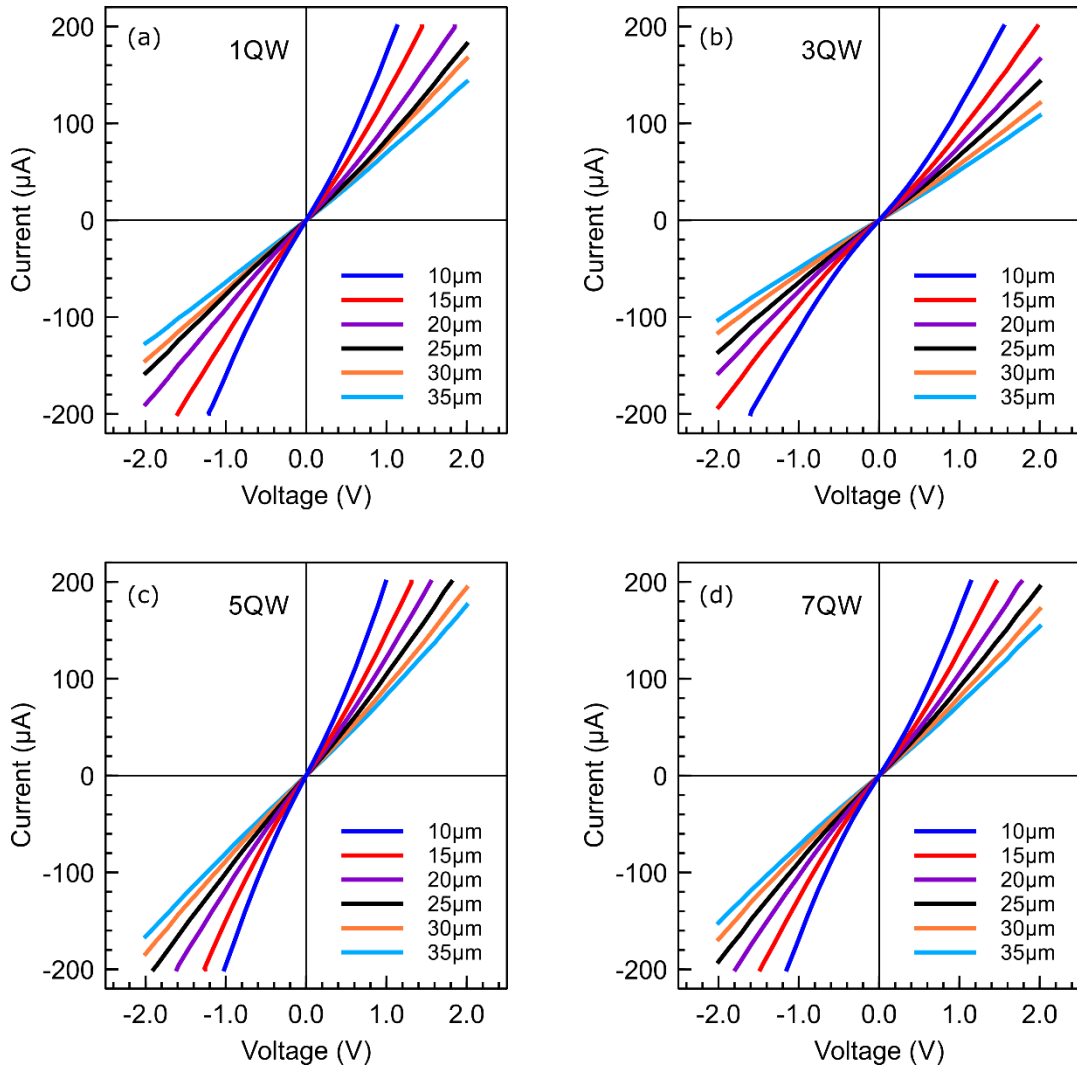


Figure 5.3.2: CTLM current-voltage characteristics for the p-contacts on the MQW epi pieces, for six different CTLM gap sizes (10, 15, 20, 25, 30, and 35 μm).

The normalized EQE curves for the MQW devices are shown in Figure 5.3.3. The current density is shown on a linear (Figure 5.3.3(a)) and a logarithmic (Figure 5.3.3(b)) scale. The efficiency of all of the devices appears to peak at approximately the same current density, and the extent of droop at higher current densities in each is similar.

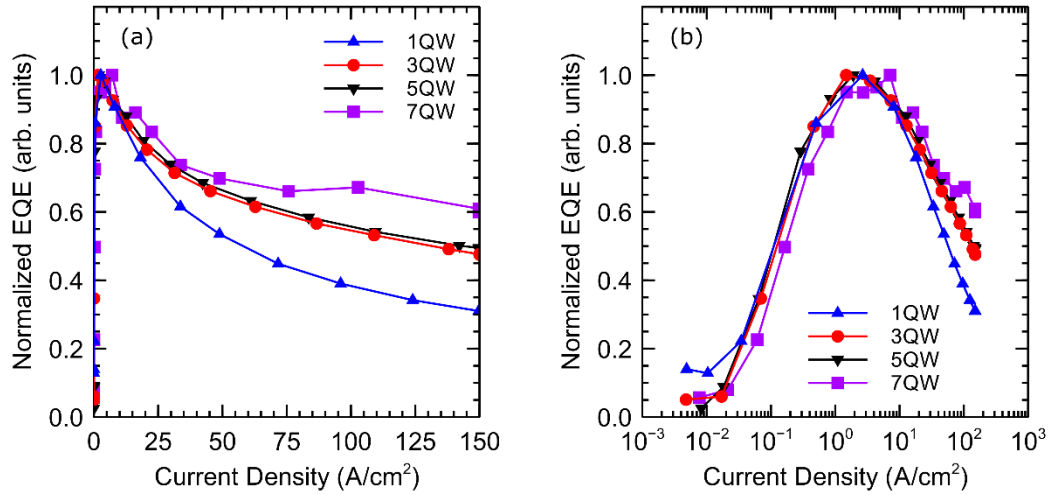


Figure 5.3.3: External quantum efficiency versus current density for the MQW LEDs, plotted with a linear (a) and semi-logarithmic (b) abscissa axis scale.

Since each additional QW adds to the total absorption of the pump light within the device, it would be useful to normalize the photocurrent in forward bias to the absorption. However, this is a difficult quantity to measure for such thin layers, since each QW only absorbs ~1-2% of the incident light. So, a proxy for the total absorption must be used instead.

The reverse bias photocurrent would be a useful stand-in if the sweep out efficiency of carriers were identical in each device. The escape rate of carriers from the QWs in reverse bias is limited by the generation rate when the sweep out efficiency is very high, and it would give a very good measure of the absorption in that case. Unfortunately the sweep out efficiency of these devices is not constant however, as can be seen in Figure 5.3.4.

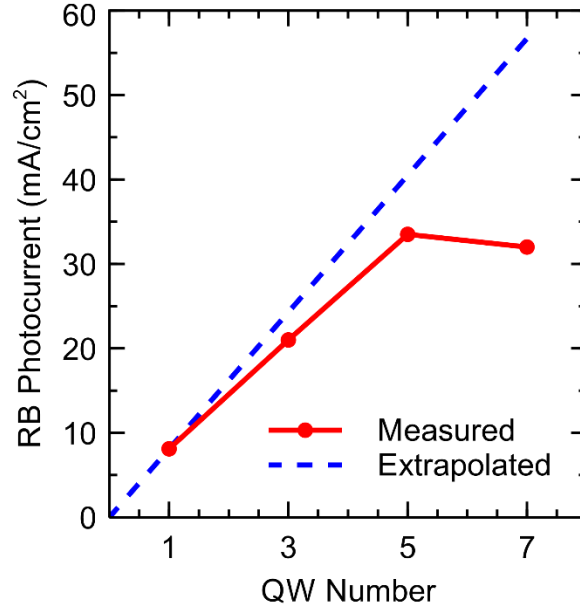


Figure 5.3.4: Measured reverse bias photocurrent (solid line with symbols) as a function of QW number, at a pump power density of $\sim 5.7 \text{ W/cm}^2$. Also shown is the expected reverse bias photocurrent (dashed line) if the sweep out efficiency were constant with QW number, extrapolated from the measured value in the 1QW LED.

If the sweep out efficiency didn't vary with QW number, then the photocurrent at -1 V in each device should follow the dashed line in Figure 5.3.4. Instead, the efficiency appears to decrease with increasing numbers of QWs. The ratio between the measured photocurrent at -1 V and the expected value assuming constant efficiency (equal to that for 1QW) is shown in Figure 5.3.5.

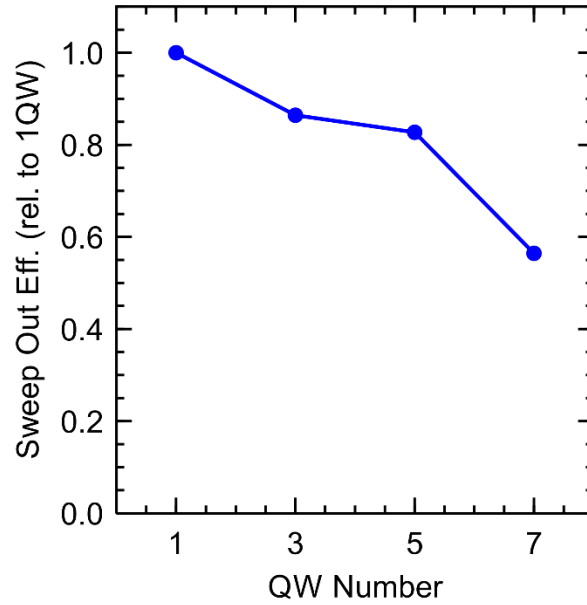


Figure 5.3.5: Ratio between the measured and expected reverse bias photocurrent (assuming the same efficiency as for one QW) as a function of QW number. This is proportional to the sweep out efficiency of the devices and is clearly not constant with QW number.

5.3.2 Modulation of the IV Characteristic and EL Intensity

Figure 5.3.6 shows the photocurrent in forward bias plotted versus current density for each of the LEDs measured. The lock-in provides only the absolute value of the photocurrent, but the sign is the same as in the previous chapter – in the forward direction, as confirmed with DC measurements, as for the LEDs in Chapter 4.

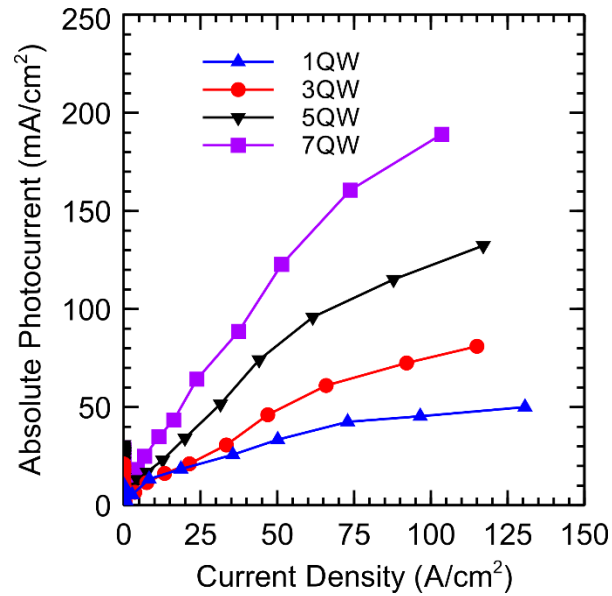


Figure 5.3.6: Constant voltage, forward-biased photocurrent measurements, at a pump power density of ~ 5.7 W/cm², for the MQW LEDs.

As can be readily seen in Figure 5.3.7, the forward biased photocurrent increases both with current density and with QW number. In Figure 5.3.8 the photocurrent normalized by QW number is shown. It is essentially constant for each additional QW after the first, but lower than for the first QW, indicating that the additional QWs do not add to the photocurrent in the same manner as the first QW does.

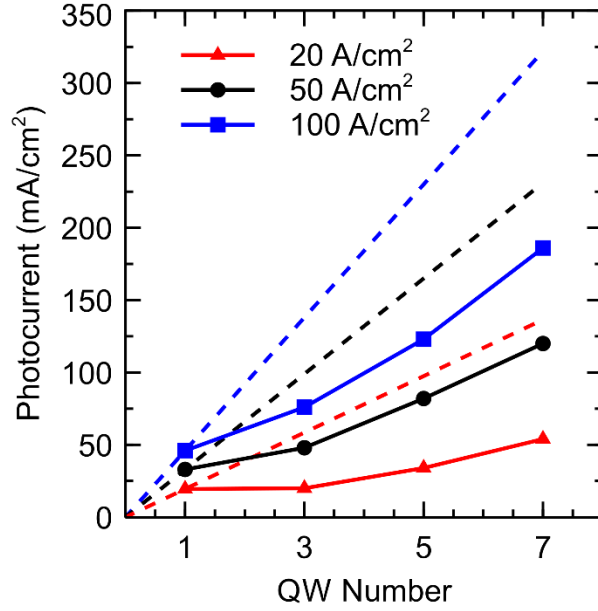


Figure 5.3.7: Forward biased photocurrent versus QW number, at three different current densities. The dashed lines denote what the photocurrent would be if it scaled with QW number, while the solid lines with symbols are the measured photocurrent.

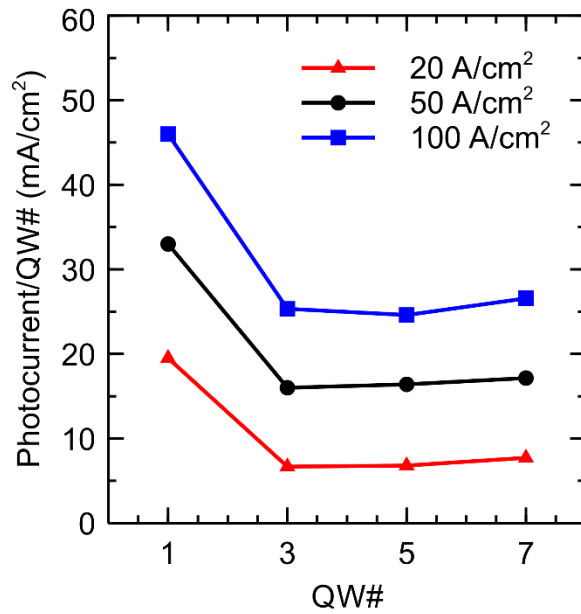


Figure 5.3.8: Forward biased photocurrent normalized by the QW number, plotted versus the QW number at three different current densities.

The EL intensity increase under illumination was also measured, and is shown in Figure 5.3.9. It was once again positive for all the LEDs, indicating that the carrier density in any of the QW(s) which were emitting light increased as well. As will be discussed below, the LI data imply that this is likely only the top QW.

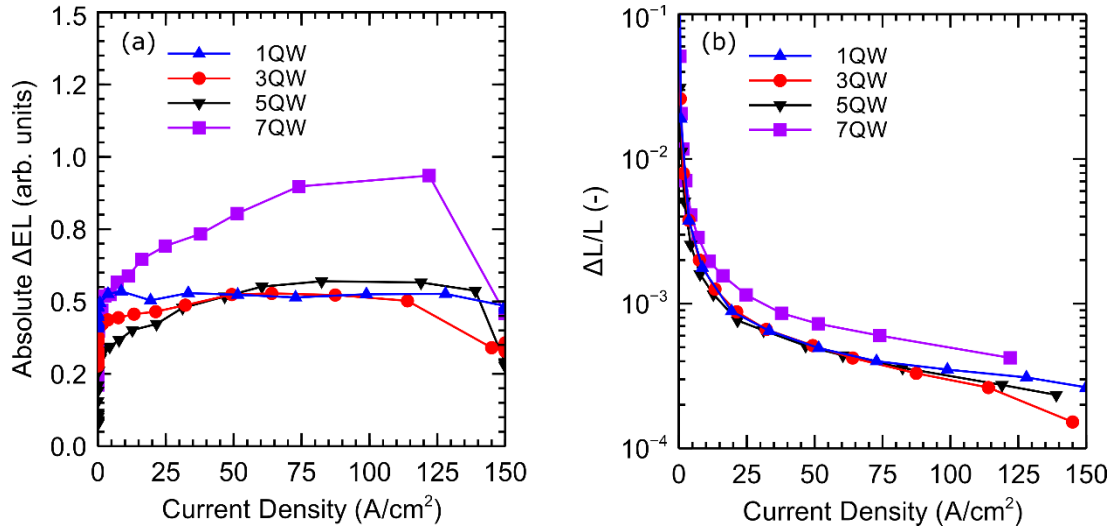


Figure 5.3.9: Photomodulated increase in EL intensity for the MQW LEDs, as measured (a) and normalized to the DC light output (b). There is little difference between the normalized curves with QW number.

5.3.3 LI data with PD mounted directly over samples

Because of the design of the photocurrent measurement apparatus, it is not easy to ensure that the magnitude of the measured EL signal can be compared between devices. The position of the device relative to the optical axis of the collection optics on the photodetector which measures the EL intensity is difficult to control precisely. In order to measure how much each additional QW adds to the light output of these LEDs, another setup was constructed specifically for this purpose.

A biased Si photodiode module with a built-in current amplifier was mounted on an x-y stage directly over a sample stage, as close as possible to the stage without interfering with the electrical probes. A Keithley 2400 series sourcemeter was used to forward bias the LEDs under current control and a handheld digital multimeter was used to measure the output of the photodetector. A schematic of the apparatus is shown in Figure 5.3.10.

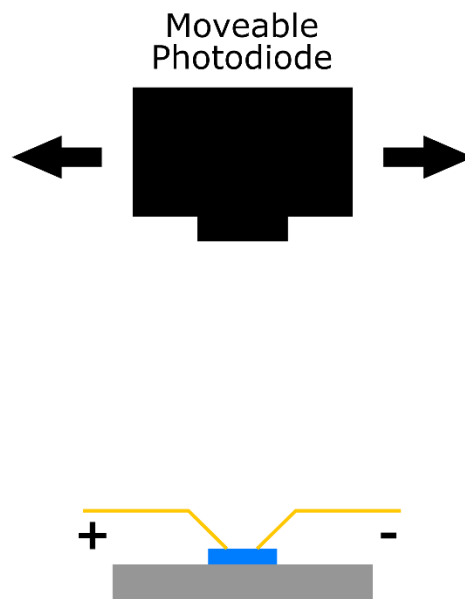


Figure 5.3.10: Schematic of the measurement setup used to collect light output power vs current density curves which could be compared between LEDs.

To make sure that the photodiode was directly over the device being measured, the position of the photodetector stage was adjusted for each LED, in order to maximize the signal while the device was forward biased before measuring the LI curve. The EL intensities are still not absolute values, as no integrating sphere was used, but the magnitudes can be compared between devices. The magnitude of the photodiode signal was recorded by hand and the data are plotted in Figure 5.3.11. As can be seen, there is no significant difference between devices

with different QW numbers, implying that the additional QWs do not contribute significantly to the overall light output of the LEDs.

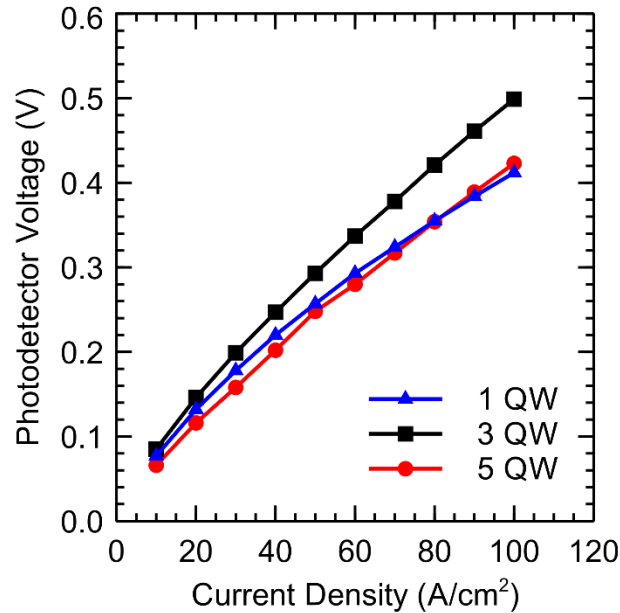


Figure 5.3.11: Light output power for three MQW LEDs plotted versus current density. The light output power for each LED was measured using the apparatus described in the text, so that the relative measurements for each device could be compared. There is negligible difference between the three LEDs.

5.4 Discussion

As mentioned in the introduction to this chapter, the purpose of studying the photocurrent in LEDs with variable numbers of QWs is to understand how to extend the analysis of the SQW LEDs in the previous chapter to more commercially relevant epi designs. Most commercial LEDs have multiple QWs. This is despite evidence in the literature that only the last-grown QW contributes significantly to the light output [22]. The LI characteristics of the

LEDs just presented are consistent with this observation as there is no significant difference in EL intensity between LEDs with different numbers of QWs.

The total light output of the LED is a sum of the light output of each QW. Assuming similar quality QWs (i.e. – similar SRH lifetimes), then it is in principle possible for a MQW LED to have the same total light output as a SQW device. All this would require is that the recombination current be redistributed between the QWs in a way that gives the same total output power, at the same current density. For this to occur though, the QWs in the MQW device would all have to be injected at lower carrier densities than the QW in the SQW device, otherwise the overall EL intensity would be greater. Since the QWs are all of similar quality, their individual radiative efficiencies would all peak at the same carrier density, and as this corresponds to a higher total current density (because of the additional recombination current in the other QWs), the EQE curve for the MQW device would necessarily peak at a higher current density than the SQW device. The progression of efficiency droop would also be stretched out in current density.

As the EQE curves essentially overlap for all of the LEDs studied in this chapter Figure 5.3.3, this clearly cannot be the case. Only two possibilities remain. Either only one QW is dominating the EL emission in each LED or the quality of the QWs is progressively improved (SRH lifetime is increased) as more QWs are added. If the quality of the QWs increases as more layers are grown, the peak in their individual radiative efficiencies would shift to lower carrier densities. For this to explain the overlapping EQE curves, the improvement in QW quality would have to occur by just the right amount to keep the peak EQE unchanged as QW number is increased, i.e. – for each of the 1QW, 3QW, 5QW, and 7QW devices. This would be a surprising coincidence indeed, so the only explanation for the LI data that remains is that

there is only one dominant QW contributing to the EL. Given that hole transport is more difficult than electron transport in GaN, due to the $\sim 5x$ higher effective mass, the dominant QW is almost certainly the top QW. It is nearest to the p-GaN, the source of injected holes.

It must be noted that state-of-the-art simulations of MQW LEDs [69] contradict this picture and show that even though there are considerably more injected carriers in the top QW than in the lower ones, there may be sufficient carrier densities in the lower QWs to put them into the droop regime where they would produce additional hot carriers via conventional Auger processes. So, it remains an open question as to how much the lower QWs are actually injected.

Assuming for the sake of argument that only one QW has a significant concentration of both electrons and holes, regardless of the number of QWs in the LED, and that the EL intensity from that one QW remains constant, then the Auger recombination current in each of the LEDs should be roughly constant with QW number as well. If the Auger recombination current is the same then the photocurrent due to Auger recombination in forward bias should remain constant. However, the photocurrent is observed to increase with QW number and this implies that additional QWs increase the net forward escape rate of carriers from the active region. Since carrier escape by tunneling can never produce forward photocurrent, there are only a few possible explanations:

- 1) There could be changes in the band structure of the active region as QW number increases which lower the forward barrier to thermionic emission out of the dominant top QW below the barrier to escape in the reverse direction.
- 2) The band structure could change so that the forward barrier to escape out of the lower QWs is lower than the barrier in the reverse as more QWs are added.

- 3) The optical excitation generates enough electron-hole pairs to induce Auger recombination in the lower QWs and the hot carriers that are thereby produced contribute to the forward photocurrent.
- 4) Hot carriers are produced in the lower QWs by a process other than the usual Auger recombination – one which occurs at lower carrier densities – but contribute to the forward photocurrent in the same manner as the hot carriers generated by normal Auger recombination.

Option 3 could potentially be ruled out on the basis of the LI data because it implies there isn't enough carrier generation to inject sufficient electron-hole pairs into the lower QWs to induce the usual kind of Auger recombination (remember, it has been assumed for the sake of argument that the picture presented in Ref. [69] is not correct – this assumption may be invalid). The pump intensity is only $\sim 6 \text{ W/cm}^2$ entering the semi-transparent p-contact, which is $\sim 70\%$ absorbing. The absorption of each QW can be estimated to be a few percent from the absorption coefficient of GaN above the band edge ($\sim 10^5 \text{ cm}^{-1}$). This makes the equivalent generation current in each QW only a few mA/cm^2 , and since EQE droop in a SQW LED typically doesn't begin until a few A/cm^2 (three orders of magnitude higher!), the possibility of photo-induced Auger recombination in the lower QWs can reasonably be ignored.

Band diagram simulations Figure 5.4.1 using the SiLENSe simulation software [70] show that at forward biases approaching the built-in voltage of the GaN diode, where there is forward photocurrent, the barrier to thermionic emission of electrons in the forward direction is still roughly identical to that in the reverse direction, for electrons escaping the dominant QW or any of the other QWs. For holes, the barrier to thermionic emission in the forward direction

appears to be slightly lower than in the reverse direction, but since holes have a ~ 5 x larger effective mass than electrons in nitrides the escape probability is considerably lower.

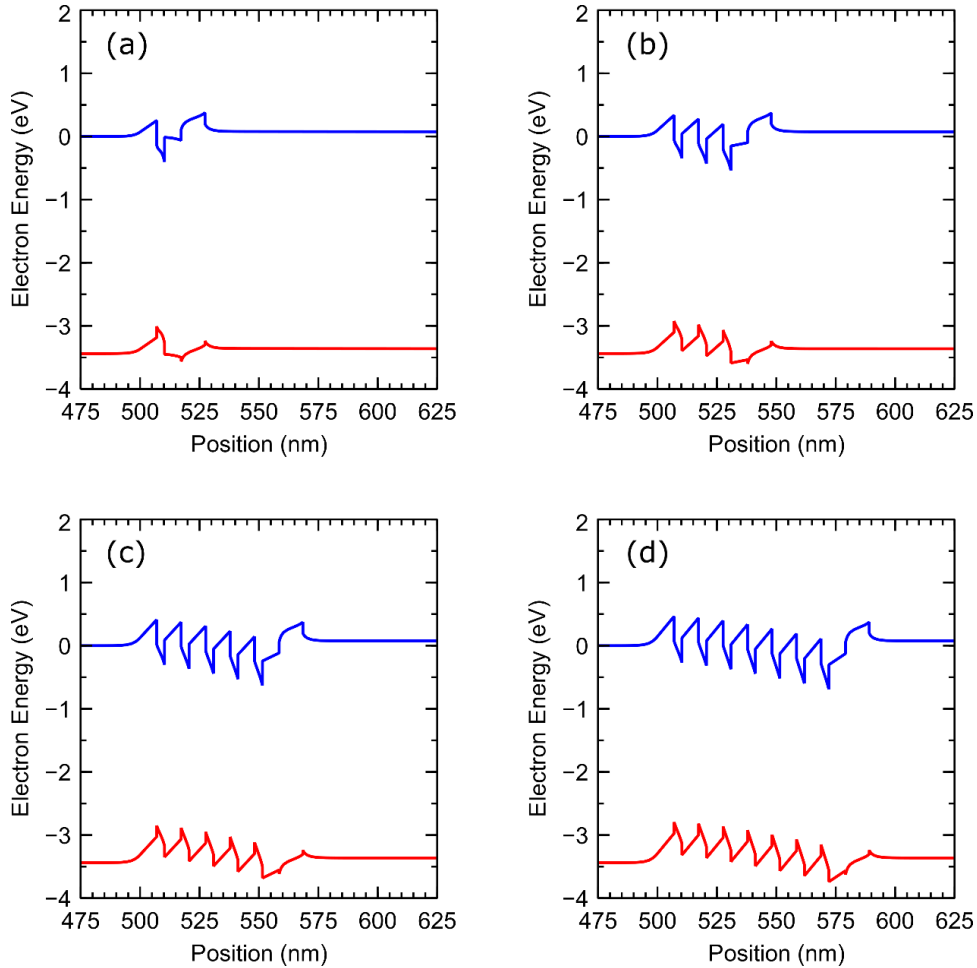


Figure 5.4.1: SiLENSe simulations of the band structure for the (a) 1QW, (b) 3QW, (c) 5QW, and (d) 7QW LED structures discussed in this chapter. The simulations were performed at a constant 3.25 V forward bias for all structures. The n-side of the junction is on the left in each plot. The conduction band is in blue and the valence band is in red.

There are limitations to computer simulations of QW LEDs, mostly stemming from the difficulty of accurately capturing the physics of carrier transport perpendicular to thin heterostructures, so LED simulation results should always be taken with heaping helping of salt. This is particularly true of these simulations, as the program predicts that each of the QWs

should have nearly identical electron and hole concentrations, which (as discussed above) cannot be the case in these LEDs. Even in the more sophisticated simulations in Ref. [69], the lower QWs have lower concentrations than the top QW. While the quasi-Fermi levels (carrier concentrations) are almost certainly inaccurate (and so are not shown in Figure 5.4.1), the calculated bands themselves can be reasonably well trusted since the effects of carrier transport on the bands are minor. They are mostly determined by the electrostatics of the space charge distribution in the device, which is controlled by the doping in the n- and p-regions, and by the polarization fields in the strained QWs. As it is the bands which provide insight into the thermal barriers to carrier escape, the simulations are adequate for our purpose in this chapter. Options 1 and 2 can both be ruled out as a result.

Only the fourth option is left, barring a carrier distribution in the QWs such as is discussed in Ref. [69]. Before considering what an alternate hot carrier generation mechanism might be in these lower QWs, it is important to note that after the first QW, the photocurrent increase due to each additional QW after the first is approximately the same (see Figure 5.3.8). This is suggestive of a hot carrier mechanism, since thermal carriers escaping QWs in the active region will feel different barrier heights to forward and reverse escape depending on the position of the QW they are escaping from within the active region, while hot carriers have enough energy to surmount all of the barriers regardless of their origin in the active region. This can be seen in the MQW LEDs Figure 5.4.1(b), (c), and (d).

The usual band-to-band Auger recombination is not the only type of Auger recombination that is possible in semiconductors. One or more of the steps in defect-assisted recombination may be an Auger process [31], [71]–[75]. An example of one such process is shown in Figure 5.4.2. Such a two-step defect-Augur process would have a lower order carrier density

dependence than band-to-band Auger recombination (which is third order, recall), and so could occur at a significant rate at the low carrier densities found in the lower QWs of a MQW LED. It would also increase at a slower pace than band-to-band Auger as more carriers were injected, which is what is observed. As shown in Figure 5.3.8, the ratio of the photocurrent in the SQW LED to the average photocurrent per QW in the MQW LEDs increases at higher current densities, implying that the photocurrent in the first QW is a bigger fraction of the total photocurrent when the QWs are injected more strongly.

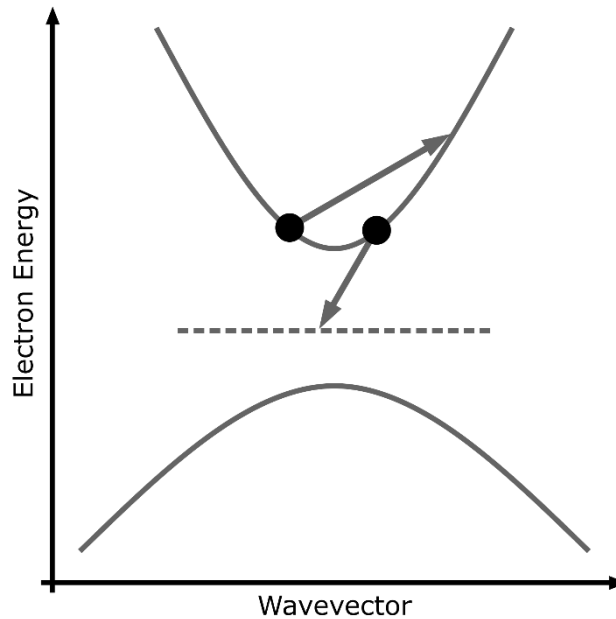


Figure 5.4.2: Schematic of one trap-assisted Auger process. Note that because a localized (i.e. – point) defect state is involved, crystal momentum is not conserved. The other varieties of trap-assisted Auger recombination are described in [31].

Defect-Auger processes would also have increased rates, relative to the usual SRH defect recombination and radiative recombination, when there is an asymmetric carrier population (e.g. - many more electrons than holes), as there likely is in the lower QWs of MQW LEDs.

An excess of electrons would favor processes involving more electrons than holes, such as an *eeh* Auger process.

Defect-assisted Auger recombination has not been confirmed to occur in any semiconductor to date, so of course a considerable amount of work remains to prove or disprove that such a process is actually occurring in MQW LEDs. It is entirely possible that some other explanation for the observed photocurrent in the MQW LEDs studied exists but has been overlooked in this chapter. To this end, preliminary studies of the photocurrent in SQW LEDs grown by ammonia molecular beam epitaxy (MBE) are presented in the next chapter. These LEDs do not droop, even out to 100 A/cm^2 , and have a low overall efficiency. As a result, they should not have any photocurrent in forward bias and they likely have many SRH centers in the QW, which kill the efficiency. Additional work is proposed, which may help get to the bottom of why the photocurrent in the MQW LEDs discussed in this chapter increases with additional QWs.

6 Ongoing and Future Work

6.1 Introduction

As with all research, there is more to do. The obvious next steps to build on the research presented in this dissertation are to:

- Continue extending the technique to commercial grade epi material and devices.
- Measure the photocurrent in SQW and MQW green LEDs.
- Further explore the origins of the photocurrent from the lower QWs in MQW LEDs.
- Compare results of photocurrent measurements to EES measurements on the same LEDs.

Each of these will be discussed in the following sections. In addition, a brief discussion of the application of the ABC model of efficiency to analyzing the photocurrent will be given, and the last section will also discuss preliminary work on understanding the origins of the photocurrent from the lower QWs.

6.2 Commercial Epi and Devices

Extending the technique to commercial MQW devices should be relatively straightforward. The main questions are, how many QWs are effectively injected in the state-of-the-art commercial MQW devices, and how does current crowding complicate the analysis. Determining how many QWs are effectively injected in state-of-the-art devices could be difficult if there is more than one dominant QW, but if there is only one then this may be

confirmed just as was done for the MQW devices studied in this chapter – by comparing the LI curve to a SQW device with an otherwise identical structure.

The main question regarding the effect of current crowding is whether or not there is significant lateral diffusion of photo-excited carriers. It should be relatively simple to check this in commercial devices. If there is no significant lateral diffusion, then the photocurrent in a device with current crowding is just an average of the photocurrent as a function of current density, weighted by the lateral current density profile in the photo-excited area of the device. The current density profile can be obtained from 3D modeling of the device structure, combined with imaging of the light emission intensity across the device. The photocurrent as a function of current density can be obtained by processing a reference device from the same epi into a structure with near ideal current spreading (as used in this dissertation). Armed with the photocurrent function in the ideal device and the spatial current density profile, the weighted average can be calculated for the device with current crowding. If this calculated value matches the measured photocurrent in the device with current crowding (as a function of bias), then there is no effect from lateral diffusion. If there is a discrepancy between the two, then more work is needed to understand the effect of lateral diffusion.

6.3 Green LEDs

As the photocurrent in a SQW LED under forward bias is a comparative measure of how much Auger recombination is occurring within the active region, it should be possible to assess the extent to which Auger recombination is more or less important in green InGaN LEDs as compared to blue LEDs. To do this experiment should be relatively simple, requiring only that

the measurements of Chapter 4 of this dissertation be repeated with blue and green SQW epi, ideally grown on the same reactor on the same day.

This last part, growing the material for the comparison on the same reactor and same day is extremely important for experiments using epi grown on academic/research MOCVD reactors, due to the high run-to-run variability and significant process drift. Additionally, as with all MOCVD growth, this will require several growth attempts, much finger-crossing, and a lot of patience.

6.4 ABC Modeling and Photocurrent

The basics of the ABC model of QW radiative efficiency in LEDs is presented in Section 2.5. The essential equation for the radiative efficiency (Equation (2.5.14)) is reproduced below,

$$\eta_{rad} \cong \frac{Bn^2}{An + Bn^2 + Cn^3} \quad (6.4.1)$$

where A, B, and C are the SRH, radiative, and Auger recombination rate coefficients respectively, and n is the carrier density in the QW. The limitations and assumptions inherent in the ABC model are discussed in Section 2.5.

The question addressed in this section will be, what can assuming the ABC model accurately describes recombination in the QW(s) of an LED tell us about the photocurrent or photomodulated light output power we can expect in the LED? The analysis presented in this section is incomplete and should be the subject of further research in conjunction with the other experiments proposed in this chapter.

First, it is important to recognize that in the illuminated state, each QW in the LED experiences a constant electron-hole pair generation rate, \mathcal{G} . This affects the steady-state of the QW by necessarily increasing the recombination and escape rates of carriers. If we make a few (perhaps dubious) simplifying assumptions, namely that

- the capture rate of carriers into each QW is constant,
- the only relevant escape mechanism is Auger hot carrier generation,
- exactly half of the hot carriers generated by Auger recombination travel in each direction

then the change in the sum of the recombination and escape rates, between the dark and illuminated state can be written,

$$\Delta(\mathcal{R}_{recomb} + \mathcal{R}_{esc}) = \mathcal{G} \quad (6.4.2)$$

This is equivalent to writing,

$$\mathcal{G} = \Delta \left(An + Bn^2 + Cn^3 + \frac{1}{2} Cn^3 \right) \quad (6.4.3)$$

which, for small excitation levels, is approximately,

$$\mathcal{G} \cong A\Delta n + 2Bn\Delta n + \frac{9}{2} Cn^2\Delta n \quad (6.4.4)$$

Knowing the ABC coefficients, this equation could be used to solve for Δn as a function of carrier density in a single QW. If the ABC coefficients are constant with carrier density, then this implies that Δn has a functional dependence on carrier density similar to the SRH recombination efficiency:

$$\Delta n = \frac{\mathcal{G} \times n}{An + 2Bn^2 + \frac{9}{2} Cn^3}, \quad \eta_{SRH} = \frac{An}{An + Bn^2 + Cn^3} \quad (6.4.5)$$

That is, approximately constant at low carrier densities, and decreasing monotonically at higher carrier densities. Additionally, the relative increase in light output power is equal to the relative increase in the radiative recombination rate,

$$\frac{\Delta L}{L} = \frac{\Delta(Bn^2)}{Bn^2} \cong \frac{2Bn\Delta n}{Bn^2} = 2 \frac{\Delta n}{n} \quad (6.4.6)$$

which is approximately,

$$\frac{\Delta L}{L} \cong 2 \frac{G}{An + 2Bn^2 + \frac{9}{2}Cn^3} \quad (6.4.7)$$

or monotonically decreasing with carrier density, which is what is observed (see Figure 4.3.5(b) and Figure 5.3.9(b)).

From Equation (6.4.7), it can also be seen that the absolute increase in light output power, ΔL , should have a dependence on carrier density similar to the radiative efficiency of the QW,

$$\Delta L = \frac{\Delta L}{L} \times L \propto 2 \frac{G \times Bn^2}{An + 2Bn^2 + \frac{9}{2}Cn^3} \quad (6.4.8)$$

Using elementary calculus, it can be seen that the expression for ΔL peaks at a carrier density of $n_{peak} = \sqrt{2A/9C}$, while the expression for η_{rad} peaks at a higher carrier density of $n_{peak} = \sqrt{A/C}$. This is contrary to what is observed in both the SQW and MQW LEDs (Figure 4.3.5(a) and Figure 5.3.9(a)), which suggests that the ABC model fails to take into account crucial information on the balance between the two non-radiative recombination mechanisms (defect-assisted SRH-type recombination and band-to-band Auger recombination). This should be a topic of further exploration, in conjunction with a continuation of the experiments described in the next section on MBE-grown LEDs.

6.5 Defect-Assisted Auger

The possibility that there is a defect-assisted Auger recombination process occurring in InGaN QW LEDs is exciting for several reasons. First, this is a heretofore unobserved phenomenon in semiconductors and so, if it could be confirmed that this is actually what is occurring in the lower QWs in MQW LEDs, then that would be big news. Second, it opens up the possibility of studying one of the non-radiative mechanisms that occurs at low injected carrier densities in QW LEDs via a technique such as electro-emission spectroscopy, because there are hot carriers (possibly hot electrons) which escape the active region and possibly make it to the p-contact before losing all of their energy. The usual SRH recombination is totally unobservable as all the energy lost during the transition is simply converted into heat. As phonons are difficult to observe in such thin layers, they can't be used as a signature, even though they are produced in abundance. Lastly, recapturing hot carriers ejected from the lower QWs so that they recombine radiatively might be a fruitful strategy to improving the efficiency of MQW LEDs, with some very clever device design.

Some preliminary work was done to begin looking at defect-assisted Auger recombination by measuring the forward biased photocurrent in MBE grown SQW LED material. MBE material is notoriously inefficient and rarely exhibits efficiency droop at current densities $<100 \text{ A/cm}^2$. So, there should be little of the usual Auger recombination occurring, even at high current densities. The premise is then that if there is a forward photocurrent still, especially at low carrier densities, then there must be another hot carrier producing process occurring within the active region of the device. The following section describes the epi design and the early results of the measurements. Any analysis or further experimentation is firmly within "Future Work" however.

6.5.1 Ongoing Work: Photocurrent in MBE LEDs

The material used for the LEDs was grown, by Dr. Erin Young, using ammonia molecular beam epitaxy (NH₃-MBE). Growth started with a 3 μm GaN-on-sapphire template grown by MOCVD, followed by 450 nm of n-type GaN, doped with $2.5 \times 10^{18} \text{ cm}^{-3}$ Si. Following the n-type GaN was a 10 nm UID GaN barrier, 3 nm of InGaN (emitting at around 450 nm), and 12 nm of UID GaN. Immediately after the active region was 80 nm of p-type GaN with $3 \times 10^{19} \text{ cm}^{-3}$ Mg doping. Lastly was a 5 nm p++ contact layer, with $3 \times 10^{20} \text{ cm}^{-3}$ Mg doping, to form a good tunneling contact. This epi structure is shown in Figure 6.5.1.

5 nm Mg:p++-GaN contact layer
80 nm Mg:p-GaN
10 nm Mg:p-Al _{0.15} Ga _{0.85} N
12 nm UID GaN barrier
3 nm UID InGaN
10 nm UID GaN
450 nm Si:n-GaN
3 μm UID-GaN buffer
Flat Sapphire Substrate

Figure 6.5.1: The epi structure of the MBE-grown SQW LEDs discussed in this chapter. The red layers are doped p-type, the blue layers are doped n-type, and the turquoise layer is the quantum well.

The epi was processed identically to the LEDs discussed in the prior chapters of this dissertation, with 5 nm / 20 nm Pt/Au semi-transparent p-contacts. Analysis of the CTLM IV curves showed that the contacts were Ohmic – absorption of light in the p-contact metal could not cause forward photocurrent through the device.

The dark IV and EQE-I curves for the device are shown in Figure 6.5.2 and Figure 6.5.3, respectively. Crucially, there is no peak in the EQE and it is still rising at moderate to high current densities, when MOCVD LEDs have already entered the droop regime. In the conventional picture of recombination in LED QWs, this implies that the SRH recombination lifetime is very short compared to the radiative recombination rate, and that the carrier density never gets too high.

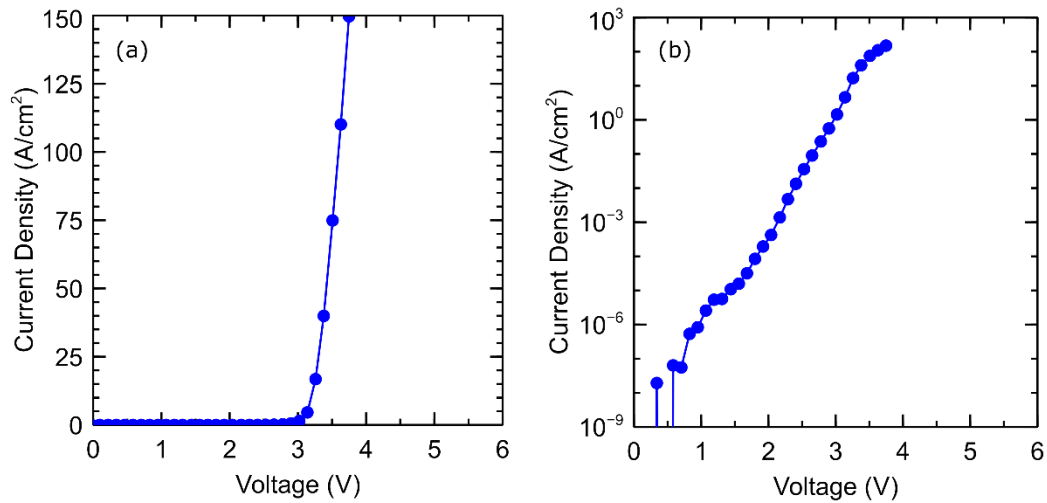


Figure 6.5.2: The measured dark current density vs voltage data for the MBE LED discussed in this chapter. The ordinate axis is linear in (a) and logarithmic in (b).

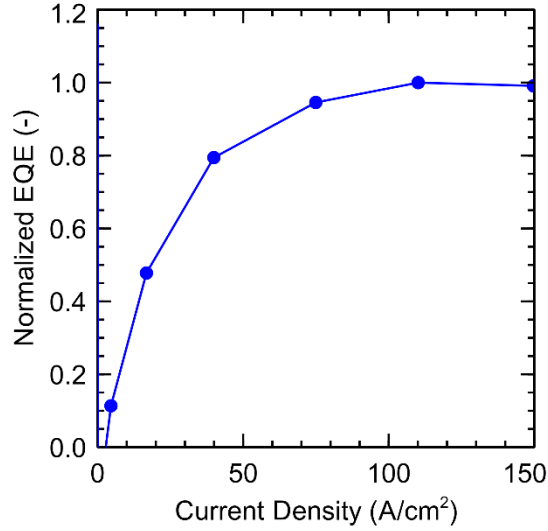


Figure 6.5.3: The dark EQE vs current density data for the MBE LED discussed in this chapter, normalized to the maximum value. There is no observable droop out to 150 A/cm², unlike for the MOCVD-grown LEDs discussed in Chapters 4 and 5..

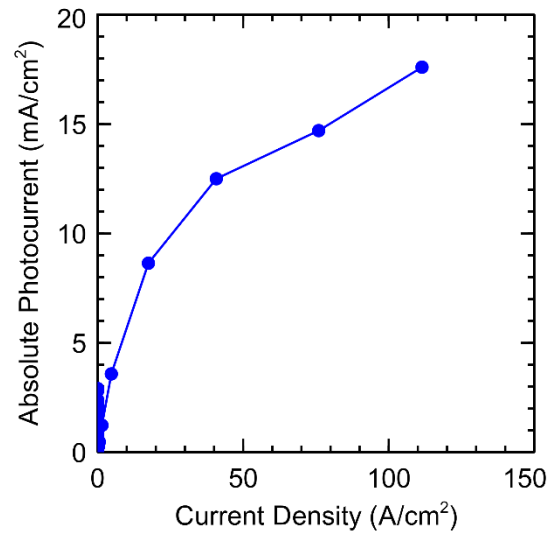


Figure 6.5.4: The absolute value of the measured photocurrent in forward bias, at a pump power density of ~5.7 W/cm², for the MBE-grown LED discussed in this chapter.

Figure 6.5.4 shows the measured forward photocurrent in forward bias in one of the MBE LEDs when forward biased. Clearly, it is non-zero. The sign of the photocurrent in reverse bias was checked by hand, and the cusp in the measured photocurrent (lock-in output) shows

that the sign changed just above the open-circuit voltage. This would appear to be evidence of hot carrier production, even though there is no efficiency droop. Further work is necessary to confirm this with certainty however. Experiments should be performed on MBE LEDs of varying quality, MOCVD LEDs with deliberate impurity (SRH center) incorporation, and they should all be correlated with EES studies to confirm that hot electrons are indeed being produced. Experiments with varying numbers of QWs would be useful to rule out any possibility of contact effects, such as internal photoemission (see [51]). Impact ionization is not expected to be an issue because the p-contacts are Ohmic.

Additionally, lifetime measurements should be performed using time-resolved photoluminescence to get an idea of the carrier density in the active region as it is only an educated guess that the absence of droop implies a low carrier density in the quantum wells.

As the photocurrent appears to be near the same order of magnitude in the MBE LEDs as in the MOCVD SQW LEDs, it would be very useful to have estimates of the rate coefficients for defect-assisted Auger. Unfortunately, theoretical calculations of defect-assisted Auger rates for various defects in InGaN don't appear to have been published to date. Laubsch, et al. did propose that either defect-assisted or phonon-mediated Auger recombination could be involved in LED droop in addition to or instead of direct band-to-band Auger (see [76]), though they don't provide quantitative estimates of the rates. Thorough investigation of this phenomenon would easily fill a dissertation in its own right, and perhaps should.

References

- [1] Claude Weisbuch, “Historical perspective on the physics of artificial lighting,” *Comptes Rendus Physique*, vol. 19, p. 89, 2018.
- [2] “Sunlight,” *Wikipedia.org* [archived]. [Online]. Available: <https://web.archive.org/web/20180811175734/https://en.wikipedia.org/wiki/Sunlight>. [Accessed: 11-Aug-2018].
- [3] O V Lossev, “Luminous carborundum detector and detection effect and oscillations with crystals,” *The London, Edinburgh, and Dublin Philosophical Magazine and Journal of Science*, vol. 6, no. 39, p. 1024, 1928.
- [4] Nikolay Zheludev, “The life and times of the LED -- a 100-year history,” *Nature Photonics*, vol. 1, p. 189, 2017.
- [5] Shuji Nakamura, Masayuki Senoh, and Takashi Mukai, “P-GaN/N-InGaN/N-GaN Double-Heterostructure Blue-Light-Emitting Diodes,” *Japanese Journal of Applied Physics*, vol. 32, pp. L8–L11, 1993.
- [6] Shuji Nakamura, Takashi Mukai, and Masayuki Senoh, “Candela-class high-brightness InGaN/AlGaN double-heterostructure blue-light-emitting diodes,” *Applied Physics Letters*, vol. 64, no. 13, pp. 1687–1689, 1994.
- [7] Justin Iveland, Lucio Martinelli, Jacques Peretti, James S Speck, and Claude Weisbuch, “Direct Measurement of Auger Electrons Emitted from a Semiconductor Light-Emitting Diode under Electrical Injection: Identification of the Dominant Mechanism for Efficiency Droop,” *Physical Review Letters*, vol. 110, p. 177406, 2013.
- [8] W Shockley, “The theory of p-n junctions in semiconductors and p-n junction transistors,” *Bell Systems Technical Journal*, vol. 28, no. 3, p. 435, 1949.
- [9] Z Z Bandic, P M Bridger, E C Piquette, and T C McGill, “Electron diffusion length and lifetime in p-type GaN,” *Applied Physics Letters*, vol. 73, no. 22, p. 3276, 1998.
- [10] Takao Miyajima, Masafumi Ozawa, Tsunenori Asatsuma, Hiroji Kawai, and Masao Ikeda, “Minority carrier diffusion length in GaN and ZnSe,” *Journal of Crystal Growth*, vol. 189–190, pp. 768–772, 1998.
- [11] J C Gonzalez, K L Bunker, and P E Russell, “Minority-carrier diffusion length in a GaN-based light-emitting diode,” *Applied Physics Letters*, vol. 79, p. 1567, 2001.
- [12] K Kumakura, T Makimoto, N Kobayashi, T Hashizume, T Fukui, and H Hasegawa, “Minority carrier diffusion length in GaN: Dislocation density and doping concentration dependence,” *Applied Physics Letters*, vol. 86, p. 052105, 2005.
- [13] Hisashi Masui, “Diode ideality factor in modern light-emitting diodes,” *Semiconductor Science and Technology*, vol. 26, no. 7, p. 075011, 2011.
- [14] H P Maruska and J J Tietjen, “The preparation and properties of vapor-deposited single-crystalline GaN,” *Applied Physics Letters*, vol. 15, no. 10, pp. 327–329, 1969.
- [15] Masakatsu Suzuki, Takeshi Uenoyama, and Akira Yanase, “First-principles calculations of effective-mass parameters of AlN and GaN,” *Physical Review B*, vol. 52, no. 11, pp. 8132–8139, 1995.
- [16] V Yu Davydov *et al.*, “Absorption and Emission of Hexagonal InN. Evidence of Narrow Fundamental Band Gap,” *Physica Status Solidi B*, vol. 229, no. 3, pp. r1–r3, 2002.

- [17] V Yu Davydov *et al.*, “Band Gap of InN and In-Rich $\text{In}_x\text{Ga}_{1-x}\text{N}$ alloys ($0.36 < x < 1$),” *Physica Status Solidi B*, vol. 230, no. 2, pp. R4–R6, 2002.
- [18] J W Huang, T F Kuech, Hongqiang Lu, and Ishwara Bhat, “Electrical characterization of Mg-doped GaN grown by metalorganic vapor phase epitaxy,” *Applied Physics Letters*, vol. 68, no. 17, pp. 2392–2394, 1996.
- [19] Shuji Nakamura, Takashi Mukai, Masayuki Senoh, and Naruhito Iwasa, “Thermal Annealing Effects on P-Type Mg-Doped GaN Films,” *Japanese Journal of Applied Physics*, vol. 31, no. Part 2, No. 2B, pp. L139–L142, 1992.
- [20] Herbert Kroemer, “A proposed class of heterojunction injection lasers,” *Proceedings of the IEEE*, vol. 51, no. 12, pp. 1782–1782, 1963.
- [21] Yuh-Renn Wu, Ravi Shivaraman, Kuang-Chung Wang, and James S Speck, “Analyzing the physical properties of InGaN multiple quantum well light emitting diodes from nano scale structure,” *Applied Physics Letters*, vol. 101, p. 083505, 2012.
- [22] Aurelien David, Michael J Grundmann, John F Kaeding, Nathan F Gardner, Theodoros G Mihopoulos, and Michael R Krames, “Carrier distribution in (0001) InGaN/GaN multiple quantum well light-emitting diodes,” *Applied Physics Letters*, vol. 92, p. 053502, 2008.
- [23] David A Browne, Micha N Fireman, Baishakhi Mazumder, Leah Y Kuritzky, Yuh-Renn Wu, and James S Speck, “Vertical transport through AlGaN barriers in heterostructures grown by ammonia molecular beam epitaxy and metalorganic chemical vapor deposition,” *Semiconductor Science and Technology*, vol. 32, p. 025010, 2017.
- [24] Yukio Narukawa, Masatsugu Ichikawa, Daisuke Sanga, Masahiko Sano, and Takashi Mukai, “White light emitting diodes with super-high luminous efficacy,” *Journal of Physics D: Applied Physics*, vol. 43, p. 354002, 2010.
- [25] Parthiban Santhanam, Dodd Joseph Gray Jr., and Rajeev J Ram, “Thermoelectrically Pumped Light-Emitting Diodes Operating above Unity Efficiency,” *Physical Review Letters*, vol. 108, p. 097403, 2012.
- [26] Leah Y Kuritzky *et al.*, “High wall-plug efficiency blue III-nitride LEDs designed for low current density operation,” *Optics Express*, vol. 25, no. 24, p. 30696, 2017.
- [27] W Shockley and W T Read Jr, “Statistics of the Recombinations of Holes and Electrons,” *Physical Review*, vol. 87, no. 5, p. 835, 1952.
- [28] William P Dumke, “Spontaneous Radiative Recombination in Semiconductors,” *Physical Review*, vol. 105, no. 1, pp. 139–144, 1957.
- [29] P T Landsberg, “The band-band Auger effect in semiconductor,” *Solid-State Electronics*, vol. 30, no. 11, pp. 1107–1115, 1987.
- [30] P T Landsberg and A R Beattie, “Auger effect in semiconductors,” *Journal of the Physical Chemistry of Solids*, vol. 8, p. 73, 1959.
- [31] P T Landsberg and D J Robbins, “The first 70 semiconductor Auger processes,” *Solid-State Electronics*, vol. 21, p. 1289, 1978.
- [32] T R Chen, B Chang, L C Chiu, K L Yu, S Margalit, and A Yariv, “Carrier leakage and temperature dependence of InGaAsP lasers,” *Applied Physics Letters*, vol. 43, p. 217, 1983.
- [33] Guan-Bo Lin, David Meyaard, Jaehee Cho, E Fred Schubert, Hyunwook Shim, and Cheolsoo Sone, “Analytic model for the efficiency droop in semiconductors with asymmetric carrier transport properties based on drift-induced reduction of injection efficiency,” *Applied Physics Letters*, vol. 100, p. 161106, 2012.

- [34] Xianfeng Ni, Qian Fan, Ryoko Shimada, Umit Ozgur, and Hadis Morkoc, "Reduction of efficiency droop in InGaN light emitting diodes by coupled quantum wells," *Applied Physics Letters*, vol. 93, p. 171113, 2008.
- [35] X Ni *et al.*, "The effect of ballistic and quasi-ballistic electrons on the efficiency droop of InGaN light emitting diodes," *Physica Status Solidi RRL*, vol. 4, no. 8–9, p. 194, 2010.
- [36] Xing Li, Huiyong Liu, X Ni, Umit Ozgur, and Hadis Morkoc, "Effect of carrier spillover and Auger recombination on the efficiency droop in InGaN-based blue LEDs," *Superlattices and Microstructures*, vol. 47, p. 118, 2010.
- [37] S Hammersley *et al.*, "Study of efficiency droop and carrier localisation in an InGaN/GaN quantum well structure," *Physica Status Solidi C*, vol. 8, no. 7–8, p. 2194, 2011.
- [38] S Hammersley *et al.*, "The consequences of high injected carrier densities on carrier localization and efficiency droop in InGaN/GaN quantum well structures," *Journal of Applied Physics*, vol. 111, p. 083512, 2012.
- [39] T J Badcock *et al.*, "Carrier density dependent localization and consequences for efficiency droop in InGaN/GaN quantum well structure," *Japanese Journal of Applied Physics*, vol. 52, p. 08JK10, 2013.
- [40] M J Davies, T J Badcock, P Dawson, M J Kappers, R A Oliver, and C J Humphreys, "High excitation carrier density recombination dynamics of InGaN/GaN quantum well structures: Possible relevance to efficiency droop," *Applied Physics Letters*, vol. 102, p. 022106, 2013.
- [41] Matthew J Davies, Tom J Badcock, Philip Dawson, Rachel A Oliver, Menno J Kappers, and Colin J Humphreys, "High excitation density recombination dynamics in InGaN/GaN quantum well structures in the droop regime," *Physica Status Solidi C*, vol. 11, no. 3–4, p. 694, 2014.
- [42] Aniela Dunn *et al.*, "Investigating efficiency droop in InGaN/GaN quantum well structures using ultrafast time-resolved terahertz and photoluminescence spectroscopy," *Physica Status Solidi C*, vol. 13, no. 5–6, p. 252, 2016.
- [43] Y C Shen, G O Mueller, S Watanabe, N F Gardner, A Munkholm, and M R Krames, "Auger recombination in InGaN measured by photoluminescence," *Applied Physics Letters*, vol. 91, p. 141101, 2007.
- [44] Emmanouil Kioupakis, Patrick Rinke, Kris T Delaney, and Chris G Van de Walle, "Indirect Auger recombination as a cause of efficiency droop in nitride light-emitting diodes," *Applied Physics Letters*, vol. 98, p. 161107, 2011.
- [45] Kris T Delaney, Patrick Rinke, and Chris G Van de Walle, "Auger recombination rates in nitrides from first principles," *Applied Physics Letters*, vol. 94, p. 191109, 2009.
- [46] Jaehee Cho, E Fred Schubert, and Jong Kyu Kim, "Efficiency droop in light-emitting diodes: Challenges and countermeasures," *Laser & Photonics Reviews*, vol. 7, no. 3, pp. 408–421, 2013.
- [47] W A Phillips, E J Thrush, Y Zhang, and C J Humphreys, "Studies of efficiency droop in GaN based LEDs," *Physica Status Solidi C*, vol. 9, no. 3–4, pp. 765–769, 2012.
- [48] Anatoli S Polkovnikov and Georgy G Zegrya, "Auger recombination in semiconductor quantum wells," *Physical Review B*, vol. 58, no. 7, p. 4039, 1998.
- [49] M Shahmohammadi *et al.*, "Enhancement of Auger recombination induced by carrier localization in InGaN/GaN quantum wells," *Physical Review B*, vol. 95, p. 125314.

- [50] Roman Vaxenburg, Anna Rodina, Efrat Lifshitz, and Alexander L Efros, “The role of polarization fields in Auger-induced efficiency droop in nitride-based light-emitting diodes,” *Applied Physics Letters*, vol. 103, no. 22, p. 221111, 2013.
- [51] K Konuma, Y Asano, and K Hirose, “Internal photoemission spectroscopy for a PtSi/p-type Si Schottky-barrier diode,” *Physical Review B*, vol. 51, no. 19, pp. 13187–13191, 1995.
- [52] L S Yu, Q J Xing, D Qiao, S S Lau, K S Boutros, and J M Redwing, “Internal photoemission measurement of Schottky barrier height for Ni on AlGaIn/GaN heterostructure,” *Applied Physics Letters*, vol. 73, no. 26, pp. 3917–3919, 1998.
- [53] Hong Ye, G W Wicks, and P M Fauchet, “Hot hole relaxation dynamics in p-GaN,” *Applied Physics Letters*, vol. 77, no. 8, pp. 1185–1187, 2000.
- [54] Martin A Green, Jianhua Zhao, Aihua Wang, Peter J Reece, and Michael Gal, “Efficient silicon light-emitting diodes,” *Nature*, vol. 412, p. 805, 2001.
- [55] Byung-Jun Ahn *et al.*, “Experimental determination of current spill-over and its effect on the efficiency droop in InGaIn/GaN blue-light emitting-diodes,” *Applied Physics Letters*, vol. 100, p. 031905, 2012.
- [56] Yufeng Li *et al.*, “Green light emitting diodes under photon modulation,” in *Materials Research Society Symposium Proceedings*, 2008, vol. 1040.
- [57] “Lock-in Amplifiers,” *Bentham Instruments Ltd.* [Online]. Available: <https://web.archive.org/web/20180905205631/http://support.bentham.co.uk/support/solutions/articles/13000036065-lock-in-amplifier-tutorial>. [Accessed: 05-Sep-2018].
- [58] A A Efremov *et al.*, “Effect of the Joule heating on the quantum efficiency and choice of thermal conditions for high-power blue InGaIn/GaN LEDs,” *Semiconductors*, vol. 40, no. 5, p. 605, 2006.
- [59] “PyVISA,” *Github.com* [archived]. [Online]. Available: <https://web.archive.org/web/20180812191950/https://github.com/pyvisa/pyvisa>. [Accessed: 12-Aug-2018].
- [60] Friedhard Romer and Bernd Witzigmann, “Effect of Auger recombination and leakage on the droop in InGaIn/GaN quantum well LEDs,” *Optics Express*, vol. 22, no. S6, p. A1440, 2014.
- [61] Friedhard Romer, Marcus Deppner, Christian Range, and Bernd Witzigmann, “Auger recombination and leakage in InGaIn/GaN quantum well LEDs,” *Proceedings of SPIE*, vol. 8986, pp. 89861R–1, 2014.
- [62] K D Chik, “A theoretical analysis of Auger recombination induced energetic carrier leakage in GaInAsP/InP double heterojunction lasers and light emitting diodes,” *Journal of Applied Physics*, vol. 63, p. 4688, 1988.
- [63] K D Chik, “On the effects of Auger recombination and energetic carrier leakage in GaInAsP/InP light emitting diodes,” *Journal of Applied Physics*, vol. 64, p. 2138, 1988.
- [64] K D Chik and B A Richardson, “On the origin of the carrier leakage in GaInAsP/InP double-heterojunction lasers,” *Journal of Applied Physics*, vol. 67, p. 2660, 1990.
- [65] Gregory L Belenky, R F Kazarinov, John Lopata, Serge Luryi, T Tanbun-Elk, and P A Garbinski, “Direct measurement of the carrier leakage out of the active region in InGaAsP/InP laser heterostructures,” *IEEE Transactions on Electron Devices*, vol. 42, no. 2, p. 215, 1995.

- [66] S Yamakoshi, T Sanada, O Wada, I Umebu, and T Sakurai, "Direct observation of electron leakage in InGaAsP/InP double heterostructure," *Applied Physics Letters*, vol. 40, p. 144, 1982.
- [67] Dieter K Schroder, *Semiconductor Material and Device Characterization*, Third. John Wiley & Sons, Inc., 2006.
- [68] V Bougrov, M E Levinshtein, S L Rumyantsev, and A Zubrilov, "Chapter 1: Gallium Nitride (GaN)," in *Properties of Advanced Semiconductor Materials GaN, AlN, InN, BN, SiC, SiGe*, New York: John Wiley & Sons, Inc., 2001, pp. 1–30.
- [69] Chi-Kang Li *et al.*, "Localization landscape theory of disorder in semiconductors. III. Application to carrier transport and recombination in light emitting diodes," *Physical Review B*, vol. 95, p. 144206, 2017.
- [70] "SiLENSe," www.str-soft.com. [Online]. Available: <https://web.archive.org/web/20180812193632/http://www.str-soft.com/products/SiLENSe/>. [Accessed: 12-Aug-2018].
- [71] P T Landsberg, "Trap-Auger recombination in silicon of low carrier densities," *Applied Physics Letters*, vol. 50, p. 745, 1987.
- [72] P T Landsberg, "Trap-Auger effect in relatively pure silicon," *Journal of Luminescence*, vol. 40/41, pp. 587–588, 1988.
- [73] P T Landsberg, C Rhys-Roberts, and P Lal, "Auger recombination and impact ionization involving traps in semiconductors," *Proceedings of the Physical Society*, vol. 84, p. 915, 1964.
- [74] G F Neumark, "Auger theory at defects -- application to states with two bound particles in GaP," *Physical Review B*, vol. 7, no. 8, p. 3802, 1973.
- [75] H G Grimmeiss and M Kleverman, "Local Auger effects at point defects in silicon," *Journal of the Physical Chemistry of Solids*, vol. 49, no. 6, pp. 615–626, 1988.
- [76] Ansgar Laubsch *et al.*, "On the origin of IQE-'droop' in InGaN LEDs," *Physica Status Solidi C*, vol. 6, no. S2, p. S913, 2009.

A. Photolithography Process Follower

This appendix contains a reproduction of the process follower for the nanofabrication process used to manufacture the LEDs presented in this dissertation. All nanofabrication was performed in the cleanrooms in the UCSB Nanofabrication Facility.

A.1 Main Process

Activation, Indium Removal			
Activate	MOCVD Lab Oven/RTA	600 C, 15', air	DO NOT ACTIVATE WITH INDIUM ON SAMPLE
Remove Indium from QT	Acid Bench	Aqua Regia, 140 C, 10', Repeat 3x	HNO ₃ +HCl 1:3 by volume
Activate	MOCVD Lab Oven/RTA	600 C, 15', air	DO NOT ACTIVATE WITH INDIUM ON SAMPLE
Dice			
Spin on PR	Spin Bench	nLoF 2020	Flood expose and Hard Bake before dicing!
Dice	Dicing Saw	11mm x 11mm	18krpm, 0.75mm/s, 2.187-8C-30RU-3, 11.2mm index
Strip PR	Solvent Bench	NMP, 80 C, rinse clean with Ace/Iso/DI	leave in NMP until PR is gone (>30 min is probably ok)
Solvent Clean	Solvent Bench	Ace/Iso//DI 3' ea.	Use RT ultrasonic bath
Particulate Clean (optional)	Acid Bench	3:1 H ₂ SO ₄ :H ₂ O 30"	Piranha dip for super clean!!!
Mesa			
Mesa Lithography	Spin Bench	SPR 220-3.0	See Litho Follower for Details
UV Ozone Descum	PR-100	1200"	
Mesa etch	ICP #2	Recipe 140, SEB_GaN (~650nm/min)	5' #106 first on clean wafer, then 1'30" #140 on etch wafer
Solvent Clean	Solvent Bench	Ace/Iso//DI 3' ea.	Use RT ultrasonic bath, HI/10/10
n-contact			

n-Contact Lithography	Spin Bench	nLoF 2020	See Litho Follower for Details
UV Ozone Descum	PR-100	1200"	
HCl Dip	Acid Bench	1:1 DI:HCl, 30", DI Rinse	Immediately before deposition
n-Metal Deposition	E-beam #3	Ti/Au/Ti, 0.300/1.000/0.080 kA	
Liftoff	Solvent Bench	NMP, 80C, 20'	blow off film with pipette with jet of NMP in jar
Solvent Clean	Solvent Bench	Ace/Iso//DI 3' ea.	rinse several times in DI, U/S clean on LO
p-contact			
p-Contact Lithography	Spin Bench	nLOF 2020	See Litho Follower for Details
UV Ozone Descum	PR-100	1200"	
HCl Dip	Acid Bench	1:1 DI:HCl, 30", DI Rinse	Immediately before deposition
p-contact Deposition	E-Beam #4	Pd/Au, 0.050/0.150 kA	
Liftoff	Solvent Bench	NMP, 80C, 20'	blow off film with pipette with jet of NMP in jar
Solvent Clean	Solvent Bench	Ace/Iso//DI 3' ea.	rinse several times in DI, U/S clean on LO
SiO2 underlayer			
H2O Dip	Wet Bench	DI, 30"	Immediately before deposition
SiO2 deposition	PECVD #1	10' SiO2 clean, 150 nm/H2O dip/150 nm	Dip in DI in between two ~12' depositions, include Si piece
SiO2 Lithography	Spin Bench	SPR 220-3.0	See Litho Follower for Details
UV Ozone Descum	PR-100	1200"	
SiO2 etch	HF Bench	BHF, try 30" first, then try 5" dips until Si monitor is hydrophobic	
PR Removal	Solvent Bench	NMP, 80C, 20'	after soaking for 20', also U/S clean on LO
Solvent Clean	Solvent Bench	Ace/Iso//DI 3' ea.	rinse several times in DI, U/S clean on LO
Pads			
p-Pad Lithography	Spin Bench	nLOF 2020	See Litho Follower for Details
UV Ozone Descum	PR-100	1200"	
HCl Dip	Acid Bench	1:1 DI:HCl, 30", DI Rinse	Immediately before deposition

p-contact Deposition	E-Beam #3	Ti/Au, 0.300/5.0 kA	
Liftoff	Solvent Bench	NMP, 80C, 20'	blow off film with pipette with jet of NMP in jar
Solvent Clean	Solvent Bench	Ace/Iso//DI 3' ea.	rinse several times in DI, U/S clean on LO

A.2 Photolithography Processes

AZ nLOF 2020 (Negative)	
Dehydration Bake	115 C, >60"
Spin	AZ nLOF 2020 - 3000rpm, 30", 20krpm/s
Bake	110°C, 60"
Expose	10", 7.5mW/cm ²
Post Exposure Bake	110°C, 60"
Develop	AZ300-MIF, 55"
Rinse	DI, 1'
SPR 220 3.0 (Positive)	
Dehydration Bake	115 C, >60"
Spin	SPR 2020-3.0, 3500 rpm, 30", 20000 RPM/sec
Soft Bake	115°C, 90"
Expose	25", 7.5mW/cm ²
Post Exposure Bake	115°C, 60"
Develop	AZ300-MIF, 50"
Rinse	DI, 1'

B. Control Program Code

This appendix contains the Python computer code used to collect the photocurrent data. It is written in Python 3.

B.1 Python 3 Code

```
# -*- coding: utf-8 -*-
"""
Main program for photocurrent measurements on LEDs with:
    Keithley 2400 SourceMeter
    Keithley 2000 Digital MultiMeter
    SR830 Lock-in Amplifier
    ILX Lightwave Temperature Controller and TEC stage

Includes added dark measurement capability

Created: 08/31/2016
Last Edited: 04/23/2018
Author: Andrew Espenlaub
"""

import visa
import configparser
import numpy as np
import tkinter as tk
import tkinterFileDialog as tkFileDialog
import datetime as dt
import pytz
import csv
import sys
import time

#default file info
config_filename = "C:\\Users\\MBE\\Desktop\\PhotoCurrent Config
Files\\PhotoCurrent_LIV_DEFAULT_CONFIG.conf"
output_filepath =
"C:\\Users\\MBE\\Desktop\\PhotoCurrent_Data\\" #default output
directory, i.e. - same directory
global output_filename
```



```

#lock-in parameter encoding dictionaries
ext_ref_slope_dict = {'sine':0,'ttl_rising':1,'ttl_falling':2}
t_constant_dict = {
    '10 us':0,'30 us':1,
    '100 us':2,'300 us':3,
    '1 ms':4,'3 ms':5,
    '10 ms':6,'30 ms':7,
    '100 ms':8,'300 ms':9,
    '1 s':10,'3 s':11,
    '10 s':12,'30 s':13,
    '100 s':14,'300 s':15,
    '1 ks':16,'3 ks':17,
    '10 ks':18,'30 ks':19
}
low_pass_filter_slope_dict = {'6':0,'12':1,'18':2,'24':3}
sensitivity_dict = {
    '2 nV':0,'5 nV':1,'10 nV':2,
    '20 nV':3,'50 nV':4,'100 nV':5,
    '200 nV':6,'500 nV':7,'1 uV':8,
    '2 uV':9,'5 uV':10,'10 uV':11,
    '20 uV':12,'50 uV':13,'100 uV':14,
    '200 uV':15,'500 uV':16,'1 mV':17,
    '2 mV':18,'5 mV':19,'10 mV':20,
    '20 mV':21,'50 mV':22,'100 mV':23,
    '200 mV':24,'500 mV':25,'1 V':26
}

#declare global variables to read from config file so that they
will be accessible from initial_setup()
global parser
global dark_measurement
global randomize
global temperatures
global filters
global num_readings
global src_gpib
global lia_gpib
global dmm_gpib
global src_nplc
global src_filter_state
global src_filter_count
global src_delay
global src_reverse_bias_dir
global src_control_mode
global src_compliance
global src_setpoint_mode

```

```

global src_setpoints
global ext_ref_slope
global min_t_constant
global max_t_constant
global low_pass_filter_slope
global num_snaps
global dmm_nplc
global dmm_filter_state
global dmm_filter_count
global dmm_num_channels
global dmm_route_string

#declare global variables for the instruments
global SRC
global LIA
global DMM

#####
#####
#####      Main Function, to be called at entry point at end of
file      #####
#####
#####

def main():
    #setup root to allow use of tkfdialog
    root = tk.Tk()
    root.withdraw()
    #get filename of config file from user via tkfdialog
    global config_filename
    config_filename =
tkfdialog.askopenfilename(defaulttextextension='.conf',initialdir=
"C:\\Users\\MBE\\Desktop\\PhotoCurrent          Config
Files\\",initialfile="PhotoCurrent_LIV_DEFAULT_CONFIG.conf",ti
tle="Select config file for measurement")

    #parse config file
    read_config_file()

    #open visa resources
    rm = visa.ResourceManager()
    global SRC,LIA,DMM
    SRC = rm.open_resource(src_gpib,timeout=None) #Keithley
2400 SourceMeter
    LIA = rm.open_resource(lia_gpib,timeout=None) #Stanford
Reserach Systems SR830 Lock-in Amplifier

```

```

DMM = rm.open_resource(dmm_gpib,timeout=None) #Keithley
2000 Digital MultiMeter with 2000-SCAN card

#do initial setup of instruments
initial_setup()

#get a timestamped name for the output file
global output_filename
output_filename = get_outfilename()

#write header information to the output file
write_header()

#loop over temperatures
global temperatures
global num_setpoints,src_setpoints,filters
num_setpoints = len(src_setpoints)
for T in temperatures:
    #Ask user to set temperature stage to correct
temperature
    input("Set temperature stage to "+T+" deg C and press
\"ENTER\" to continue")
    #Wait for temperature reading to stabilize
wait_temperature()

    #Do dark measurement if specificed
global dark_measurement
if dark_measurement=='on':
    measure_LIV(T,'-',dark=True)

    #Ask user to turn on laser
    input("Turn on the pump source and press \"ENTER\" to
continue")
    #Wait for laser output to stabilize (feedback or pre-
programmed wait time...?)
    '''
    wait_laser()
    '''
    #Ask user to make laser power measurement
    input("Measure pump source power and press \"ENTER\" to
continue")

#loop over filters
for F in filters:
    #Ask user to set ND filter to correct value
    input("Set ND filter wheel to OD "+F+" and press
\"ENTER\" to continue")

```

```

        measure_LIV(T,F,dark=False)

#reset instruments, clear status bytes and interfaces
SRC.write("*RST;*CLS;*IFC")
LIA.write("*RST;*CLS;*IFC")
DMM.write("*RST;*CLS;*IFC")

#####
#####
#####      Other functions, which get called in the main function
#####
#####
#####

def read_config_file():
    '''
    parses parameters from the config file
    '''
    #read in config file
    global parser
    parser = configparser.ConfigParser()
    parser.read(config_filename)

    #read [General] parameters from config file
    try:
        params = parser['General']
        global
        dark_measurement,randomize,temperatures,filters,num_readings
        dark_measurement = params['dark_measurement']
        randomize = params['randomize']
        temperatures = params['temperatures'].split(',')
        filters = params['filters'].split(',')
        num_readings = int(params['num_readings'])
    except ValueError:
        sys.exit('Check that the [General] parameters in the
config file are the right datatype')

    #read [GPIB Addresses] parameters from config file
    try:
        params = parser["GPIB Addresses"]
        global src_gpib,lia_gpib,dmm_gpib
        src_gpib =
"GPIB0::"+params["sourcemeter_gpib"]+"::INSTR"
        lia_gpib = "GPIB0::"+params["lock-in_gpib"]+"::INSTR"
        dmm_gpib = "GPIB0::"+params["dmm_gpib"]+"::INSTR"
    except ValueError:

```

```

        sys.exit('Check that the [GPIB Addresses] parameters in
the config file are right datatype')

#read [SourceMeter] parameters from config file
try:
    params = parser['SourceMeter']
    global
src_nplc,src_filter_state,src_filter_count,src_delay,src_rever
se_bias_dir
    global
src_control_mode,src_compliance,src_setpoint_mode,src_setpoint
s
    src_nplc = float(params['src_nplc'])
    src_filter_state = params['src_filter_state']
    src_filter_count = int(params['src_filter_count'])
    src_delay = float(params['src_delay'])
    src_reverse_bias_dir = params['src_reverse_bias_dir']
    src_control_mode = params['src_control_mode']
    src_compliance = float(params['src_compliance'])
    src_setpoint_mode = params['src_setpoint_mode']
    src_setpoints = np.array([])
    if src_setpoint_mode=='sweep':
        start,stop,num = [float(sp) for sp in
params['src_setpoints'].split(',')]
        num = int(num)
        src_setpoints = np.linspace(start,stop,num)
    elif src_setpoint_mode=='list':
        src_setpoints = np.array([float(sp) for sp in
params['src_setpoints'].split(',')])
    else:
        raise ValueError

    if src_reverse_bias_dir=='on' and len(src_setpoints)>0:
        src_setpoints *= -1 #reverse the bias direction if
specified
    if randomize=='on' and len(src_setpoints)>0:
        src_setpoints =
np.random.permutation(src_setpoints) #randomize the setpoint
list if specified
except ValueError:
    sys.exit("Check that the [SourceMeter] parameters in
the config file are the right datatype")

#read [Lock-In] parameters from config file
try:
    params = parser['Lock-in']

```

```

        global
        ext_ref_slope,min_t_constant,max_t_constant,autogain_sens_start,low_pass_filter_slope,num_snaps
        ext_ref_slope =
        ext_ref_slope_dict[params['ext_ref_slope'].lower()]
        min_t_constant =
        t_constant_dict[params['min_t_constant'].lower()]
        max_t_constant =
        t_constant_dict[params['max_t_constant'].lower()]
        autogain_sens_start =
        sensitivity_dict[params['autogain_sens_start']]
        low_pass_filter_slope =
        low_pass_filter_slope_dict[params['low_pass_filter_slope']]
        num_snaps = int(params['num_snaps'])
    except ValueError:
        sys.exit("Check that the [Lock-in] parameters in the
        config file are the right datatype")

    #read [DMM] parameters from config file
    try:
        params = parser['DMM']
        global
        dmm_nplc,dmm_filter_state,dmm_filter_count,dmm_num_channels,dm
        m_route_string
        dmm_nplc = float(params['dmm_nplc'])
        dmm_filter_state = params['dmm_filter_state']
        dmm_filter_count = int(params['dmm_filter_count'])
        dmm_num_channels = int(params['dmm_num_channels'])

        #set the route:scan:internal string to
        (@1,2,...,dmm_num_channels)
        dmm_route = list(range(1,dmm_num_channels))
        commas = [',']* (dmm_num_channels-1)
        dmm_route = [str(val) for pair in zip(dmm_route,commas)
        for val in pair]+[str(dmm_num_channels)]
        dmm_route_string = "("
        for el in dmm_route:
            dmm_route_string = dmm_route_string+el
            dmm_route_string = dmm_route_string+')'
    except ValueError:
        sys.exit("Check that the [DMM] parameters in the config
        file are the right datatype")

def initial_setup():
    '''
    Method to perform initial setup of sourcemeter, multimeter
    and lock-in amplifier

```

```

'''
#reset instruments, clear status bytes and interfaces
SRC.write("*RST;*CLS;*IFC")
LIA.write("*RST;*CLS;*IFC")
DMM.write("*RST;*CLS;*IFC")

#SourceMeter setup
##SRC.write("display:enable off")
SRC.write("source:clear:auto off")
SRC.write("source:delay:auto off")
SRC.write("source:delay %f" % (src_delay))
if src_control_mode == "current":
    SRC.write("source:function:mode current")
    SRC.write("source:current:mode fixed")
    SRC.write("source:current:range:auto on")
    SRC.write("source:current:level 0.0") #set bias to 0A
initially
    SRC.write("sense:voltage:dc:protection:level %f" %
(src_compliance))
    elif src_control_mode == "voltage":
        SRC.write("source:function:mode voltage")
        SRC.write("source:voltage:mode fixed")
        SRC.write("source:voltage:range:auto on")
        SRC.write("source:voltage:level 0.0") #set bias to 0V
initially
    SRC.write("sense:current:dc:protection:level %f" %
(src_compliance))
    SRC.write("sense:function:off:all")
    SRC.write("sense:function:concurrent on")
    SRC.write("sense:function:on 'voltage:dc','current:dc'")
    SRC.write("sense:voltage:dc:range:auto on")
    SRC.write("sense:current:dc:range:auto on")
    SRC.write("sense:voltage:nplcycles %f" % float(src_nplc))
    SRC.write("sense:current:nplcycles %f" % float(src_nplc))
    SRC.write("sense:average:state "+src_filter_state)
    SRC.write("sense:average:tcontrol repeat")
    SRC.write("sense:average:count %d" % int(src_filter_count))
    SRC.write("system:rsense on")
    SRC.write("trigger:count %d" % (num_readings))
    SRC.write("trigger:source tlink")
    SRC.write("trigger:direction source") #bypasses first input
trigger from DMM to start sweep
    SRC.write("trigger:input source")
    SRC.write("trigger:output sense")
    SRC.write("trace:clear")
    SRC.write("trace:points 1")
    SRC.write("trace:feed sense")

```

```

SRC.write("trace:feed:control next")
SRC.write("format:elements voltage,current")
print("finished with SourceMeter setup")

#Lock-In setup
LIA.write("OUTX 1") #select GPIB hardware output interface
LIA.write("PHAS 0") #phase is set to 0 degrees
LIA.write("ISRC 0") #input source to A
LIA.write("IGND 0") #input grounding set to Floating
LIA.write("ICPL 0") #input coupling set to AC
LIA.write("ILIN 0") #input line notch filters set to None
LIA.write("FMOD 0") #external refernce
LIA.write("RSLP %d" % (ext_ref_slope)) #external reference
slope set
LIA.write("OFSL %d" % (low_pass_filter_slope)) #low pass
filter slope set
LIA.write("RMOD 0") #high reserve
LIA.write("SYNC 1") #SYNC filter on because chopping
frequency will be <200Hz
LIA.write("*SRE 0") #reset Serial Poll Enable Register so
nothing generates an SRQ
#LIA.write("LOCL 2") #local lockout mode enabled
print("finished with Lock-in setup")

#Digital Multimeter setup
##DMM.write("display:enable off")
DMM.write("route:scan:lselect internal")
DMM.write("route:scan:internal "+dmm_route_string)
DMM.write("sense:hold:state off")
DMM.write("sense:function 'voltage:dc'")
DMM.write("sense:voltage:dc:range:auto on")
DMM.write("sense:voltage:dc:nplcycles %f" % dmm_nplc)
DMM.write("sense:voltage:dc:average:state
"+dmm_filter_state)
DMM.write("sense:voltage:dc:average:tcontrol repeat")
DMM.write("sense:voltage:dc:average:count %d" %
dmm_filter_count)
DMM.write("trigger:source external")
DMM.write("trigger:count %d" % (num_readings))
DMM.write("trigger:delay 0")
DMM.write("sample:count %d" % (dmm_num_channels))
DMM.write("trace:clear")
DMM.write("trace:points %d" %
(dmm_num_channels*num_readings)) #MUST COME BEFORE FEED CONTROL
AND AFTER TRIG AND SMPL COUNT
DMM.write("trace:feed sense")
DMM.write("trace:feed:control next")

```



```

DMM.write("format:elements reading")
print("finished with DMM setup")

def get_outfilename():
    '''
    Creates timestamped output filename
    '''
    #Get date and time for file name
    timezone = 'US/Pacific' #UTC-8:00
    timestamp = dt.datetime.now().timestamp()
    datetime = dt.datetime.fromtimestamp(timestamp,tz=pytz.timezone(timezone)).isoformat()
    year,month,day = datetime[2:4],datetime[5:7],datetime[8:10]
    hour,minute,second = datetime[11:13],datetime[14:16],datetime[17:19]
    date = year+month+day
    hhmmss = hour+minute+second

    #Write header information to file
    try:
        params = parser['Sample']
        if 'led_name' in params.keys():
            LED_name = params['led_name']
        else:
            LED_name = ''
    except Exception:
        sys.exit("Configuration file must include line with keyword \"LED_NAME\"")

    output_filename = date+"_"+hhmmss+"_PhotoCurrent_LIV_"+LED_name+".csv"

    return output_filepath+output_filename

def write_header():
    '''
    Writes header info into output file
    '''
    lines = []
    with open(config_filename,mode='r') as config_file:
        lines = config_file.readlines()
    with open(output_filename,mode='w') as output_file:
        for line in lines:

```

```

        output_file.write(line)
    if not lines[-1][-1]=='\n':
        output_file.write('\n')
    columnnames =
["timestamp", "T_set", "Src_SP", "Filter_OD", "V_src", "I_src", "R",
"Theta", "R_dev", "Theta_dev", "LIA_laser_light", "LIA_LED_light",
"DMM_laser_light", "DMM_LED_light", "T", "V_LED"]
    sp_unit = "-"
    if src_control_mode=="voltage":
        sp_unit = "V"
    elif src_control_mode=="current":
        sp_unit = "A"
    units = {"timestamp": "UTC
timestamp", "T_set": "C", "Src_SP": sp_unit, "Filter_OD": "OD", "V_sr
c": "V", "I_src": "A", "R": "V", "Theta": "deg", "R_dev": "V", "Theta_de
v": "deg", "LIA_laser_light": "V", "LIA_LED_light": "V", "DMM_laser_
light": "V", "DMM_LED_light": "V", "T": "C", "V_LED": "V"}
    writer =
csv.DictWriter(output_file, fieldnames=columnnames, delimiter=',
', lineterminator='\n')
    writer.writeheader()
    writer.writerow(units)

```

```

def temperature(R):
    """
    Converts thermistor resistance (output of TEC stage) to
    temperature in Kelvin
    """
    params = parser['Temperature Stage']
    C1, C2, C3 =
float(params['C1']), float(params['C2']), float(params['C3'])
    R *= 1e4
    return 1. / (C1 + C2 * np.log(R) + C3 * (np.log(R) ** 3))

```

```

def write_data(SRC_data, LIA_data, DMM_data, T, F, sp):
    """
    Appends data to output file
    """
    print("Writing data to file")
    timestamp = dt.datetime.now().timestamp()
    with open(output_filename, mode='a') as output_file:
        columnnames =
["timestamp", "T_set", "Src_SP", "Filter_OD", "V_src", "I_src", "R",
"Theta", "R_dev", "Theta_dev", "LIA_laser_light", "LIA_LED_light",
"DMM_laser_light", "DMM_LED_light", "T", "V_LED"]

```

```

        writer
csv.DictWriter(output_file, fieldnames=columnnames, delimiter=',',
',lineterminator='\n')

```

```

row = {}
row["timestamp"] = str(timestamp)
row["T_set"] = str(T)
row["Src_SP"] = str(sp)
row["Filter_OD"] = str(F)
row["V_src"] = str(SRC_data[0])
row["I_src"] = str(SRC_data[1])
row["R"] = str(LIA_data[0])
row["Theta"] = str(LIA_data[1])
row["R_dev"] = str(LIA_data[2])
row["Theta_dev"] = str(LIA_data[3])
row["LIA_laser_light"] = str(LIA_data[4])
row["LIA_LED_light"] = str(LIA_data[5])
row["DMM_laser_light"] = str(DMM_data[0])
row["DMM_LED_light"] = str(DMM_data[1])
row["T"] = str(temperature(LIA_data[6]))
row["V_LED"] = str(LIA_data[7])
writer.writerow(row)

```

```

def wait_temperature():
    """
    Waits for temperature to stabilize
    Stores and collects temperature data from lock-in buffer
    and calculates standard deviation to see if it is stabilized
    yet
    Returns when temperature is stabilized
    """
    LIA.write("DDEF 2,3,0") #set CH2 to display Aux 3 value
    LIA.write("SRAT 13") #set sample rate to 512 Hz
    LIA.write("SEND 1") #set buffer mode to Loop

    stable = False
    while not stable:
        LIA.write("STRT") #starts data storage
        print("Collecting temperature stability data")
        time.sleep(512/512 * 1.1) #wait for buffer to collect
some data
        LIA.write("PAUS") #pauses data storage
        pts = int(LIA.query("SPTS?")[:-1])
        while pts<513:
            LIA.write("STRT")
            time.sleep(1)

```

```

        LIA.write("PAUS")
        pts = int(LIA.query("SPTS?")[:-1])
    print("# of stored points: ",pts)
    print("Reading temperature stability data")
    data = LIA.query("TRCA? 2,0,512").split(',')[:-1]
    print("Temperature data read")
    LIA.write("REST") #resets data buffer
    R = np.array([float(d) for d in data]) #analog output
of TEC controller
    R_mean,R_std = np.mean(R),np.std(R)
    R_spread = R_std/R_mean*100
    ##T_data = temperature(R) #temperature of stage in
Kelvin
    ##T_mean,T_std = np.mean(T_data),np.std(T_data)
    ##T_spread = T_std/T_mean*100 #in %
    #check that the standard deviation of the temperature
is < threshold percentage of the mean value (i.e. - stabilized
to within threshold percentage)
    ##threshold_percentage = float(parser['Lock-
in']['std_dev_threshold']) #in %
    if R_spread < 2.0:
        stable = True
        print("Temperature stable")
    else:
        continue

def wait_laser():
    '''
    Waits for laser power to stabilize
    Stores and collects laser power data from lock-in buffer
and calculates standard deviation to see if it is stabilized
yet
    Returns when laser power is stabilized
    '''
    LIA.write("DDEF 1,3,0") #set CH1 to display Aux 1 value
    LIA.write("SRAT 13") #set sample rate to 512 Hz
    LIA.write("SEND 1") #set buffer mode to Loop

    stable = False
    while not stable:
        LIA.write("STRT") #starts data storage
        print("Collecting pump light source stability data")
        time.sleep(128/512 * 1.1) #wait for buffer to overflow
a little
        LIA.write("PAUS") #pauses data storage

```

```

pts = int(LIA.query("SPTS?")[:-1])
while pts<129:
    LIA.write("STRT")
    time.sleep(1)
    LIA.write("PAUS")
    pts = int(LIA.query("SPTS?")[:-1])
print("# of stored points: ",pts)
data = LIA.query("TRCA? 1,0,128").split(',')[:-1]
LIA.write("REST") #resets data buffer
data = np.array([float(d) for d in data])
mean,std = np.mean(data),np.std(data)
spread = std/mean*100 #in %
#check that the standard deviation of the temperature
is < threshold percentage of the mean value (i.e. - stabilized
to within threshold percentage)
    threshold_percentage = float(parser['Lock-
in']['std_dev_threshold']) #in %
    if spread < threshold_percentage:
        stable = True
        print("Laser power stable")
    else:
        continue

def auto_gain():
    '''
    Automatically sets the gain and time-constant on the lock-
in amplifier
    '''
    T = min_t_constant
    S = autogain_sens_start #sensitivity_dict['1 V'] #use the
commented out code to override the config file value (might slow
down measurement significantly!)

    def wait_10T():
        '''
        Waits for 10 times the time constant, T, where T is the
0-19 integer the lock-in uses (which can be looked up in
t_constant_dict)
        '''
        arr = [1,3]
        t = arr[T%2] * 10**((T-T%2)/2-5) #time constant in
seconds
        time.sleep(10*t)

    def check_FS():
        '''

```

```

> 37% Checks the ratio of R to the full scale sensitivity is
'''
LIA.write("DDEF 1,1,0") #set CH1 to display R value
LIA.write("SRAT 13") #set sample rate to 512 Hz
LIA.write("SEND 1") #set buffer mode to Loop

arr = [2,5,10]
FS = arr[S%3] * 10**((S-S%3)/3-9) #FS sensitivity in V
LIA.write("STRT") #starts data storage
print("Collecting R stability data for checking %%FS
and setting sensitivity")
N = 128
if T>9:
    if T==10:
        N = 1024
    else:
        N = 1536
time.sleep(N/512 * 1.1) #wait for buffer to overfill a
little
LIA.write("PAUS") #pauses data storage
pts = int(LIA.query("SPTS?")[:-1])
while pts<N+1:
    LIA.write("STRT")
    time.sleep(1)
    LIA.write("PAUS")
    pts = int(LIA.query("SPTS?")[:-1])
print("# of stored points: ",pts)
data = LIA.query("TRCA? 1,0,%d" % (N)).split(',')[:-1]
LIA.write("REST") #resets data buffer
data = np.array([float(d) for d in data])
max_value = max(data)
#returns the number of sensitivity settings that the
lock-in should decrement by
if max_value/FS > 0.37:
    return 0
elif max_value/FS < 0.20:
    return 2
else:
    return 1

def check_T():
'''
Checks that the std dev of R is below threshold, i.e.,
that the time constant is long enough to stabilize R
'''
LIA.write("DDEF 1,1,0") #set CH1 to display R value

```

```

LIA.write("SRAT 13") #set sample rate to 512 Hz
LIA.write("SEND 1") #set buffer mode to Loop

LIA.write("STRT") #starts data storage
print("Collecting R stability data for setting time-
constant")
N = 128
if T>9:
    if T==10:
        N = 1024
    else:
        N = 1536
time.sleep(N/512 * 1.1) #wait for buffer to overflow a
little
LIA.write("PAUS") #pauses data storage
pts = int(LIA.query("SPTS?")[:-1])
while pts<N+1:
    LIA.write("STRT")
    time.sleep(1)
    LIA.write("PAUS")
    pts = int(LIA.query("SPTS?")[:-1])
print("# of stored points: ",pts)
data = LIA.query("TRCA? 1,0,%d" % (N)).split(',')[:-1]
LIA.write("REST") #resets data buffer
data = np.array([float(d) for d in data])
mean,std = np.mean(data),np.std(data)
spread = std/mean*100 #in %
threshold_percentage = float(parser['Lock-
in']['std_dev_threshold']) #in %
if spread < threshold_percentage:
    return True
else:
    return False

LIA.write("OFLT %d" % (T))
LIA.write("SENS %d" % (S))
wait_10T()
FS_ret_val = check_FS()
while FS_ret_val:
    S -= FS_ret_val
    arr = [2,5,10]
    print("Decreasing sensisitivity to %0.0e V" % (arr[S%3]
* 10**((S-S%3)/3-9)))
    LIA.write("SENS %d" % (S))
    wait_10T()
    FS_ret_val = check_FS()
while T<max_t_constant and not check_T():

```

```

        T += 1
        arr = [1,3]
        print("Increasing time constant to %0.0e s" % (arr[T%2]
* 10**((T-T%2)/2-5)))
        LIA.write("OFLT %d" % (T))
        wait_10T()
        S += 1
        LIA.write("SENS %d" % (S))
        wait_10T()
        FS_ret_val = check_FS()
        while FS_ret_val:
            S -= FS_ret_val
            arr = [2,5,10]
            print("Decreasing sensisitivity to %0.0e V" %
(arr[S%3] * 10**((S-S%3)/3-9)))
            LIA.write("SENS %d" % (S))
            wait_10T()
            FS_ret_val = check_FS()

        if T==max_t_constant-1:
            wait_10T()

def average_LIA_SNAP(n):
    '''
    Averages n (n>0) SNAP measurements of the lock-in data
    '''
    aux_data = np.zeros(4)
    for i in range(n):
        print("querying ascii values")
        data = LIA.query_ascii_values("SNAP?
5,6,7,8",container=np.array,converter='f')
        for j in range(len(data)):
            aux_data[j] += data[j]/float(n)
    return aux_data

def get_LIA_data(num_snaps,dark=False):
    '''
    Function to get LIA_data
    R,theta by averaging over 3 seconds of data sampled at
    512 Hz
    Aux inputs via SNAP?
    '''
    if not dark:
        auto_gain() #auto-gain the lock-in!!! This is very
important!!!

```



```

LIA.write("DDEF 1,1,0") #set CH1 to display R value
LIA.write("DDEF 2,1,0") #set CH2 to display theta value
LIA.write("SRAT 13") #set sample rate to 512 Hz
LIA.write("SEND 1") #set buffer mode to Loop

LIA.write("STRT")
print("Collecting Lock-in measurements")
time.sleep(1536/512 * 1.1) #wait for buffer to overflow
a little
LIA.write("PAUS") #pauses data storage
pts = int(LIA.query("SPTS?")[:-1])
while pts<1537:
    LIA.write("STRT")
    time.sleep(1)
    LIA.write("PAUS")
    pts = int(LIA.query("SPTS?")[:-1])
print("# of stored points: ",pts)
CH1 = LIA.query("TRCA? 1,0,1536").split(',')[:-1]
CH2 = LIA.query("TRCA? 2,0,1536").split(',')[:-1]
LIA.write("REST")
R_data = np.array([float(d) for d in CH1])
theta_data = np.array([float(d) for d in CH2])
R = np.mean(R_data)
theta = np.mean(theta_data)
R_dev = np.std(R_data)
theta_dev = np.std(theta_data)
else:
    R,theta = '-','- '
    R_dev,theta_dev = '-','- '

aux1,aux2,aux3,aux4 = average_LIA_SNAP(num_snaps)

return (R,theta,R_dev,theta_dev,aux1,aux2,aux3,aux4)

def measure_LIV(T,F,dark=False):
    '''
    Collects the LIV measurement (default is with pump on)
    '''
    if dark:
        #Ask user to ensure LED is in the dark (room lights off,
        etc...)
        input("Turn off the room lights and seal the enclosure
        around the LED for the dark LIV measurment\n\tPress \"ENTER\"
        to continue")

    SRC.write("output on")

```

```

#loop over setpoints and write data to file
sp_counter = 0
for sp in src_setpoints:
    sp_counter += 1
    #Set K2400 output
    if src_control_mode == "current":
        print("SP %d of %d:\n\tSetting current to %0.2e mA"
% (sp_counter,num_setpoints,sp*1000))
        SRC.write("source:current:level %0.2e" % (sp)) #set
current to setpoint
    elif src_control_mode == "voltage":
        print("SP %d of %d:\n\tSetting voltage to %0.2e V"
% (sp_counter,num_setpoints,sp))
        SRC.write("source:voltage:level %0.2e" % (sp)) #set
bias to setpoint
    else:
        sys.exit("Check src_control_mode in config file --
must be 'voltage' or 'current'")

    #Trigger K2400 measurement of I and V and K2000 DMM
measurement of laser_light and LED_light
    DMM.write("initiate")
    SRC.write("initiate")
    DMM.write("*wai")
    SRC_data =
SRC.query_ascii_values("trace:data?",container=np.array,conver
ter='f')
    DMM_data =
DMM.query_ascii_values("trace:data?",container=np.array,conver
ter='f')

    #Trigger Lock-in measurement (SNAP? 3,4,5,6,7,8)
    LIA_data = get_LIA_data(num_snaps,dark=dark) #will
return '-' for R,theta,R_dev,theta_dev if dark=True
    #Write data to output file
    write_data(SRC_data,LIA_data,DMM_data,T,F,sp)

    #Clear the traces of the SourceMeter and DMM, and reset
the trace settings (may not be necessary, but just in case of
any funny business...)
    SRC.write("trace:clear")
    SRC.write("trace:points 1")
    SRC.write("trace:feed sense")
    SRC.write("trace:feed:control next")
    DMM.write("trace:clear")

```

```

        DMM.write("trace:points                %d"                %)
(dmm_num_channels*num_readings)) #MUST COME BEFORE FEED CONTROL
AND AFTER TRIG AND SMPL COUNT
        DMM.write("trace:feed sense")
        DMM.write("trace:feed:control next")

#turn off Keithley output after measurement of all setpoints
SRC.write("output off")

#####
#####
#####                               Entry point and main function call
#####
#####
#####
#####
if __name__=='__main__':
    main()

```

C. Auger-Generated Hot Carrier Currents

This appendix describes some of the different types of Auger recombination events, both conventional and defect-assisted, which can generate hot carrier currents.

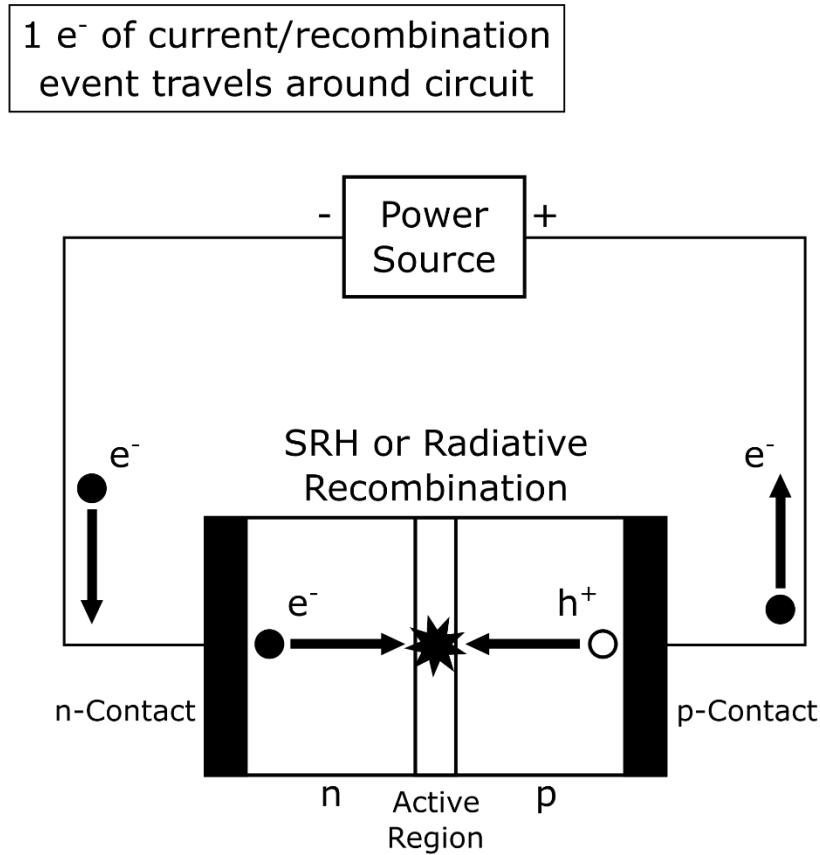


Figure C.0.1: Schematic of an LED under forward bias, including the external circuit, showing the current per SRH or radiative recombination event. Note that holes have the opposite charge from electrons so that when they are injected from the p-contact, it corresponds to electrons being extracted from the p-contact into the external circuit.

Figure C.0.1 depicts the current flow through an LED – and the external circuit, which supplies power to the LED – for either SRH or radiative recombination. There is only one electron of current per recombination event.

1.5 e^- of current/recombination event travels around circuit, on average

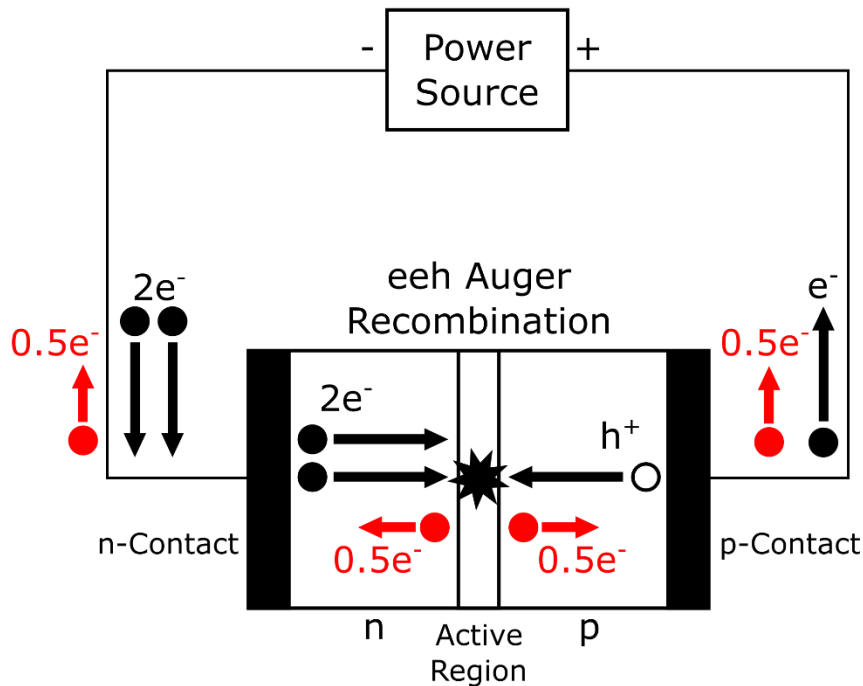


Figure C.0.2: Schematic of an LED under forward bias, including the external circuit, showing the average current per *eeh* Auger recombination event. The hot electrons (and the additional current they induce in the external circuit) are shown in red. Note that holes have the opposite charge from electrons so that when they are injected from the p-contact, it corresponds to electrons being extracted from the p-contact into the external circuit.

The situation is different for Auger recombination, where there is a third carrier (the eventual hot carrier) which must be taken into account. This is depicted below in Figure C.0.2 for *eeh* Auger, and in Figure C.0.3 for *ehh* Auger. The additional current is the same in either case – 0.5 additional electrons, on average, when compared to SRH or radiative recombination.

1.5 e^- of current/recombination event travels around circuit, on average

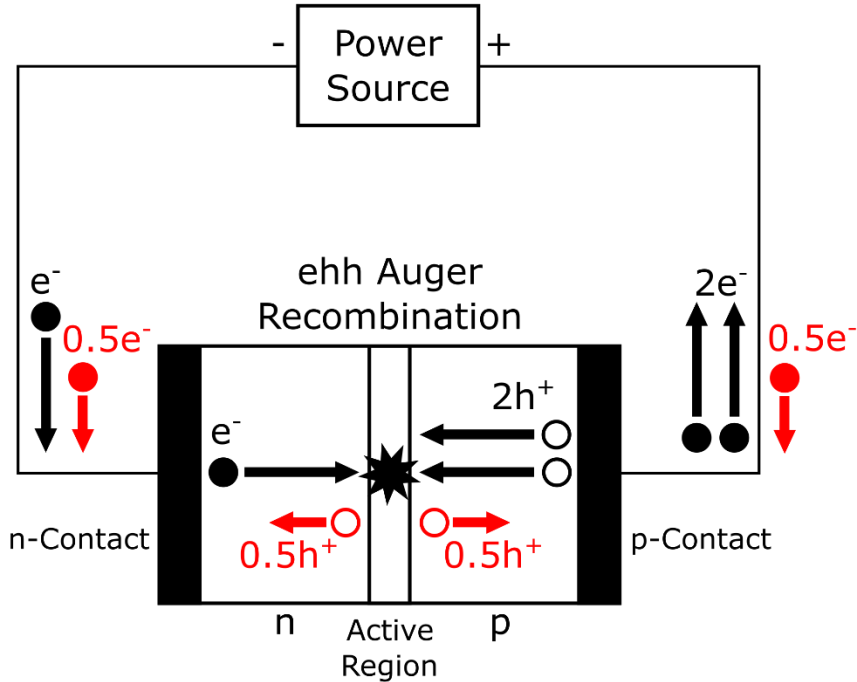


Figure C.0.3: Schematic of an LED under forward bias, including the external circuit, showing the average current per *ehh* Auger recombination event. The hot holes (and the additional current they induce in the external circuit) are shown in red. Note that holes have the opposite charge from electrons so that when they are injected from the p-contact, it corresponds to electrons being extracted from the p-contact into the external circuit.

The situation depicted in Figure C.0.2 and Figure C.0.3 apply to any kind of Auger recombination, including trap-assisted Auger recombination (discussed at the end of this appendix).

Section C.1 details the different conventional Auger recombination events which may occur in the active region of a QW LED, specifically addressing the different directions the hot carriers may escape in, as well as the electrically- and optically-injected cases separately. Section C.2 details the many cases which may occur for trap-assisted Auger recombination in the active region.

As discussed elsewhere in this dissertation, the net current due to Auger-generated hot carriers is always the average of the current due to the hot carriers travelling forward and those travelling in reverse – approximately one half carrier of current per recombination event extra, regardless of the kind of Auger process involved.

C.1 Conventional Auger Recombination

Conventional Auger recombination in the active region of an LED, either band-to-band or phonon-assisted, can generate either hot electrons (*eeh*) or hot holes (*ehh*). Those hot carriers may travel either in the forward direction upon leaving the active region, or in the reverse direction. Depicted in Figure C.1.1 are these four cases – *eeh* or *ehh* and escape in the forward or reverse direction – for the situation when all the carriers involved in the Auger recombination are electrically injected from the contacts.

Figure C.1.1(a) and Figure C.1.1(c) show the hot carriers travelling in the forward direction, adding an extra carrier worth of current per recombination event compared to when they travel in the reverse direction (Figure C.1.1(b) and Figure C.1.1(d)).

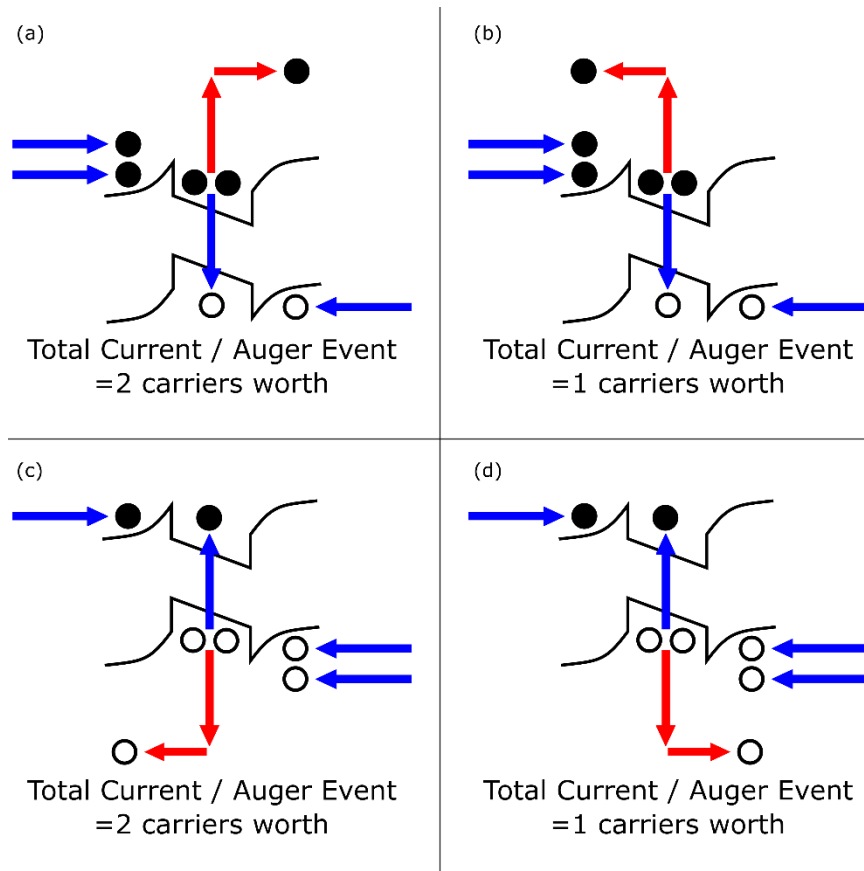


Figure C.1.1: Schematics showing conventional Auger recombination processes in a SQW LED, in the dark where the recombining electron-hole pair is electrically injected. In cases (a) and (b), the hot carrier is an electrically injected electron, and in (c) and (d) the hot carrier is an electrically injected hole. The hot carrier travels in the forward direction in (a) and (c), and in reverse in (b) and (d).

Depicted in Figure C.1.2 is the situation when the eventual hot carrier is electrically injected, but the recombining electron-hole pair is optically excited by resonant photo-excitation of the QW layer. The hot carrier still carries additional current only when it escapes in the forward direction but now there is no current due to the injection of the recombining electron hole pair.

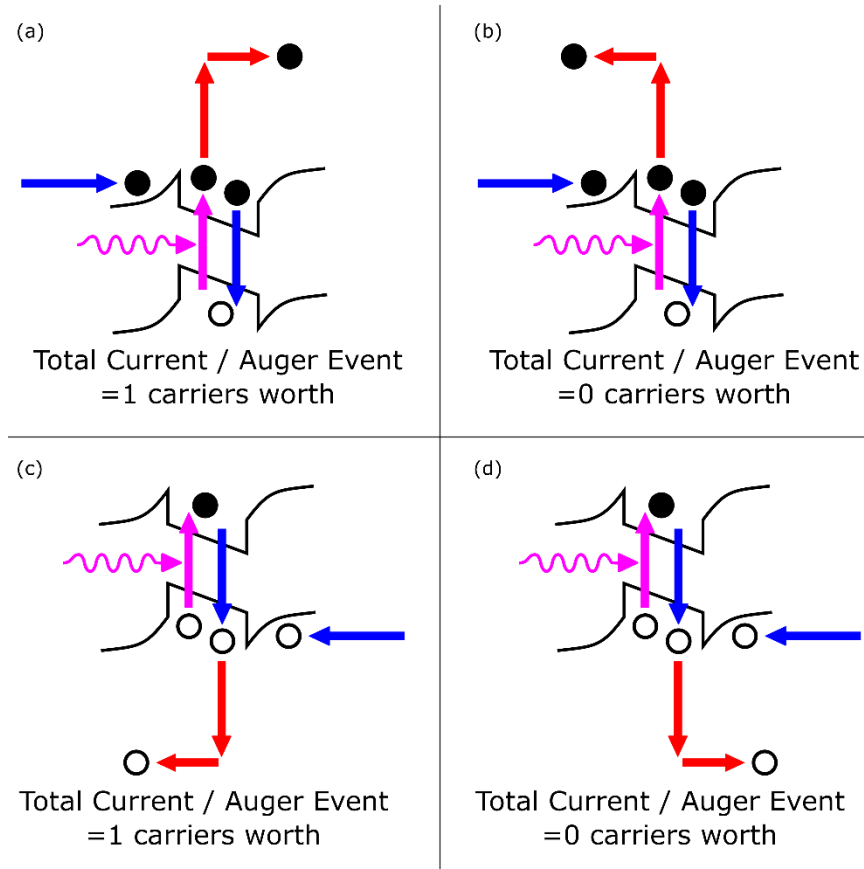


Figure C.1.2: Schematics showing conventional Auger recombination processes in a SQW LED, under resonant optical excitation of the QW layer. Only the eventual hot carrier is electrically injected. In cases (a) and (b), the hot carrier is an electrically injected electron, and in (c) and (d) the hot carrier is an electrically injected hole. The hot carrier travels in the forward direction in (a) and (c), and in reverse in (b) and (d).

C.2 Defect-Assisted Auger Recombination

There are several different flavors of defect-assisted Auger recombination, which are well described in Ref. [31]. Again, the hot carrier may be either an electron or a hole, but there is an additional variable – namely which of the two steps in the defect-assisted recombination produces the hot carrier. The hot carrier may result either from the electron capture step or from the hole capture step. This results in four varieties of defect-assisted Auger recombination, as opposed to two for the conventional Auger processes.

Additionally, either the electron capture or the hole capture will be the rate-limiting step (both occur in series). It is not necessary that the slow step will also be the Auger step, but since the Auger process will involve a second carrier (the hot carrier) it is perhaps reasonable to assume that they will be the same. Only these cases are depicted in the figures below, as the number of processes that would need to be depicted would double otherwise.

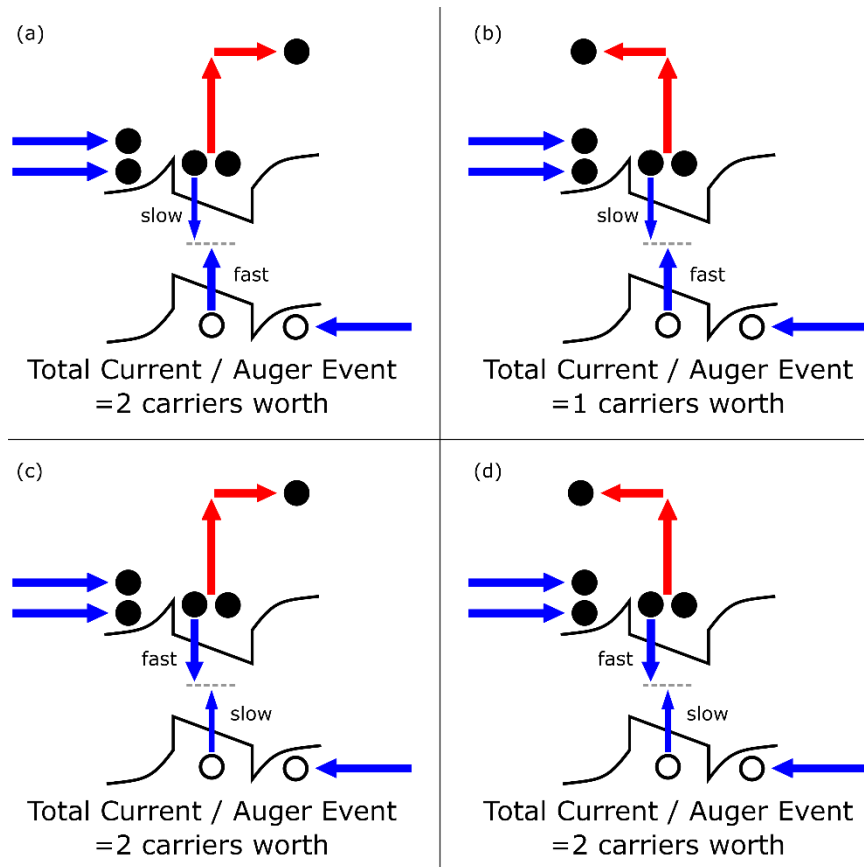


Figure C.2.1: Schematics showing trap-assisted Auger recombination processes in a SQW LED, in the dark, when all of the carriers are electrically injected. Only processes generating hot electrons are shown in this figure. In cases (a) and (b), the slow and hot carrier-generating Auger process is the electron capture process, and in (c) and (d) it is the hole capture process. The hot carrier travels in the forward direction in (a) and (c), and in reverse in (b) and (d).

Figure C.2.1 shows hot electron-generating trap-assisted Auger recombination processes in a SQW LED, in the dark. As with conventional Auger processes, there is additional forward

current due to the hot carriers which escape in the forward direction, but not to those escaping in the reverse direction.

Figure C.2.2 shows hot hole-generating trap-assisted Auger recombination processes in a SQW LED, in the dark. These processes are exactly analogous to the hot electron-generating processes shown in Figure C.2.1, except in the type of hot carrier produced.

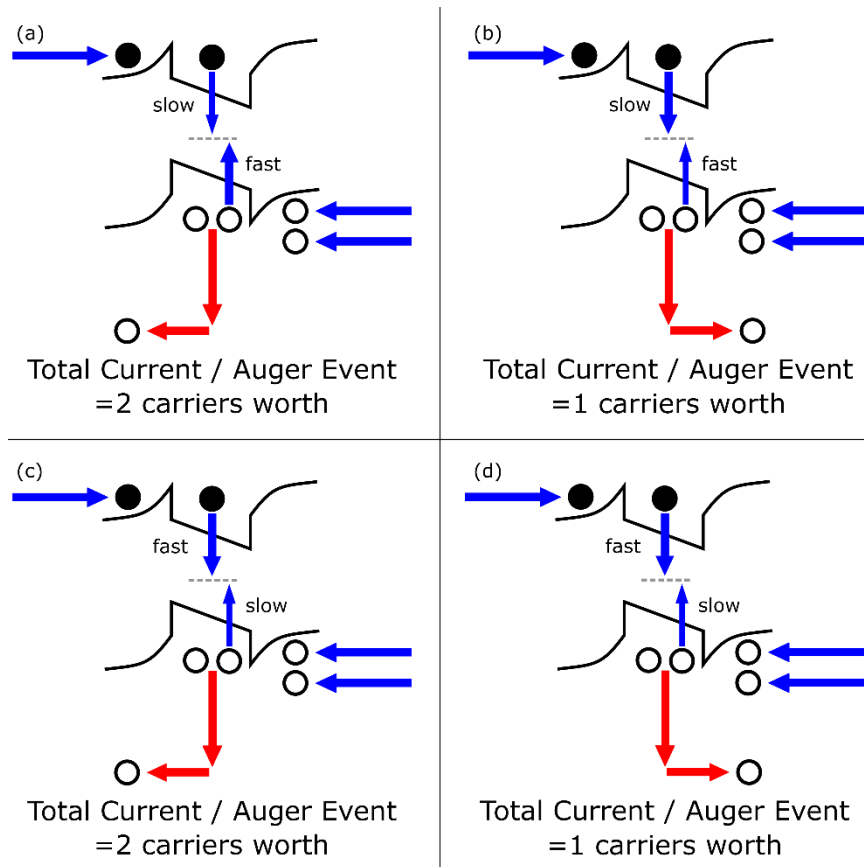


Figure C.2.2: Schematics showing trap-assisted Auger recombination processes in a SQW LED, in the dark, when all of the carriers are electrically injected. Only processes generating hot holes are shown in this figure. In cases (a) and (b), the slow and hot carrier-generating Auger process is the electron capture process, and in (c) and (d) it is the hole capture process. The hot carrier travels in the forward direction in (a) and (c), and in reverse in (b) and (d).

When the recombining electron-hole pair are optically excited by resonant photo-excitation of the QW layer, the cases depicted in Figure C.2.3 (hot electrons) and Figure C.2.4 (hot holes)

result. As with conventional Auger recombination, there is no current from the recombining electron-hole pair, but there is current due to the hot carriers which escape in the forward direction.

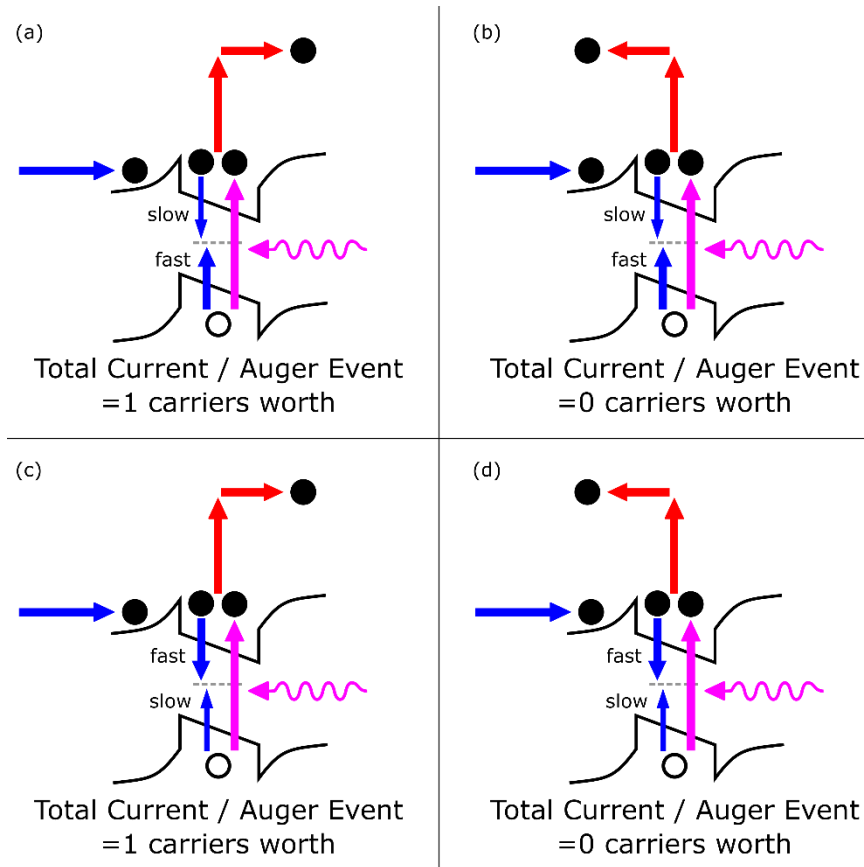


Figure C.2.3: Schematics showing trap-assisted Auger recombination processes in a SQW LED, under resonant optical excitation of the QW layer. Only the eventual hot carrier is electrically injected. Only processes generating hot electrons are shown in this figure. In cases (a) and (b), the slow and hot carrier-generating Auger process is the electron capture process, and in (c) and (d) it is the hole capture process. The hot carrier travels in the forward direction in (a) and (c), and in reverse in (b) and (d).

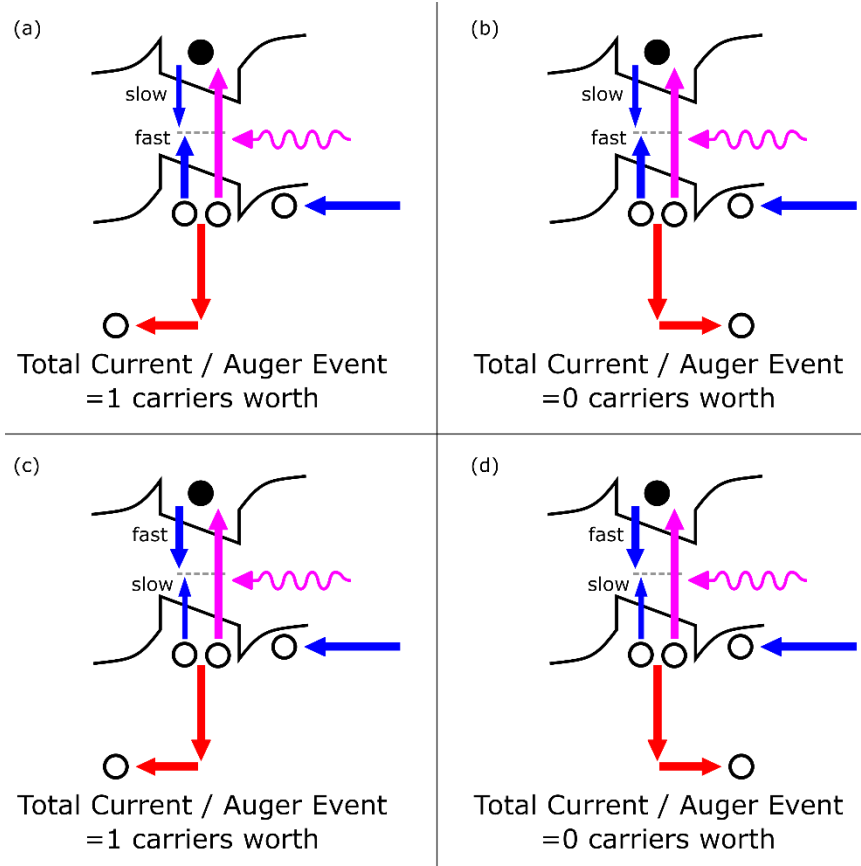


Figure C.2.4: Schematics showing trap-assisted Auger recombination processes in a SQW LED, under resonant optical excitation of the QW layer. Only the eventual hot carrier is electrically injected. Only processes generating hot hole are shown in this figure. In cases (a) and (b), the slow and hot carrier-generating Auger process is the electron capture process, and in (c) and (d) it is the hole capture process. The hot carrier travels in the forward direction in (a) and (c), and in reverse in (b) and (d).